Electrical Characterization of Colloidal Lead Sulphide Nanocrystals

A dissertation

Submitted to the University of Hamburg - Department of Chemistry

In partial fulfillment of the requirements for the degree of

Doctor of Natural Sciences (*Dr. rer. Nat.*)

Mohammad Mehdi Ramin Moayed

Hamburg 2018

1. Reviewer: Prof. Dr. Christian Klinke

2. Reviewer: Prof. Dr. Gabriel Bester

Date of the thesis defense: 17.08.2018

Date of the thesis approval: 20.08.2018

Publications

The work described in this thesis was carried out between August 2014 and July 2018 at the Institute of Physical Chemistry, University of Hamburg in the group of Prof. Dr. Christian Klinke. During this period, I worked on five manuscripts which were published in scientific journals or as conference proceedings, and two manuscripts which were still under the revision process when this thesis was written. These publications are mentioned subsequently.

Main Papers:

Thomas Bielewicz, **Mohammad Mehdi Ramin Moayed**, Vera Lebedeva, Christian Strelow, Angelique Rieckmann, Christian Klinke, From dots to stripes to sheets: Shape control of lead sulfide nanostructures, Chemistry of Materials 27 (2015) 8248.

Mohammad Mehdi Ramin Moayed, Thomas Bielewicz, Martin Sebastian Zöllner, Carmen Herrmann, Christian Klinke, Towards colloidal spintronics through Rashba spin-orbit interaction in lead sulphide nanosheets, Nature Communications 8 (2017) 15721.

Mohammad Mehdi Ramin Moayed, Thomas Bielewicz, Heshmat Noei, Andreas Stierle, Christian Klinke, High Performance n- and p-Type Field-Effect Transistors Based on Hybridly Surface Passivated Colloidal PbS Nanosheets, Advanced Functional Materials (2018) 1706815.

Other Papers:

Mohammad Mehdi Ramin Moayed, Thomas Bielewicz, Martin Sebastian Zöllner, Carmen Herrmann, Christian Klinke, Rashba Spin-Orbit Coupling in Colloidal Lead Sulfide Nanosheets, Proceedings of Advanced Photonics 2017, OSA Technical Digest NoTu1C.3.

Frauke Gerdes, Eugen Klein, Sascha Kull, **Mohammad Mehdi Ramin Moayed**, Rostyslav Lesyuk, Christian Klinke, Review: Halogens in the synthesis of colloidal semiconductor nanocrystals, Zeitschrift für Physikalische Chemie (2018) 1164.

Under revision:

Mohammad Mehdi Ramin Moayed, Sascha Kull, Angelique Rieckmann, Philip Beck, Michael Wagstaffe, Heshmat Noei, Andreas Kornowski, Rostyslav Lesyuk, Andreas Stierle, Christian Klinke, From a semiconductor to a metal: tuning electrical properties of lead sulphide by sculpting the crystal

Fu Li, **Mohammad Mehdi Ramin Moayed**, Frauke Gerdes, Sascha Kull, Eugen Klein, Rostyslav Lesyuk, Christian Klinke, Formation Mechanism, Ligand-mediated Shape Tuning and Photo-detection of Single-Crystalline Laterally Large SnS Nanosheets

Content

Notations

Bulk-inversion asymmetry	BIA
Chemical-vapor deposition	CVD
Circular photogalvanic effect	CPGE
Density-functional theory	DFT
Density of states	DOS
Electron-beam lithography	EBL
Field-effect transistors	FETs
Giant magnetoresistance	GMR
High resolution transmission-electron microscope	HRTEM
Integrated circuits	ICs
Linear photogalvanic effect	LPGE
Molecular-beam epitaxy	MBE
Nanocrystal	NC
Spin degree of freedom	SDoF
Spin field-effect transistor	SFET
Spin-orbit coupling	SOC
Structural-inversion asymmetry	SIA
Transition metal dichalcogenides	TMDs
Transmission-electron microscope	TEM
Tunnel magnetoresistance	TMR
X-ray photoelectron spectroscopy	XPS
X-ray powder diffraction	XRD

Abstract

By approaching the end of Moore's law, many efforts have been undertaken for semiconductor technology to keep its progress pace. Finding new materials to be employed instead of the conventional materials or finding new paradigms for data processing are among them. In order to contribute to these efforts, I investigated the electrical properties of lead sulphide nanocrystals.

Lead sulphide is a small bandgap material with many promising properties and applications. This material could be synthesized recently in the form of 2D nanosheets which are laterally large enough to be individually contacted. These nanosheets have been already used as field-effect transistors (FETs) and solar cells.

In order to employ this material for future electronics, its transistor behavior had to be improved. As the first step, the lateral size of the nanosheets has been optimized. By reducing the width of the crystal, which is equivalent to the reduction of the transistors' active channel, the functionality of the devices has been boosted. This became possible by employing quasi-1D stripes instead of the normal squared nanosheets. This modification has improved the on/off ratio by a few orders of magnitude.

The other important aspect is the possible imperfections of the crystal, which could hinder its high performance when it is used as a functional device. One of the critical imperfections in colloidal crystals could be their surface which normally contains trap states, originating from dangling bonds. To address this problem, the capability of different halogenoalkanes has been investigated to passivate the surface of the PbS nanosheets. Electrical measurements have shown that Cl^- ions, which are provided by the decomposition of chloroalkanes, are able to effectively passivate these traps. The conductivity, field-effect mobility and on/off ratio of the sheets were significantly higher, when a Cl-containing coligand had been used to synthesize them, in addition to oleic acid as the main ligand (hybrid surface passivation). The passivation effect has been further signified by increasing the amount of the used coligand. The existence of Cl^- ions on the surface of the high performance nanosheets has been confirmed with X-ray photoelectron spectroscopy.

Further, the contact metal and the working environment have remarkable effects on the FET behavior of the sheets. Carefully adjusting the aforementioned parameters made it possible to realize high performance n-type FETs based on PbS. For this purpose, narrow stripes with a fully Cl-passivated surface have been contacted with Ti, as a proper contact metal for n-type materials, and the obtained devices have been characterized in vacuum. The outcome of this

experiment was a FET with record on/off ratio and field-effect mobility among other colloidal materials. To convert the devices to p-type, Au contacts have been employed and air has been introduced to the crystal.

The applications of the PbS nanosheets can be also expanded beyond conventional electronics. For this purpose, the spin-orbit coupling of the nanosheets has been investigated by performing circular photogalvanic measurements in order to probe their potential application in spintronics. When a material has a strong spin-orbit coupling, its band structure splits based on the spin orientation of the charge carriers. By illuminating this material with circularly polarized light, the spin equilibrium of the split bands is broken, resulting in an asymmetric distribution of the carriers in momentum space. This can be detected as a helicity-dependent net current while no bias voltage is applied to the material. The amplitude of this current could be considered as a measure for the strength of the spin-orbit coupling.

In order to see this effect with the PbS nanosheets, their crystalline symmetry has been broken by applying asymmetric interfaces on top and underneath (SiO_2 and vacuum) or by applying a gate electric field. The observed effect, which could be tuned by altering the gate voltage or by changing the thickness of the crystal, has been also investigated theoretically by density-functional theory calculations. The obtained insight, which is the first observation of the spin transport through colloidal materials, has opened new pathways for colloidal spintronics.

Eventually, to further expand the potential applications of PbS, its properties have been altered by manipulating the crystal. A certain form of PbS nanowires has been found that shows metallic behavior, in contrast to the other forms which are all semiconducting. The reason for that is the presence of the single element Pb rich {111} facets on the surface of these wires, which makes the crystal metallic. This has been done by synthesizing small octahedra during the early stages of the synthesis. By the attachment of these octahedra, zigzag shaped metallic nanowires are produced which have the Pb rich {111} surface facets.

Transport measurements have been employed to prove the metallic character of the wires in addition to density-functional theory calculations. The ability to tune the electrical properties of a material only by sculpting its crystal is important since it helps to better optimize many types of crystalline systems. The results introduce new applications for PbS nanowires such as flexible interconnects.

Zusammenfassung

In dieser Arbeit wurden die elektrischen Eigenschaften verschiedener PbS Nanostrukturen untersucht. Solche Nanostrukturen könnten als aktives Material für zukünftige elektronische Bauteile oder für neue Methoden der Datenverarbeitung (z. B. für Spintronik) verwendet werden.

Im ersten Teil der Arbeit wurden die Nanostrukturen zur Herstellung von Feldeffekttransistoren (FETs) verwendet. Die laterale Breite des Kristalls wurde verringert, um die Leistung dieser FETs zu verbessern. Schmale PbS Nanostreifen zeigten dabei ein besseres Transistorverhalten (On/Off-Verhältnis und Feldeffektmobilität) als breite Nanoblätter.

Zusätzlich wurden verschiedene Halogenalkane verwendet, um die Oberfläche der Nanoblätter zu passivieren. Wenn Chlorid-Ionen zu der Synthese hinzugefügt wurden, waren die Oberflächendefekte des Kristalls passiviert und die Nanoblätter wiesen ein höheres On/Off-Verhältnis und eine höhere Feldeffektmobilität auf. Die Existenz von Chlorid-Ionen wurde auch mit der Röntgenphotoelektronenspektroskopie (XPS) bestätigt. Hochleistungs-n-Typ-FETs wurden unter Verwendung Chlorid-passivierter schmaler Streifen, die mit Ti kontaktiert und im Vakuum vermessen wurden, erreicht. Die Leistung dieser Transistoren entspricht der höchsten, die für kolloidale Nanostrukturen beobachtet wurde. Durch Änderung des Kontaktmetalls zu Au zeigten die Nanoblätter unter Luftatmosphäre ein p-Typ-Verhalten.

Im zweiten Teil der Arbeit wurden die Nanoblätter für Anwendungen jenseits herkömmlicher Elektronik untersucht. Zu diesem Zweck wurde die Rashba Spin-Bahn-Kopplung der Nanoblätter durch die zirkular photogalvanische Messungen untersucht, um ihre mögliche Anwendung in der Spintronik zu erforschen. Die Symmetrie des Kristalls wurde durch die asymmetrischen Grenzflächen oben und unten (SiO_2 und Vakuum) oder durch den Einfluss eines äußeren elektrischen Feldes aufgebrochen. Durch die Beleuchtung mit zirkular-polarisiertem Licht war es möglich, elektrische Ladungen in Nanoblättern auszurichten und in elektrischen Strom umzuwandeln ohne, dass eine Spannung angelegt werden musste. Durch die Variation der Schichtdicke der Nanoblätter, der Polarisation des verwendeten Lichtes und der Intensität der elektrischen Felder ließ sich der Effekt kontrollieren. Die experimentellen Beobachtungen wurden mit Simulationen der elektronischen Struktur der Materialien unterstützt. Dies ist die erste Beobachtung des Spintransports in kolloidalen Materialien.

Im letzten Teil wurde eine bestimmte Form von PbS-Nanodrähten untersucht, die metallisch ist. Diese Drähte bestanden aus Oktaedern, dessen Oberfläche durch {111} –Facetten gebildet wurde und aus Pb-Atomen bestand. Wegen dieser Pb-reichen Oberfläche waren diese Drähte metallisch. Transportmessungen und DFT-Berechnungen wurden verwendet, um den metallischen Charakter der Drähte zu erklären. Diese Ergebnisse führen zu neuen Anwendungen für PbS, z. B. zu flexiblen Verbindungen.

Chapter 1:

Introduction

1-1 Electronics: From Past to Future

Since 1970, improvements of the electronics industry have been mainly based on the miniaturization of electronic components in integrated circuits (ICs). According to Moore's law, the 1965 prediction of the Intel co-founder Gordon Moore, the number of the manufactured transistors on a chip would be doubled every 18 months, boosting the performance of electronic devices[1-3]. This strategy had been successfully employed for more than 4 decades, until it started to be hindered by technological and phenomenological problems[3,4]. Difficulties in the heat dissipation of the circuits which have extremely high densities of nano-sized transistors, unreliabilities arising from quantum uncertainties (in sub-nanometer regimes)[5,6], and the unreasonably high price of the instrumentation required for the fabrication of ultra-small devices[7,8] made the Moore's law deviate from its original roadway.

In order to address this issue, several ideas have been suggested and investigated. One possibility is to keep the current computing techniques and the current materials (mainly silicon), and improve the performance by forming 3D structures, instead of limiting the circuits to flat chips. This method has been employed intensively, especially for low energy applications such as memories[9-11].

In parallel, many research groups try to replace silicon by other materials to fabricate new electronic components. The emergence of carbon nanotubes and graphene as 1D and 2D semiconductors attracted huge attention to low dimensional materials, introducing them as promising alternatives for the current electronic materials. This field has been further developed by using other 2D materials such as transition metal dichalcogenides (TMDs). Due to quantum confinement, these materials exhibit novel physical properties which might help to overcome the limitations of the conventional systems[5,12,13].

Eventually, harnessing new logic paradigms has been suggested, as an ultimate solution to revolutionize the computing. Examples of such methods are quantum computing and neuromorphic computing[5,12,14,15]. In quantum computers, all the calculations are performed based on quantum mechanical phenomena (for example the propagation of the carriers' spin direction); instead of classical ones (e.g. motion of electrons). This leads to significant improvements of the calculation speed, functionality, and efficiency of the devices[12,14,16]. In the neuromorphic computation, large scale analog/digital circuits are employed to mimic neuro-biological architectures present in the nervous system[15,17,18]. Although concepts like quantum computing and neuromorphic computing promise substantial advantages over the

existing systems, so far their functionality has not been able to go beyond the laboratory level[5].

1-1-1 The emergence of two-dimensional semiconductors

As mentioned before, the development of 2D semiconductors introduced new solutions for the future of semiconductor technology. These nanomaterials are important in two aspects: First, they can improve the performance of the conventional transistors due to their superior properties which originate from their low dimensionality[19,20]. Second, their novel physical properties result in new degrees of freedom which can be used as new logic paradigms. For instance, manipulating the spin degree of freedom (SDoF) and the valley (local extrema on the valence/conduction band with equal energy levels) degree of freedom have been introduced for modern computing[21-23].

Graphene was the first investigated material in the field of 2D electronics, a single layer of hexagonally arranged carbon atoms which shows extraordinary properties, including high carrier mobility and significant mechanical stability[24-26]. Unfortunately, field-effect transistors (FETs) based on graphene did not represent acceptable gating effects due to its zero bandgap. A possible solution for this problem was cutting the graphene flakes to narrow ribbons, which led however, to the reduction of the mobility[26-28]. The other possibility was using other 2D materials instead of graphene. For instance, MoS_2 and other TMDs have been investigated intensively. They showed to have high carrier mobilities (still lower than graphene) and at the same time, very effective gateabilities due to their sizeable bandgap[29-31]. Their band structure normally contains several valleys. Since the number/spin of the carriers in each valley can be externally controlled, these materials are also considered for spintronics/valleytronics[32-34].

Different kinds of 2D materials are conventionally produced either by means of expensive instrumentations, like chemical-vapor deposition (CVD) and molecular-beam epitaxy (MBE) machines, or with very low output methods like mechanical exfoliation[35,36]. Although they have shown remarkable properties, producing them with cost-effective methods and in industry compatible scales has remained difficult. Establishing new methods to reduce their production costs seems to be critical.

1-2 Colloidal synthesis of nanocrystals

One of the promising methods to produce different nanomaterials is the colloidal approach. This method has distinct advantages which make it superior to other techniques. It is very cost effective, since it requires no expensive instrumentations (as it will be discussed later)[37-39]. The crystal quality of its products is very high[37,40]. It represents a great degree of flexibility, since the products can be tuned in terms of size, shape, and properties simply by altering the synthesis conditions[40,41]. Eventually, it can be used to produce high amounts of nanomaterials, which makes it suitable for industrial applications[40]. Colloidal nanomaterials can be stored in different media as suspensions, and handled with simple methods like drop casting, spin coating, or ink-jet printing for device preparation[37,38].

In a colloidal synthesis, the reactants must be dissolved in the proper solvents and mixed while the temperature is accurately controlled. The reaction temperature must be high enough to promote the decomposition of the reactants (precursors) and the production of the monomers (nucleation), but low enough to stimulate the growth of the formed nuclei by limiting the nucleation. By injecting the reactants into the reaction mixture, the concentration of the precursors raises above the nucleation threshold. At this step, in which the complex is supersaturated, the nucleation starts and small nanocrystals (NCs) are formed. The formation of these nuclei reduces the concentration of the precursors, and brings it to a level lower than the nucleation threshold. As a result, the formation of new nuclei stops and the remaining precursors are used to grow the previously formed nuclei. Eventually, the precursors' concentration approaches a constant value and the grown NCs become stable. This scheme is graphically illustrated by the La Mer plot, shown in Fig. 1[40,42].

At the end of the growth phase, the NCs should be stabilized. Otherwise, they agglomerate and only macroscopic materials are obtained. This can be done by ligands, organic or inorganic molecules (like oleic acid or chloride) which are attached to the surface of the NCs through covalent, dative, or ionic bonds and passivate it. Figure 2 schematically illustrates that how the ligands cover the surface of the NCs to keep them away from each other and to prevent the agglomeration. In addition, these capping agents control the nucleation and growth by adjusting the reactivity of the precursors, modify the growth by passivating crystal facets, stabilize the NCs in the solution, and passivate their electronic surface states[37,42].

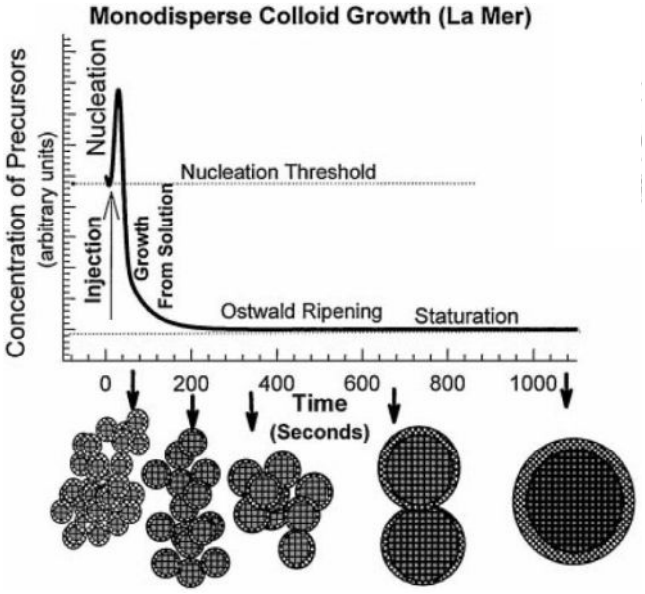

Figure 1. Nucleation and growth of the nanocrystals in a typical colloidal synthesis. The concentration of the precursors increases to higher than the nucleation threshold after the injection and decreases again after the formation of nuclei. It approaches a constant value at the end of the synthesis after the growth phase. The figure was adopted from[42].

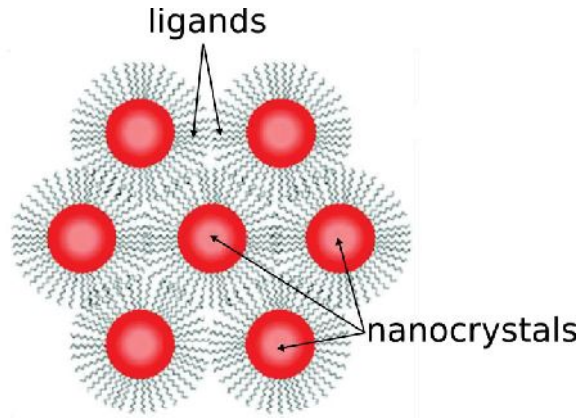

Figure 2. Nanocrystals (shown as red spheres) capped with ligands (wavy black lines). These ligands prevent the agglomeration by keeping the nanocrystals away from each other. The figure was adopted from[43].

1-2-1 Oriented attachment and synthesis of colloidal 1D or 2D materials

The growth mechanism of colloidal NCs is not limited to the previously mentioned one. It has been observed that the formed NCs can also attach to each other before the stabilization

phase. The controlled attachment of NCs (oriented attachment) can be employed to make complex structures[44]. The main driving force for this phenomenon is the energy difference between the NCs' surface facets. This mechanism includes the rotation of the NCs, such that their high energy surface facets are aligned, and then they attach to each other to minimize the surface energy of the system[45].

The formation of PbS nanosheets (a narrow bandgap semiconductor [bandgap: 0.41 eV] with a rock-salt crystal structure[46], with interesting properties such as a rather large Bohr exciton radius of 18 nm[47] or the possibility of carrier multiplication[48], and with promising applications such as FETs[49] or solar cells[50]) is an example of oriented attachment, which further clarifies this type of growth mechanism. During the synthesis, first small truncated cubes are formed. They contain 6 {100}, 8 {111}, and 12 {110} facets, while the {110} facets show the highest reactivity compared to the other ones (Fig. 3 - section 1). This difference in the reactivity aligns the cubes through the highly reactive {110} facets. Then, the aligned NCs attach to each other and form bigger structures like nanosheets. Figure 3 schematically shows the alignment of the NCs and the formation of a nanosheet from these cubes[51].

At this point of the synthesis, ligands play a crucial role. When the properly aligned NCs are attached to each other, oleic acid, the used ligand for this synthesis, passivates the {100} facets since these facets are the most favorable ones for oleic acid to be adsorbed to. In this condition, passivating the {100} facets, which are the top and bottom parts of the formed structure, stops the growth in the third dimension (height of the sheet). Therefore, the structure only grows laterally by the attachment of the NCs, which results in the formation of a 2D crystal[51].

Such nanosheets grow in the (110) direction, and as mentioned, their top and bottom surfaces are the {100} facet[51,52]. By changing the amount of the main ligand (oleic acid) in the synthesis, which modifies the stability of the top and bottom surfaces, the thickness of the sheets can be tuned between 2 to 20 nm. The lateral size of the sheets is normally higher than 2 µm[52]. By adding relatively high amounts of chloroalkane to the synthesis, which normally acts as a second ligand, the stabilization of the NCs becomes more effective. Therefore, the structures grow mainly in one direction. The products of this synthesis are quasi 1D stripes with the length of around 5 µm and the width of less than 100 nm[53]. Figure 4 shows examples of the sheets and the stripes, produced with the above mentioned methods. It has been recently shown that even other halogenoalkanes can be employed to synthesize PbS

nanosheets. Most of the employed halogenoalkanes had similar influences on the shape and the size of the products[54].

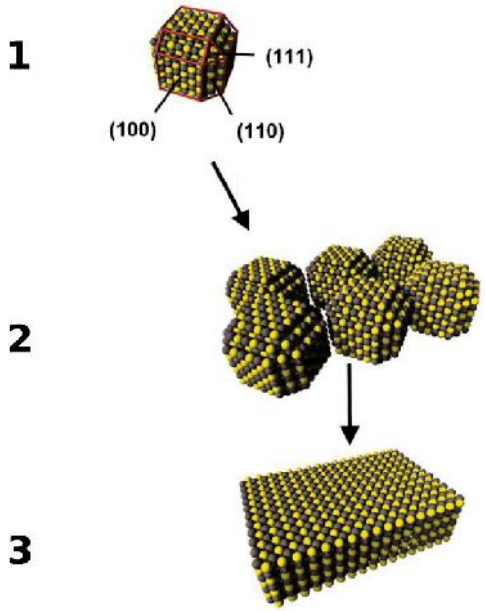

Figure 3. Formation of PbS nanosheets by the oriented attachment. First the truncated cubes are produced (step 1). Then, they align (step 2) and attach to each other through the highly reactive {110} facets and form the sheets (step 3). The figure was adopted from[51].

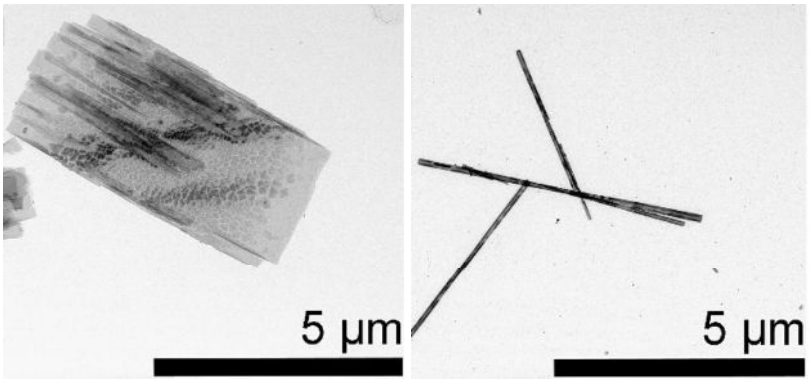

Figure 4. Transmission-electron microscope (TEM) images of the PbS nanosheets (left) and stripes (right), made by the oriented attachment. The thickness of the nanosheets is tuned between 2 to 20 nm by changing the amount of the main ligand (oleic acid), while increasing the amount of the coligand (chloroalkane) promotes the quasi-one dimensional growth[52,53]. The figures were adopted from[53].

There are other examples of oriented attachment, leading to the formation of other shapes. By adjusting the reaction conditions, it is possible to convert the truncated cubes, which are formed in the beginning of the synthesis, into octahedra. As can be seen schematically in Fig. 5a and in the high resolution transmission-electron microscope (HRTEM) images in Fig. 5b, these octahedra attach to each other through the {100} facets and make a special form of wires with a zigzag shape (Fig. 5c). The length of these wires can reach to 15 µm. Their growth direction is (100) while their surface facets are {111}, similar to the surface of their octahedral building blocks[55-57].

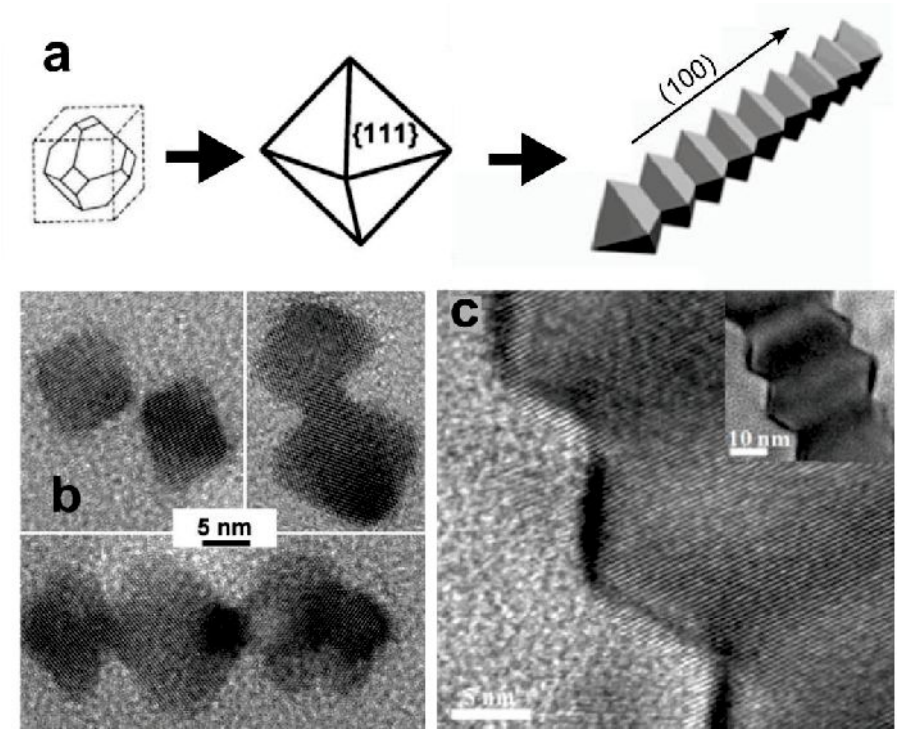

Figure 5. Attachment of octahedra and formation of zigzag wires. (a) At the beginning of the synthesis, the truncated cubes are transformed into octahedra, which attach to each other through the {100} facets and form a wire in this direction. The figure was adopted from[55,56]. (b) HRTEM images of the oriented attachment of octahedra, explained in part a. Adopted from[55]. (c) HRTEM image of the formed zigzag wire after the attachment. The inset shows the TEM image of the same wire with a lower magnification. Adopted from[56].

The especially important point about these wires is that their surface facets (the {111} facets) include only one element, in contrast to the surface of the normal sheets and wires (the {100} facets). The arrangement of the Pb and S atoms in different facets can be observed in Fig. 6.

In the {100} facet and the {110} facet, both elements are present with different arrangements. However, the {111} facet is a single element facet (either with Pb or S)[58,59].

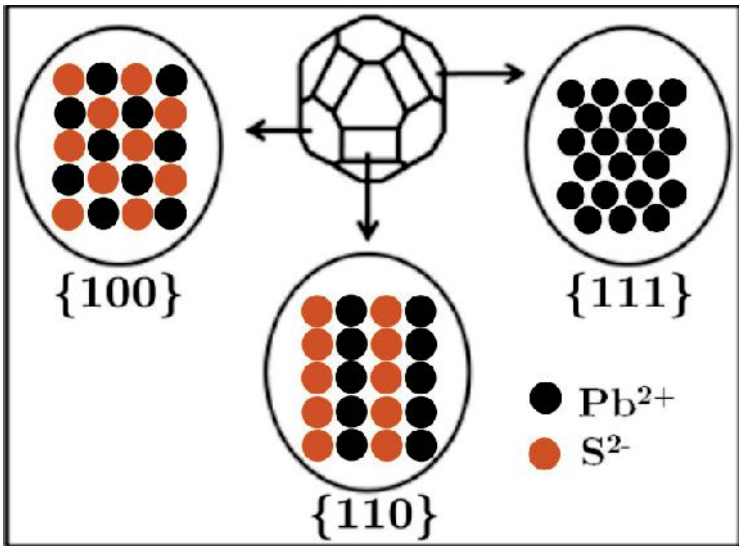

Figure 6. Arrangement of atoms in different facets of the PbS crystal. It is like a chess board in the {100} facet. In the {110} facet, both elements are present in rows. In contrast, the {111} facet contains only one element. The figure was made by the author.

1-3 Electronic properties of nanomaterials

As already discussed, there are several motivations for employing semiconducting nanomaterials. In the following section, more details about the fundamental properties of nanomaterials will be provided and the benefits of low dimensionality will be discussed.

1-3-1 Electronic band structure

If an isolated atom is considered, its electrons would have discrete energy levels around the nucleus. These energy levels for a hydrogen atom can be calculated based on the Bohr model by Eq. 1:

$$E_H = -m_0 q^4 / 8\varepsilon_0^2 h^2 n^2 \qquad (1)$$

Here, m_0 is the free electron mass, q is the unit electronic charge, ε_0 is the permittivity of vacuum, h is the Planck constant, and n is a positive integer representing the quantum number. By taking the principal quantum number into account, every energy level would be a doubly degenerate level[60].

In this condition, if a similar atom comes closer to this atom, every doubly degenerate energy level will spilt to two levels as a result of the interactions between the atoms (attraction and repulsion forces). Similarly, if *N* atoms approach each other, the interactions between the orbitals become more pronounced and therefore, the energy levels split to *N* closely spaced levels. When *N* is large enough, these splitted levels form an energy band[60]. This effect is schematically shown in Fig. 7.

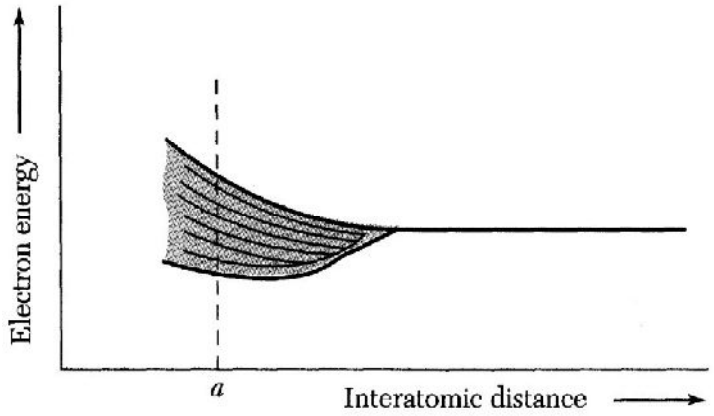

Figure 7. Splitting of the energy levels when *N* atoms approach each other. Here *a* represents the equilibrium interatomic distance of the crystal. The figure was adopted from[60].

If the system contains more complex atoms, silicon atoms instead of hydrogen for instance, the band splitting would be different. By reducing the distance between the silicon atoms, there would be interactions and overlaps of the 3s and 3p subshells. As can be seen in Fig. 8, at the equilibrium interatomic distance, the formed bands split and each splitted band would have 4*N* states. When there is no thermal excitation (at 0 K), electrons occupy all the states in the lower band (which is called the valence band), whereas the states in the upper band (the conduction band) remain empty. Here, the important parameter is the energy difference between the bottom of the upper band and the top of the lower band. This energy range contains no states and therefore, it is called the forbidden energy gap or the bandgap. This parameter is equal to the required energy to free an electron in the conduction band[60].

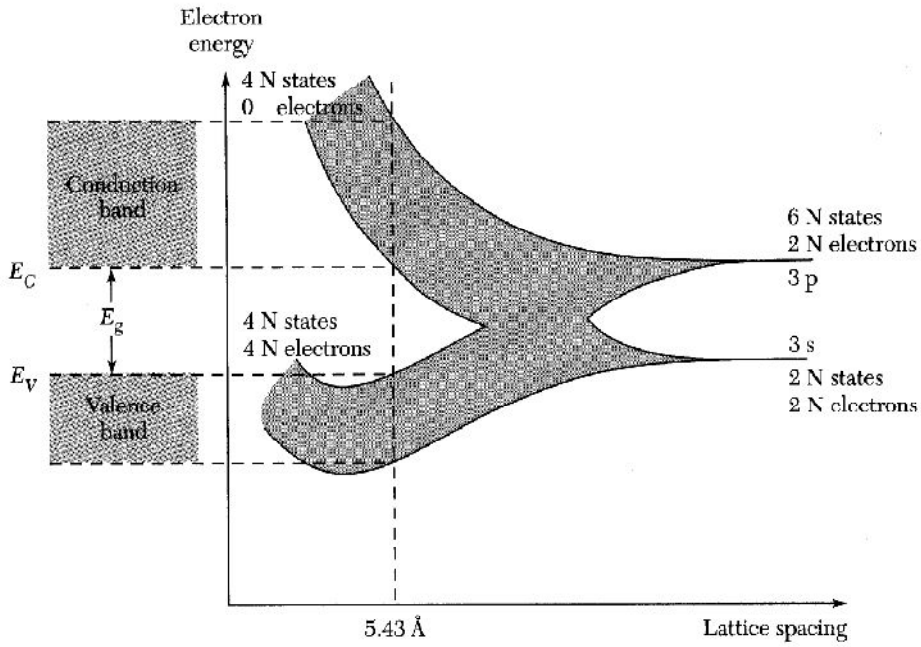

Figure 8. Splitting of the energy bands by reducing the interatomic distances in a silicon crystal. At the equilibrium interatomic distance, the energy difference between the lower band and the upper band is called the bandgap. The figure was adopted from[60].

The energy of an electron in the conduction band is calculated by Eq. 2:

$$E = \frac{P^2}{2m_n} \qquad (2)$$

In this equation, P is the momentum and m_n is the effective mass (also can be shown as m^*) of the electron, which differs from the real electron mass due to the periodic potential of the nuclei in the crystal. A similar equation can be also derived for the holes (the remaining empty states when electrons are excited to the conduction band). These two equations can be employed to plot the simplified band structure of a material (a direct semiconductor), as shown in Fig. 9[60].

For many materials like silicon, the energy-momentum relationship is more complex. For these materials (indirect semiconductors), the maximum of the valence band and the minimum of the conduction band do not occur at a same momentum. Therefore, an electron

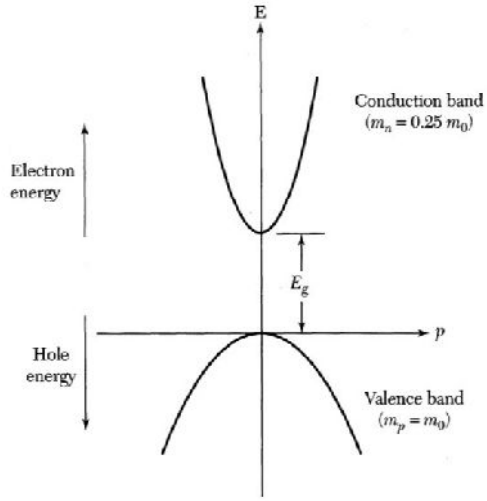

Figure 9. Simplified band diagram of a material based on the effective mass of electrons and holes. The figure was adopted from[60].

which is excited from the valence band top to the conduction band bottom should gain momentum in addition to energy. For silicon, as shown in Fig. 10, the minimum of the conduction band occurs along the (100) direction while the maximum of the valence band is at $P = 0$[60].

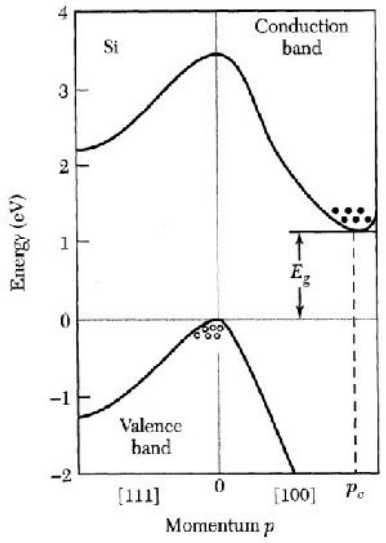

Figure 10. Band diagram of silicon as an indirect semiconductor. The minimum of the conduction band occurs along the (100) direction and the maximum of the valence band is at $P = 0$. The figure was adopted from[60].

For a material like PbS, both extrema occur along a certain direction (the (111) direction) and not at $P = 0$. Therefore, it is also considered as a direct semiconductor[61]. The band structure of PbS is shown in Fig. 11.

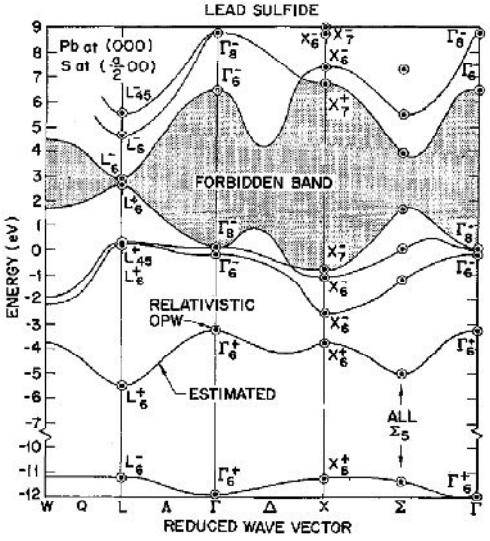

Figure 11. Band diagram of PbS. As a direct semiconductor, the bandgap occurs along the (111) direction (corresponding to the L point) and not at $P = 0$ (the Λ point). The figure was adopted from[61].

The other important parameter which can be derived to describe the electronic properties of a material is the density of states (DOS). The DOS represents the distribution of the available quantum states which can be filled by an electron (based on the Pauli exclusion principle, only one electron can occupy a quantum state). The DOS can be employed to calculate the concentration of the available carriers for the transport, or eventually, the conductivity of the material[62]. The DOS for the conduction band is calculated by Eq. 3.

$$g_c(E) = \frac{m_n^* \sqrt{2m_n^*(E-E_c)}}{\pi^2 \hbar^3} \qquad (3)$$

In this equation, E_c is the bottom of the conduction band, and $\hbar = h/2\pi$. A similar equation is also valid for the valence band. By using these equations, one can plot the DOS for different energy levels. As can be observed in Fig. 12, the DOS is zero in the bandgap and also at E_c or E_v. It increases as the square root of the energy, for the energies higher than E_c or lower than E_v[63].

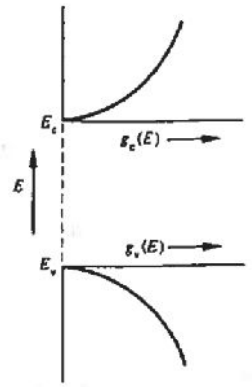

Figure 12. Density of states for different energy levels. It is zero in the bandgap and increases as the square root of the energy in the conduction band or the valence band. The figure was adopted from[63].

The probability of occupying a state with the energy of E can be derived by the Fermi-Dirac distribution function, represented in Eq. 4.

$$F(E) = \frac{1}{1+e^{(E+E_F)/kT}} \qquad (4)$$

Here, k is the Boltzmann constant, T is the temperature, and E_F is the energy of the Fermi level, at which the probability of the occupation by an electron is exactly one-half. The combination of the DOS and the Fermi-Dirac distribution is employed to obtain the carrier concentration[60].

1-3-2 The size effect on electronic properties

In bulk materials, free carriers can move freely in the entire crystal (as a quasi-infinite platform for the transport). By reducing the size of the crystal, carriers are confined in certain directions and therefore, electronic properties are altered. The quantum confinement occurs in three dimensions for 0D nanoparticles, in two dimensions for 1D nanowires, or just in one dimension for 2D nanosheets. By decreasing the size of the confined dimensions or by increasing the number of the confined dimensions, the deviation from the properties of the bulk material becomes more pronounced.

First of all, the bandgap of the material increases by intensifying the quantum confinement. This can be clearly observed, for instance, by reducing the size of CdSe nanoparticles. The emission of this material which is normally red, can be tuned continuously to blue by

decreasing the size of the particles and thus, increasing their bandgap[41]. The shift in the emission of CdSe nanoparticles (passivated with a ZnS shell) is shown in Fig. 13.

Figure 13. Continuously shifting the emission of CdSe nanoparticles (passivated with a ZnS shell) from red to blue by reducing the size of the particles and increasing the bandgap. The figure was adopted from[64].

Confining the crystal also modifies its DOS. By considering Eq. 5, it is possible to estimate the DOS based on the dimensionality of the crystal.

$$g(E) = E^{\frac{D}{2}-1} \qquad (5)$$

Here, *D* shows the dimensionality of the crystal. Based on this equation, the DOS is derived for different forms of a crystal as it is shown in Fig. 14. In 3D crystals (bulk), the DOS increases smoothly by increasing the energy. In nanosheets or other forms of 2D materials, it increases like a staircase. The DOS of 1D materials (nanowires) has a saw-tooth form. Eventually, the DOS of 0D nanoparticles is a δ-function of the energy[41].

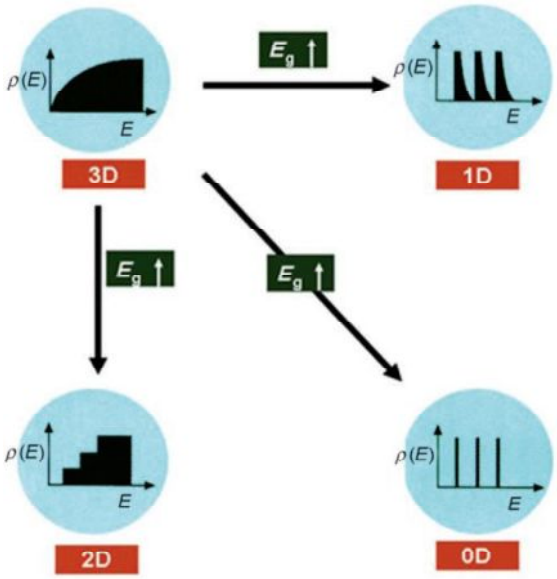

Figure 14. The density of states for different forms of a crystal. It changes from a smooth function of the energy in 3D materials to a discrete δ-function for 0D nanoparticles. The figure was adopted from[41].

1-3-3 Electrical transport through nanomaterials

In general, the charge transport (movement of carriers) in a material occurs as a consequence of a gradient in the Fermi level. These movements can be the carriers' drift (due to an electric field) or their diffusion (because of their concentration gradient)[65]. Under an electric field, electrons accelerate according to Eq. 6.

$$F = m^* \frac{d\boldsymbol{v}}{dt} = \hbar \frac{dk}{dt} = -e\boldsymbol{E} \qquad (6)$$

Where m^* is the effective mass, $\boldsymbol{v}$ is the velocity of electrons, k is the momentum, t is the time, e is the electron charge, and $\boldsymbol{E}$ is the electric field. Without considering the ballistic regime (transport without scattering), the maximum drift velocity (given by Eq. 7) depends on the relaxation time τ, which sums up all the scattering events (impurities, phonons, and defects). The relaxation time (τ) is the required time for carriers to travel as long as the mean-free path (λ)[65].

$$\boldsymbol{v} = -\frac{e\boldsymbol{E}\tau}{m^*} \qquad (7)$$

Therefore, the current density is (Eq. 8):

$$j = nq\boldsymbol{v} = \frac{ne^2\boldsymbol{E}\tau}{m^*} = \sigma\boldsymbol{E} \quad (8)$$

In this equation, n is the number of the carriers and σ is the conductivity. By rewriting Eq. 8, the conductivity relaxation-time approximation is derived (Eq. 9).

$$\sigma = \frac{1}{\rho} = \frac{ne^2\tau}{m^*} \quad (9)$$

In this equation, σ and ρ are respectively the conductivity and the specific resistivity. The mobility of the carriers which is defined by Eq. 10 can be also employed to calculate the conductivity (Eq. 11).

$$\mu = \frac{v}{\boldsymbol{E}} \quad (10)$$

$$\sigma = qn\mu \quad (11)$$

These equations are valid for both carriers' types and only for the low-field regime, in which the velocity is proportional to the electric field[65].

The mobility is consequently calculated according to the relaxation-time approximation (Eq. 12).

$$\mu = \frac{q\tau}{m^*} \quad (12)$$

Although the conductivity of metals is generally higher than semiconductors, the mobility of semiconductors can be much higher[65].

By reducing the dimensionality of the crystal, several phenomena modify the transport, including the surface scattering, the quantized and ballistic conduction, Coulomb charging and tunneling, and widening and discrete of the bandgap. Further, the conductivity can be affected by the increased perfection of the nanoscale crystals, for instance by the reduction of impurities, structural defects and dislocations[66].

In bulk semiconductors, the mean-free path which determines the conductivity is in the range of tens to hundreds of nanometers. When the size of the crystal is reduced to lower than this

range, the role of surface scattering becomes more important than other types of scattering (defects or phonon scattering). In this condition, the motion of electrons is interrupted by their collision to the surface of the crystal. If electrons experience elastic scattering, their energy and their momentum along the direction of the motion are preserved. Therefore, the conductivity of the crystal remains similar to the bulk material. In contrast, inelastic scattering terminates the mean-free path of electrons. After the collision, they lose their velocity along the conduction direction, since the electrons' scattering angle is random, and therefore, the conductivity decreases[66]. For a crystal with the thickness smaller than the mean-free path (for example a nanosheet), the Thompson model is employed to calculate the resistivity (or conductivity), which is given in Eq. 13.

$$\frac{\rho_0}{\rho_f} = \frac{d}{2\lambda_0}\left(\ln\left(\frac{\lambda_0}{d}\right) + \frac{3}{2}\right) \qquad (13)$$

In this equation, ρ_0 is the resistivity of the bulk material, ρ_f is the resistivity of the film, λ_0 is the mean-free path of the bulk material, and d is the thickness of the film. In this model, all the surface scattering events are assumed to be inelastic scattering. In order to consider the elastic scattering events, the Fuchs-Sondheimer (F-S) theory can be employed to derive a more accurate relation (Eq. 14).

$$\frac{\rho_0}{\rho_f} = \frac{3d}{4\lambda_0}(1 + 2P)\left(\ln\left(\frac{\lambda_0}{d}\right) + 0.423\right) \qquad (14)$$

Here, P shows the fraction of elastic surface scattering. Surface impurities and roughness increase the possibility of inelastic scattering[66].

Reducing the dimensionality of the crystal alters the conductivity also by increasing its bandgap. It has been observed that this effect increases the resistivity of the material. Even in extreme cases, transitions from the metallic to semiconducting or from the semiconducting to insulating state have been observed[66].

The transport through the systems with higher degrees of confinement (0D nanoparticles) normally experiences more size related modifications. The ballistic conduction occurs when the conduction length is smaller than the mean-free path, and electrons travel without being scattered. Therefore, the phenomena which are dependent to the coherence of the transport can be exploited. Further, the Coulomb blockade is observed when the capacitance of the crystal is so small that a big amount of energy is required to add one electron to the system.

Therefore, the system would have discrete charging energies. The availability of such discrete charging energies or the so called Coulomb staircase makes it possible to realize the concept of single-electron transistors based on the nanoparticles with the diameter of less than 2-3 nm, and by adding a gate electrode to the system. Eventually, the tunneling conduction is the other effect which plays a crucial role in the conductivity of low dimensional materials. When two conductors, separated by a dielectric layer, are very close to each other, their electron wave functions overlap inside the dielectric layer. As a result, charges can flow through the dielectric layer when an electric field is present. The conductivity of the dielectric layer decreases exponentially by increasing its thickness (the distance between the conductors)[66].

1-3-4 Semiconductors in contact with metals

In ideal cases and without considering the surface states, there will be a charge flow form an n-type semiconductor to a high work-function metal when they get in contact with each other. In this condition, the Fermi level of the semiconductor must be lowered in order to line up with the work function of the metal. Therefore, the bending of the semiconductor Fermi level would be equal to the difference in the work function of the metal and the semiconductor[67].
This bending results in the formation of a potential barrier for electrons. The height of this barrier ($q\Phi_{Bn0}$) is equal to the difference between the metal work-function ($q\Phi_m$) and the electron affinity (qX) of the semiconductor (Eq. 15). Similarly, Eq. 16 is used to calculate the barrier height for a p-type material.

$$q\emptyset_{Bn0} = q(\emptyset_m - \chi) \quad (15)$$

$$q\emptyset_{Bp0} = E_g - q(\emptyset_m - \chi) \quad (16)$$

The sum of these two barriers is equal to the bandgap of the semiconductor (E_g)[67]. The metal-semiconductor contact and the formation of the potential barrier are schematically shown in Fig. 15.
In practice, the height of the metal-semiconductor potential barrier varies significantly from the theoretical expectations due to the surface contaminations, the unavoidable interface layer, and the surface states[67].

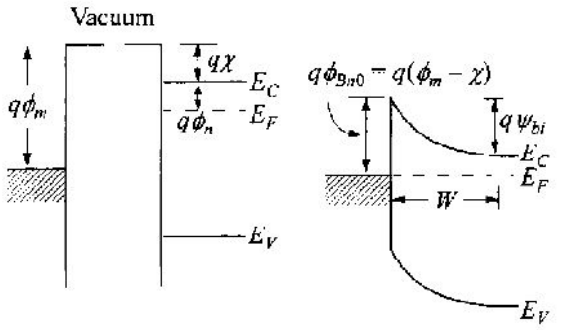

Figure 15. The band alignment of a semiconductor in contact with a metal. A potential barrier is formed since the Fermi level of the semiconductor should line up with the work-function of the metal. The figure was adopted from[67].

After the band alignment at the metal-semiconductor junction, the charge transport can occur in five different ways. As can be observed in Fig. 16, one possibility for electrons is to overcome the potential barrier and move from the semiconductor to the metal over the barrier (1). This type of transport which is called the thermionic transport can only happen when electrons have the required energy to climb the potential barrier at the junction. The transport from high mobility semiconductors (Si or GaAs) to metals is normally thermionic. The other way of transport is quantum mechanical tunneling through the barrier (2). This is normally the case for heavily doped semiconductors and helps to establish Ohmic contacts (will be discussed later). By increasing the doping level of the semiconductor, the width of the potential barrier becomes smaller and therefore, electrons would be able to tunnel through it more easily. Alternatively, electrons can recombine with the holes which are provided from the metal side (3). Electrons can also diffuse into the depletion region, which is the area under the potential barrier (4). Eventually, holes as minority carriers can be injected from the metal to the semiconductor and diffuse there (5). In order to achieve the transport by the minority carriers, the system must have an adequate forward bias[67]. All of these possibilities are schematically depicted in Fig. 16.

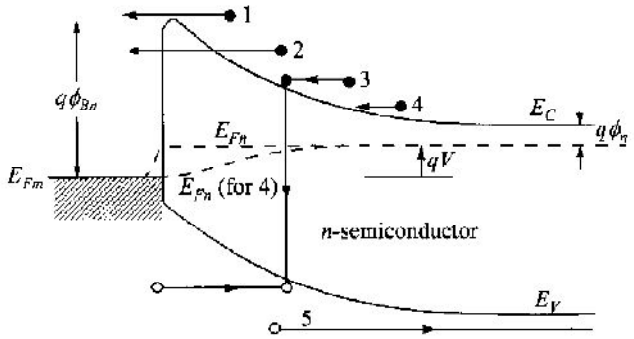

Figure 16. The possible mechanisms for the charge transport between an n-type semiconductor and a metal. (1) Thermionic emission, (2) tunneling, (3) recombination, (4) diffusion, and (5) diffusion of minority carriers. The figure was adopted from[67].

After the formation of the contact between a metal and a semiconductor, it would be an Ohmic contact when it has a negligible resistance compared to the total resistance of the device. Such contacts do not significantly perturb the functionality of the device since they supply a current without any considerable voltage drop. To evaluate the contact resistance, Eq. 17 can be employed at zero volt bias regime[67].

$$R_c = \left(\frac{dJ}{dV}\right)^{-1}_{V=0} \qquad (17)$$

In this equation, J is the current density and V is the bias voltage. In order to investigate the contact resistance, the transport mechanism of the system must be considered. The transport mechanism itself depends normally to the Schottky barrier height, the temperature, and the doping level of the semiconductor. Therefore, these are the important parameters to establish a low resistance contact. For this purpose, the metal is normally selected accordingly, in order to make the barrier height as low as possible. Increasing the doping level of the semiconductor is also helpful, although it might also alter other properties of the system. Doping is especially beneficial for the wide gap semiconductors, since the work-function of metals are never low enough to form an Ohmic contact with them. Adding a layer of a small bandgap material to make a heterojunction is the other possibility to modify the band alignment and to improve the contact[67]. This strategy can be also implemented by employing graphene or other 2D materials in order to reduce the contact resistance between metals and semiconductors[68,69].

Establishing Ohmic contacts to colloidal materials is more complicated compared to physically grown semiconductors. Their surface is normally covered with long organic

ligands, which could dramatically hinder the transport, especially when thin films of nanoparticles are used instead of individual crystals[70,71]. Calculations have revealed that when a high work-function metal like Au is used to contact PbS nanosheets, the band alignment is such that an Ohmic contact is established for holes, and a Schottky barrier is formed for electrons, as it is shown in Fig. 17[49].

The band alignment can be modified by changing the work-function of the contact metal. By decreasing the work-function, the transport of electrons would be improved while the transport of holes is hindered. For instance with Ti, an Ohmic contact is formed for electrons. When the work-function of the metal is extremely high, for instance with Pt, the formed Schottky barrier for electrons becomes very narrow, which promotes the tunneling of electrons[50]. The alignment of the PbS bands in contact with different metals is shown in Fig. 17.

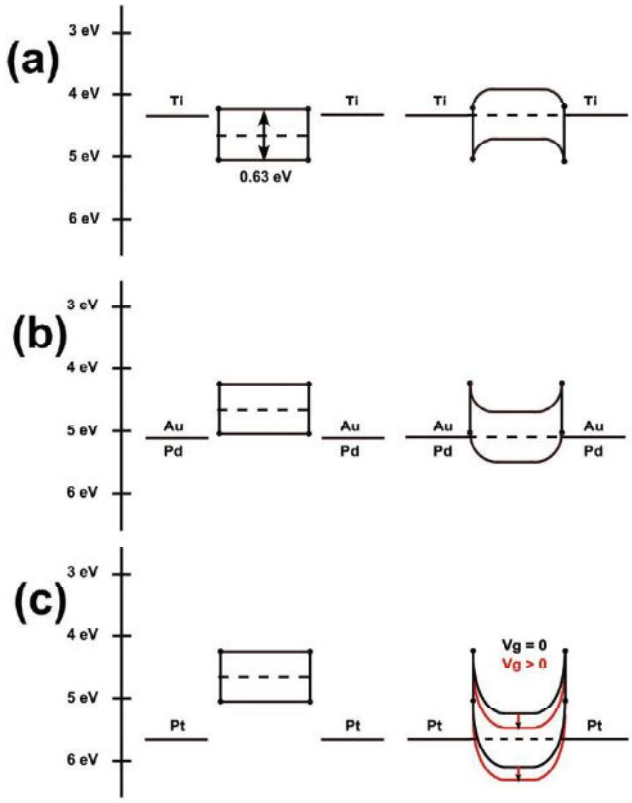

Figure 17. Band alignment of PbS in contact with different metals. (a) With Ti as a low work-function metal, an Ohmic contact is formed for electrons. (b) Au and Pd have higher work-functions compared to Ti. In contact with PbS, they establish Ohmic contacts for holes and Schottky barriers for electrons. (c) With Pt which has a very high work-function, very narrow Schottky barriers are formed for electrons. The figure was adopted from[50].

As a result of the band alignment, PbS nanosheets show p-type behavior in contact with Au, due to the formation of Ohmic contacts for holes. At low temperatures, the conductivity of the sheets decreases and their on/off ratio (the ratio between the on current and the off current) increases. The field-effect mobility of these nanosheets reaches to 0.417 cm^2/Vs at room temperature while their on/off ratio is 3 and their conductivity is 72.06 mS/cm[49]. The FET behavior of theses sheets can be observed in Fig. 18.

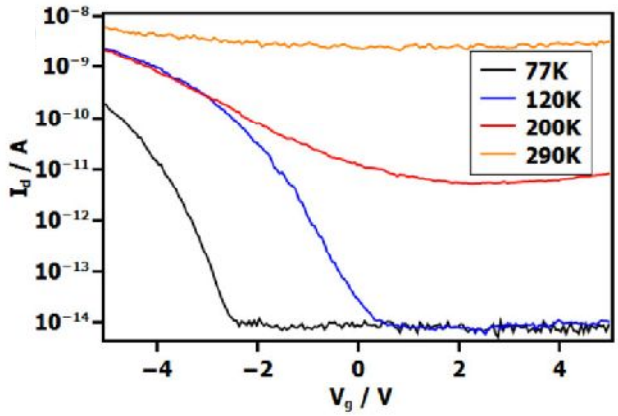

Figure 18. Transistor behavior (transfer characteristics) of an individually contacted PbS nanosheet (with Au). P-type behavior is observed with higher on/off ratios at low temperatures. The figure was adopted from[49].

It should be pointed out that the thickness of the nanosheets plays a crucial role in their performance as FETs. It has been observed that thinner sheets have lower conductivities but higher on/off ratios compared to thicker sheets. The reason for that is the increase of the bandgap by the quantum confinement, which also modifies the band alignment between the crystal and the contact metal[52]. A comparison between the functionality of differently thick sheets can be observed in Fig. 19.

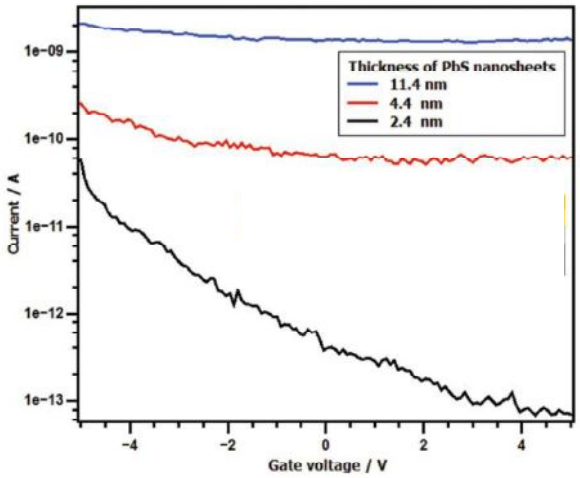

Figure 19. The thickness effect on the electrical properties of individually contacted PbS nanosheets. By reducing the thickness, the conductivity decreases while the on/off ratio increases. The figure was adopted from[52].

1-4 Spintronic properties of nanomaterials

As mentioned in section 1-1, one possibility for the modern data processing is harnessing new logic paradigms. For example, the spin degree of freedom can be employed instead of the carriers' charge[72,73]. This method has been commercially used for some years through magnetic metals and based on the tunnel magnetoresistance (TMR) and giant magnetoresistance (GMR) effects. As a result, the read head of hard disks can transfer data by means of the SDoF[73,74].

Compared to metals, manipulating the spin could be more complicated in semiconductors. The most fundamental effect which is used to control the SDoF in semiconductors is the spin-orbit coupling (SOC)[72,75]. When electrons, as charged particles, move in the electric field of the nucleus, they feel a magnetic field proportional to their velocity and to the amplitude of the electric field. This magnetic field interacts with the magnetic moment of the electrons. These interactions are the origin of the SOC. According to the definition of the SOC, it is more pronounced for heavy atoms (atoms with high atomic numbers). The SOC results in splitting the atomic levels based on the spin direction of the carriers[76].

Based on this phenomenon, the concept of the spin FET has been proposed, in which spin polarized charges are injected to a narrow bandgap semiconductor by magnetic contacts and are controlled by an electric field (since the SOC can be affected by an electric field)[77,78].

Compared to the SFET concept, the more efficient way to establish a non-equilibrium spin direction in a semiconductor is through the selective interband excitation of carrier. This is

achieved by the illumination of circularly polarized light, which carries spin. In this condition, the spin of photons is transferred to the charge carriers in the semiconductor.

By considering the angular momentum of the splitted sub-bands (due to the SOC), the selection rule for this excitation can be obtained. The angular momentum is equal to ±1/2 for the s orbital (the conduction band, atomic orbital number: 0) and to ±1/2 and ±3/2 for the p orbital (the valence band, atomic orbital number: -1, 0, +1). During the excitation, the energy and the angular momentum must be conserved. In other words, in addition to the energy of photons, their angular momentum must be transferred to the carriers. As can be seen in Fig. 20, the angular momentum of photons, which is considered to be +1, is added to the initial angular momentum of the electrons. By tacking the probability of each transition into account (shown in the circles), it can be observed that the excited carriers would have a net angular momentum (spin)[76].

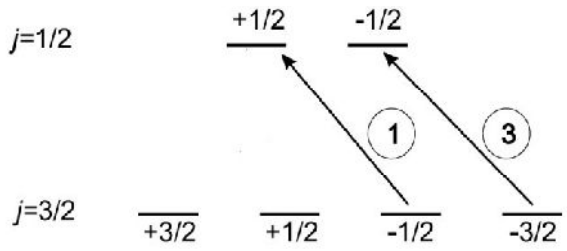

Figure 20. Possible optical transitions and their probability (shown in the circles) for illumination with circularly polarized light. When the angular momentum of photons is equal to +1(-1), the excited carriers would have a net negative (positive) angular momentum. The figure was adopted from[76].

In order to exploit the non-equilibrium spin orientation of carriers, the spin relaxation time should not be very short compared to the recombination time of the carriers, a condition which is often achievable even at room temperature[76].

The symmetry of the crystal plays a critical role for the observation of the SOC. In an inversion symmetric crystal, the effect of the SOC is compensated in different directions. Therefore, it would not be externally detectable. The inversion asymmetry, which must be present to split the bands, can be due to the intrinsic asymmetry of the crystal, the bulk-inversion asymmetry (BIA). In this case, the Dresselhaus SOC is available. Alternatively, the symmetry of a crystal can be broken externally, for example by applying a gate electric field, in order to make a structural-inversion asymmetry (SIA). This type of SOC is called the

Rashba SOC[76,79,80]. Since the Rashba SOC can be externally tuned, it is of great importance for spintronics[81,82].

1-4-1 Photogalvanic effect

When a net spin is optically injected to a semiconductor, it could be electrically measured under specific circumstances[82-84]. As previously mentioned, when a semiconductor is illuminated with circularly polarized light, some of the interband transitions would be forbidden. This is schematically depicted in Fig. 21. The valence band and the conduction band of spin-orbit coupled materials split to two sub-bands, one for the spin up and the other one for the spin down. It would be equivalent to the angular momentum of ±1/2 for the conduction band and ±3/2 for the valence band[76,85]. When the angular momentum of photons is +1, the sub-band with the angular momentum of -1/2 is populated (transition from -3/2 to -1/2) and the other one remains empty (no possible transitions to the +1/2 sub-band). In this condition, the distribution of the excited electrons in momentum space would not be symmetric and they would have a net momentum. With a continuous illumination, this net momentum can be measured externally as a net current which flows without applying any bias voltage. This effect is called the circular photogalvanic effect (CPGE) and is one of the straightforward methods to investigate the spin dependent properties, without requiring magnetic fields[76,82,86].

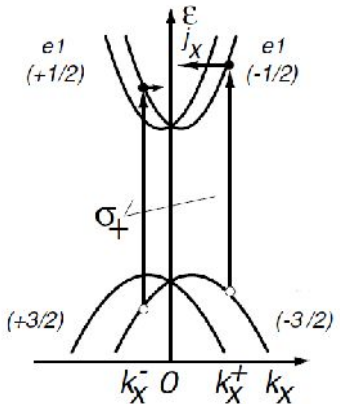

Figure 21. Circular photogalvanic effect and excitation of electrons with circularly polarized light. The bands are split according to their spin. Only one of the sub-bands can be populated, resulting in an asymmetric distribution of carriers in momentum space. The figure was adopted from[85].

In order to distinguish the spin current, produced by the SOC, from other kinds of photocurrent, the helicity of polarized light can be modulated. By changing the polarization from linear to circular, the CPGE current must change from zero to a maximum, while changing the polarization from left handed circular to right handed circular must reverse the direction of the current. To modulate the polarization of light a quarter-wave plate can be employed. Starting from 0° to higher angles, the quarter wave plate changes the polarization from linear (0°) to circular (45°), back to linear (90°), to circular but with the opposite handedness (135°), and again back to linear (180°)[83,87,88].

During this experiment, two other types of photocurrent can be also detected. A background current is always generated, which is independent of the angle of the quarter wave plate and is caused by the photovoltaic effect. Further, a current is produced by the linear photogalvanic effect (LPGE). As a result of asymmetric scattering of carriers in different directions, a current is generated which is dependent to the angle of the quarter wave plate but not to the helicity. The oscillation period of the LPGE current is π/2, while the period of the main effect (CPGE) is π[82,84,89]. The photocurrent, which is experimentally measured, is the superposition of these three effects (the background current, the LPGE, and the CPGE). This can be mathematically expressed as Eq. 18.

$$j_{total} = J_0 + J_{LPGE} \sin 2\varphi \cos 2\varphi + J_{CPGE} \sin 2\varphi \qquad (18)$$

In this equation, φ is the angle of the quarter wave plate. This equation can be used to fit the results of the photocurrent measurements. The obtained amplitude for the CPGE current shows the strength of the Rashba or Dresselhaus SOC[82,84,88].

This effect has been experimentally observed with different semiconductors. For instance, Fig. 22 shows the CPGE measurements on CdSe nanowires. The measured photocurrent (black dots) is fitted with Eq.18 in order to calculate the contribution of each effect. As can be seen, a CPGE current (the blue plot) is generated by the illumination of circularly polarized light on the spin-orbit coupled material. The LPGE and the background current are also observable as expected[82].

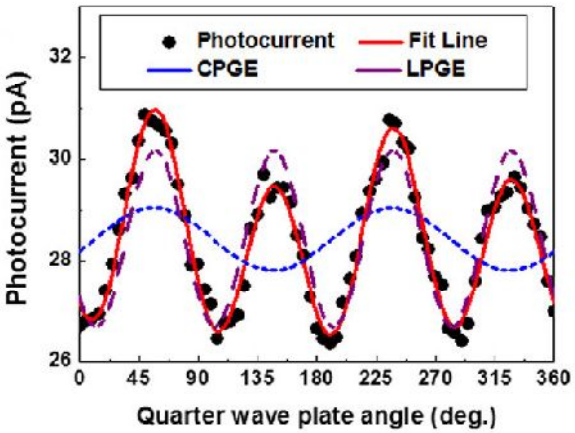

Figure 22. Experimental observation of the CPGE on CdSe nanowires. By fitting the photocurrent, the contribution of each effect is calculated. The non-zero CPGE current shows the SOC of the material. The figure was adopted from[82].

Chapter 2:

Motivation

In order to find promising solutions for the post-Moore era, two general goals have been followed in this work: 1) Introducing colloidal PbS nanosheets as new candidates for future electronics. For this purpose, the nanosheets are employed instead of silicon to make conventional transistors. 2) Suggesting these nanosheets as platforms for new concepts of data processing like spintronics.

Colloidally synthesized PbS nanosheets carry the promise of many interesting properties. As one of the first approaches, they have been employed as field-effect transistors. However, their performance has stayed far behind, compared to other 2D and layered materials or compared to the acceptable levels for industrial applications. Thus, one task would be to find any possible reasons which hinder the performance of these sheets as FETs and to find the most effective solutions to address them. The design of the PbS based FETs had to be optimized in order to improve their functionality.

In addition, other novel properties of these nanosheets had to be exploited. Their potential application in spintronics was one of the interesting topics which had to be investigated. For this purpose, a suitable test strategy had to be developed (the lateral size and the thickness of the used nanosheets or the measurement setup). Understanding the origin of the possible spin dependent properties was of great importance.

Eventually, the effect of the crystal structure on electrical properties of the sheets had to be probed. Tuning the electrical properties only by sculpting the crystal was an important method which could be employed to simply modify the NCs according to the target applications.

All of these steps would help to overcome the limitations of classical semiconductors, either by directly using PbS as the active material or by employing the obtained insights to optimize other similar systems.

Chapter 3:

Results and Discussion

(Cumulative Part)

In this chapter, the achieved results during my doctoral studies are presented in the form of scientific articles published in peer-reviewed journals. This project has been mainly conducted by using different forms of PbS nanostructures, specifically nanosheets. These nanosheets have been introduced in the work of Schliehe *et al.*, which describes the synthesis of laterally large PbS nanosheets through the oriented attachment[51]. They have been used later as field-effect transistors[49].

Here, to improve the FET properties of these nanosheets, many parameters have been modified. Firstly, by the hybrid passivation of the surface defects, huge improvements have been observed. Further, the design of the FETs (the contact metal or the crystal shape) has been optimized to realize high performance devices. This would be the first part of the project according to the previously mentioned scope (introducing a new electronic material).

To address the second target (harvesting new logic paradigms), a totally different approach has been employed. To investigate the spin dependent properties of the nanosheets, the spin polarization has been optically injected to the system and the reaction of the crystal has been electrically probed. This was the first observation of spin dependent transport phenomena through colloidal materials.

Eventually, to further understand the transport through PbS and to expand its potential application, the electrical properties of differently grown crystals (compared to the normal sheets) have been investigated in terms of conductivity, photoconductivity, and temperature dependency. The outcome of these measurements would be a complementary support to the previous studies of the system.

3-1 Reducing the width of the FET channel

The first step to optimize the FET behavior of the nanosheets is to adjust the lateral dimensions of the crystal which acts as the active channel of the FET. It has been already shown that by reducing the thickness of the sheets, which amplifies the confinement of the crystal, it is possible to increase the bandgap and thus, increase the on/off ratio of the achieved FETs, although the conductivity decreases[52].

During the synthesis of PbS NCs, one possibility to tune their size/shape is to vary the amount of the introduced chloroalkane. It has been observed that by increasing the amount of chloroalkane and due to its effect on the reactivity of different facets, the shape of the NCs is transformed from 2D sheets to quasi 1D stripes. The width of these stripes stays below 100 nm while they grow more in length (compared to the squared sheets). They are normally up

to 5 µm long. When the amount of chloroalkane in the synthesis is too high, only spherical nanoparticles are formed[53].

Electrical measurements on these stripes show clear improvements compared to the squared sheets, although the p-type character of the devices (in contact with Au) is preserved. The formation of Ohmic contacts for holes is responsible for this p-type behavior. By applying a back gate, they show pronounced gating effects. The on/off ratio of these stripes and their field-effect mobility are much higher than the previously reported values for the squared sheets. Confinement of the transport in a 1D channel results in a stronger gate influence on the conductivity, and therefore, significantly lower currents in the off state. Therefore, a better gating behavior (higher on/off ratio and higher field-effect mobility) is achieved[49,53]. This is the first step to optimize the FET behavior of this material.

3-2 Surface passivation

To further improve the functionality of the PbS based FETs, it is crucial to accurately investigate different components of such devices in order to identify the weaknesses of the system.

In this respect, the surface of the NCs is very important since it has drastic influences on their properties[90]. As mentioned in Section 1-2, organic ligands are normally used during the synthesis of NCs to passivate their surface. They control the reactivity of different facets in order to adjust the dimensionality of the crystal. However, they do not completely cover the whole surface of the crystal. Since they are relatively long molecules, they cannot get very close to each other. As a result of this periodicity mismatch, some parts of the crystal between the ligands remain un-passivated. This leads to the formation of dangling bonds on the surface. These dangling bonds act as trap states and hinder the transport by reducing the carrier concentration and mobility[38,91-93].

In order to address this problem many ideas have been suggested, including the ligand exchange with shorter molecules or even with single atoms. The more effective alternative would be the hybrid passivation (using more than one type of ligand)[93-95].

Here, Cl^- ions have been employed to hybridly passivate the surface of the nanosheets. The main ligand for the synthesis of these nanosheets is oleic acid, a relatively long organic molecule. In addition to that, different halogenoalkanes have been added to the synthesis. These halogenoalkanes decompose during the synthesis and form halide ions, which act as X-type elemental ligands. These ions penetrate to the organic layer and passivate the dangling

bonds between them. By passivating the trap states, the FET performance of the nanosheets would be improved.

By altering the employed halogen and its amount, it has been shown that Cl^- ions are much more effective than F^- ions. Further, by increasing the amount of the halide ion in the reaction, which is done by increasing the amount of the added halogenoalkane, the passivation could be improved. As a result of this passivation scheme, n-type FETs were obtained with significantly higher conductivities, field-effect mobilities, and on/off ratios. X-ray photoelectron spectroscopy (XPS) measurements have been also used in order to confirm the origin of the improvements[96].

3-3 Device engineering of PbS based FETs

The other important aspect for improving the functionality of the nanosheets is device engineering. The role of the channel thickness and the contact metal have been already investigated[50,52]. Moreover, it has been shown in the previous sections that the performance would be improved by using the stripes instead of the squared sheets or by hybridly passivating the surface traps. To further investigate the system, the influence of the atmospheric gases has been probed. It is expected that introducing air to the nanosheets could alter their transistor properties compared to that in vacuum.

The careful selection of the aforementioned parameters (surface passivator, channel width, contact metal, and working environment) leads to the realization of high performance FETs. For this purpose, a high amount of chloroalkane was used to passivate the surface. This also resulted in the shape transformation from sheets to stripes. Ti was employed as the contact metal to promote the expected n-type behavior by reducing the contact resistance for electrons (since Ti has a low work function). Eventually, the sample was kept in vacuum in order to desorb O_2 from the surface of the crystal, since O_2 acts like a p-dopant. The obtained devices showed an extremely high on/off ratio (4×10^6), field-effect mobility (248 $cm^2V^{-1}s^{-1}$), and conductivity (1916 mS/cm). This level of performance is remarkably higher compared to any other type of colloidal material and is comparable with TMDs and other similar layered materials. Here, the field-effect mobility approaches the electron mobility of bulk PbS. The optimization of the PbS based FETs and the obtained results are schematically summarized in Fig. 23.

A similar strategy could be employed to convert the devices to p-type FETs. If the stripes are contacted with Au (as a high work function metal which promotes p-type behavior) and air is

introduced to their surface (as a p-dopant), they show p-type behavior. Even in the p-type regime, they exhibit high levels of functionality. However, their n-type character is still superior[96].

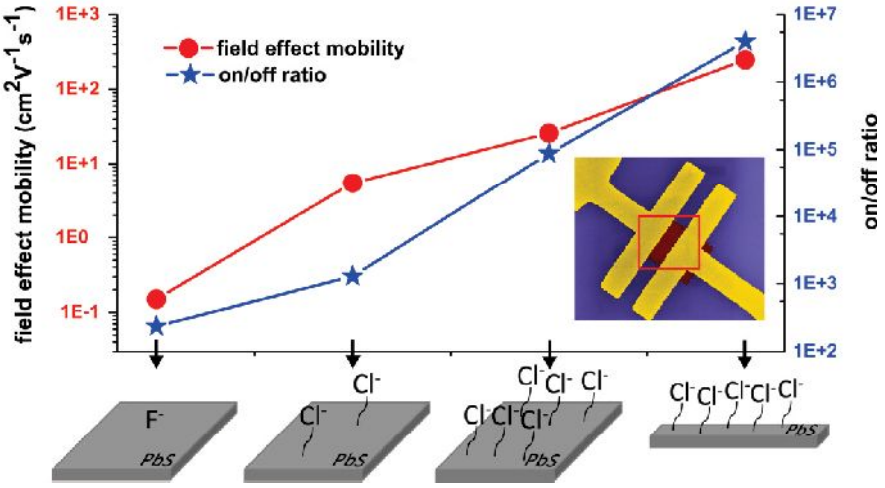

Figure 23. Improvement of the FET behavior (field-effect mobility and on/off ratio) of the PbS nanosheets. While F^- ions are not attached to the surface, Cl^- ions are bound to the surface and improve the properties by passivating the defects. By reducing the width of the highly passivated crystals, high performance FETs could be realized. The figure was adopted from[96].

3-4 Colloidal spintronics through the Rashba effect

The next part of this project was devoted to expand the application of the PbS NCs beyond conventional electronics. Crystals which have heavy elements, such as Pb, show a high spin-orbit coupling. This property plays a significant role in semiconductor spintronics. Thus, these nanosheets might have the potential for spintronic applications. Since the nanosheets are confined in height, the symmetry of their crystal can be easily broken. This would be also the other advantage of the PbS nanosheets for spintronics.

Based on this motivation, the nanosheets were investigated by performing circular photogalvanic measurements in order to probe their spin-orbit coupling. For this purpose, the inversion symmetry of the crystal was broken by applying asymmetric vertical interfaces (vacuum on top and SiO_2 underneath), as well as a vertical gate-electric field (Fig. 24a). This resulted in splitting of the band structure for different spins. In this condition, by exciting spin polarized carriers by circularly polarized light, a photocurrent was generated. The

dependency of the detected current to the angle of the quarter-wave plate was in agreement with the CPGE current. It was maximum when the light polarization was completely circular and was zero when light was linearly polarized. The direction of this photocurrent was reversed by reversing the handedness of the light polarization (Fig. 24b).

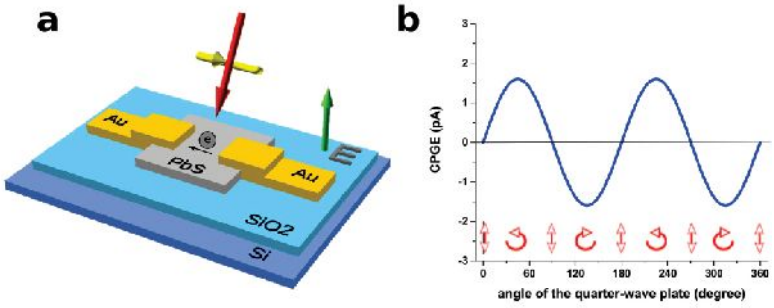

Figure 24. CPGE measurements on the PbS nanosheets. (a) The schematic demonstration of the test setup, required for breaking the symmetry. (b) The oscillation of the CPGE current in different angles of the quarter wave-plate, equivalent with different helicities. The figures were adopted from[97].

In order to ensure that the origin of the observed CPGE is the Rashba band splitting, different methods have been employed. First of all, by partially shadowing the devices and by changing the illumination-incidence angle, it has been shown that the imposed vertical asymmetry (the interfaces and the gate electric field) is indeed effective to generate the CPGE. This is a sign for the Rashba type band splitting.

In addition, density-functional theory (DFT) calculations have been used to simulate the band structure of a PbS nanosheet in the presence of an external electric field. These simulations showed that the valence and conduction bands split at the M point ((110) direction) when a vertical gate electric field is applied to the crystal. By calculating the spin character of the bands, a new selection mechanism for exciting the carriers has been obtained. Based on these observations, the angular momentum of photons couples equally to the M valley (the bandgap at the (110 direction)) and the M' valley. However, it excites only one type of spin. As a result, the generated current is only spin polarized and not valley polarized.

The effect was tuned in different ways. By changing the gate voltage, the degree of broken symmetry was changed and therefore, the band splitting was adjusted. In order to exclude any spin independent effects from the interpretation (for instance altering the contact Schottky barrier by changing the gate electric voltage), the ratio of the spin current (CPGE) to the total

photocurrent was calculated. It was observed that the normalized CPGE has a clear dependency to the gate voltage, as it was expected from the DFT calculations.

Further, by reducing the thickness of the nanosheets, higher degrees of confinement were achieved and the symmetry was broken more effectively. These measurements confirmed that the thinner nanosheets show stronger Rashba effects. Also for these measurements, it was crucial to consider the normalized CPGE, to exclude the irrelevant effects from the interpretations (e.g. the nanosheets' size effect on their light absorption capability).

These experiments were the first realization of the spin transport in colloidal materials. The outcome could combine the idea of spintronics with the advantages of the colloidal synthesis in order to realize low cost high performance computing components. In addition, the observation of the Rashba effect in PbS, which has a centrosymmetric crystal structure, is of great importance, since it helps to better understand different spin-orbit coupled systems[97].

3-5 Tuning the electrical properties of PbS nanowires

The last part of the project which is a complementary section for the previously discussed parts is about tuning the electrical properties of PbS nanowires by sculpting the crystal. As discussed in section 1-2-1, the PbS stripes or sheets are formed through the attachment of small cubes. The surface of these crystals is the {100} facet, which contains Pb and S atoms. By altering the combination of the used ligands, the building blocks (cubes) are transformed to octahedra. The attachment of these octahedra leads to the formation of wire shaped crystals. The surface of these wires is the {111} facet, containing only Pb atoms.

Electrical measurements of these nanowires suggest that they are metallic. They exhibit relatively higher conductivities compared to other forms of PbS, they are not gateable, and they do not show any photo-response. More importantly, by reducing the temperature, their conductivity increases, which is the typical behavior of metals. DFT calculations are also in agreement with the experimental observations and show a non-zero DOS for different energy levels of a PbS crystal, which is cut through the {111} facet. The Pb-rich surface of these wires forms a metallic conduction path around them which makes the whole structure metallic.

It is worthy to point out that these metallic nanowires are synthesized together with normal semiconducting nanowires. By accurately adjusting the synthesis parameters, it is possible to produce both types, or dominantly one of them. The metallic wires can be distinguished from the semiconducting ones by their shape. The former have a zigzag shape while the latter have

a normal straight form. These experiments promote new strategies for tuning the properties of different crystals as well as new applications for lead sulphide nanostructures such as flexible electrodes or interconnects.

3-6 Publications in Peer Reviewed Journals

3-6-1 From Dots to Stripes to Sheets: Shape Control of Lead Sulfide Nanostructures

The following part is the article which summarizes the results of the measurements about reducing the channel width by employing the PbS stripes instead of the squared sheets. My contribution to this project was fabricating the devices based on the PbS stripes, performing the electrical measurements, and the analysis and interpretation of the results. This is a reprint from: *From Dots to Stripes to Sheets: Shape Control of Lead Sulfide Nanostructures,* Thomas Bielewicz, Mohammad Mehdi Ramin Moayed, Vera Lebedeva, Christian Strelow, Angelique Rieckmann, and Christian Klinke. Chemistry of Materials, **2015**. 27(24): p. 8248-8254[53]. Copyright ©2015 American Chemical Society.

CHEMISTRY OF MATERIALS

Article

pubs.acs.org/cm

From Dots to Stripes to Sheets: Shape Control of Lead Sulfide Nanostructures

Thomas Bielewicz, Mohammad Mehdi Ramin Moayed, Vera Lebedeva, Christian Strelow, Angelique Rieckmann, and Christian Klinke*

Institute of Physical Chemistry, University of Hamburg, Grindelallee 117, 20146 Hamburg, Germany

Supporting Information

ABSTRACT: Controlling anisotropy in nanostructures is a challenging but rewarding task because confinement in one or more dimensions influences the physical and chemical properties of the items decisively. In particular, semiconducting nanostructures can be tailored to gain optimized properties to work as transistors or absorber material in solar cells. We demonstrate that the shape of colloidal lead sulfide nanostructures can be tuned from spheres to stripes to sheets by means of the precursor concentrations, the concentration of a chloroalkane coligand and the synthesis temperature. All final structures still possess at least one dimension in confinement. The structures cover all dimensionalities from 0D to 3D. Additionally, the effect of temperature on the shape and thickness of PbS nanosheets is shown and electrical transport measurements complement the findings.

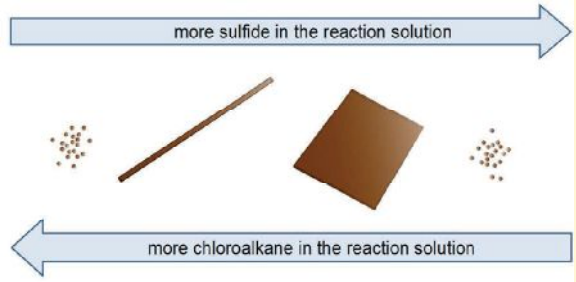

INTRODUCTION

By influencing the shape and size of nanocrystals, it is possible to also influence their chemical and physical properties.[1−3] These depend strongly on the structures' dimensionality. The optical and electrical properties of a 0D material (e.g., quantum dots) differ strongly from the ones of a 1D nanomaterial (e.g., nanowires). Although the first possess discrete energy levels,[4] the latter possess so-called van-Hove singularities in the density of states.[5] Nowadays, two-dimensional materials (2D) also gain attention because of their good conductivity in the plane while still being tunable in their electronic properties because of confinement in height.[6−13] Colloidal chemistry represents a promising route to synthesize semiconductor nanomaterials which are inexpensive and easily processable as thin films for electronic devices.[14−21] This method allows for shape control by changing, for example, the synthesis temperature or ligand concentration.[22−25]

To obtain anisotropic nanostructures, crystal growth must be prevented in certain directions, which is well achievable in PbS,[26,27] despite PbS having a cubic symmetry. To alter the growth of PbS to obtain different kinds of anisotropic structures, pressure and temperature can be enough to transform already grown PbS nanowires to two-dimensional structures.[28] Another convenient way is to introduce a chloroalkane to a colloidal nanoparticle synthesis, which can yield a lot of different structures depending on other parameters in the synthesis.[29−31] By confinement in height, producing two-dimensional sheetlike structures, the effective band gap can be tuned from the bulk value of 0.41 eV[32] up to values of over 1 eV, whereas charge carriers can still move freely in the sheets' plane. The rather large Bohr exciton radius of PbS of about 18 nm[33] also helps to shift the absorption wavelength from the bulk value of ∼3000 nm to the visible range.[34] This makes PbS an interesting semiconductor material for applications in infrared photodetectors[35] and solar cells.[36,37] Moreover, its capability for carrier multiplication attracted considerable attention.[38,39]

In our first findings on two-dimensional PbS via colloidal synthesis,[40] the addition of a chloride compound was crucial because it influenced the kinetics of nucleation and growth in such a way that ultrasmall PbS particles (<3 nm) merged into larger sheets by oriented attachment. The driving force of this attachment is the reduction of the area of highly reactive {110} facets of the ultrasmall particles. At the same time a vertical growth is prohibited by a self-assembly of oleic acid on the {100} facets of the crystals. Later, we showed that through a variation of the oleic acid concentration the sheets could be controlled in their thickness and sheets with heights ranging from 4 up to 20 nm could be synthesized.[18] At the same time, the group of Sun et al. showed that using different chloroalkanes at different temperatures the thickness could also be controlled from 2 up to 4.6 nm.[41] Here, we show that the thickness of the sheets is only dependent on the reaction temperature regardless which chloroalkane is used. We also show how the shape of PbS nanostructures can be controlled by changing the molar ratio between the lead precursor and the

Received: August 4, 2015
Revised: December 1, 2015
Published: December 9, 2015

ACS Publications © 2015 American Chemical Society

DOI: 10.1021/acs.chemmater.5b03088
Chem. Mater. 2015, 27, 8248−8254

sulfur source, but also by changing the concentration of the essential chloroalkane coligand. The latter allows tuning the shape from spherical nanoparticles to stripes and to sheets. It is astonishing that small changes can lead to a variety of new PbS structures, in particular elongated PbS stripes with a length of several tens of micrometers. Nanostripes can be used in further studies because of their ease of processing. We show that they possess even better electronic properties compared to what we found previously for PbS sheets.[42]

In syntheses of colloidal chalcogenide nanomaterials the molar ratio between the precursors usually varies between 1:5 to 5:1.[43] In our first reported synthesis of ultrathin lead sulfide nanosheets the ratio between the lead and sulfur source was already at an unusual high molar ratio of 14:1.[40] Basis for the synthesis is a standard procedure for spherical nanoparticles, which was then complemented with 1,1,2-trichloroalkane (TCE) to produce nanosheets. Both approaches contain tri-n-octyl phosphine (TOP) as a coligand. Recently, we found that increasing the molar ratio between lead and sulfur to 120:1 makes it possible to obtain nanosheets without any TOP in the reaction solution (with spherical nanoparticles as byproduct).[18] In studies presented here, we demonstrate that under appropriate conditions TOP is no longer necessary to produce large, thin and smooth nanosheets or nanostripes of lead sulfide. By increasing the molar ratio even beyond 120:1 (Pb:S) less ligands are needed to control the shape which could be also interesting for other colloidal syntheses where higher ratios could also lead to new shapes.

RESULTS AND DISCUSSION

Sulfide Concentration. Chloroalkanes function as weak ligands and support the formation of two-dimensional nanosheets by oriented attachment. In a previous publication, we could show that chloroalkanes possess the highest binding energy on {110} facets of the PbS crystal where lead and sulfur ions are aligned in rows.[18] These facets are also the ones on which oriented attachment takes place. Due to the adsorption of the chloroalkanes and displacement of oleic acid (OA) on these facets, they become richer in energy. Because the binding of the chloroalkanes is weaker to those facets than that of oleic acid or oleate, oriented attachment takes place to minimize the surface energy of these crystal facets.

In a first series of experiments the sulfide concentration was varied while fixing all other parameters. Using three different chloroalkanes as coligands, namely 1,1,2-trichloroethane (1,1,2-TCE), 2,3-dichlorobutane (2,3-DCB), and 1,3-dichlorobutane (1,3-DCB), shows that with decreasing sulfide concentration the structures' shape changes. Despite their structural differences (but similar boiling points), all three chloroalkanes yield comparable shapes at the same Pb:S molar ratios: from two-dimensional nanosheets (Pb:S ratio starting from 35:1) to long stripelike structures and finally to monodisperse spherical nanoparticles (Pb:S ratio of 550:1) as shown in Figure 1. Not shown are high sulfide concentrations (Pb:S ratio >35:1) where spherical nanoparticles are formed, too. It seems that only the functional group plays a major role. With a very low sulfide concentration (molar Pb:S ratio more than 500:1) only few nuclei are formed at the start of the reaction. These nuclei cannot find other nuclei easily to merge to nanosheets via oriented attachment but eventually stripes can still form through oriented attachment. By increasing the concentration (at molar Pb:S ratios between 300:1 and 500:1) enough nuclei are formed and oriented attachment takes place to yield sheet-like two-dimensional structures. When the sulfide concentration is increased, these stripes can grow together to form square-like sheets (molar ratios below 300:1) because there is still enough sulfide monomer present in the reaction solution. Otherwise, the stripes are stabilized too strongly by the ligands. Kiran et al. identified a $(PbS)_{32}$ cluster as the first stable crystal and could show by atomic force microscopy (AFM) measurements that the first larger and detectable structures are built from these clusters.[44] It is interesting, that four of those clusters do not always merge to squarelike structures but can also form stripelike structures where all four clusters merge via the same facet type. With a smaller sulfide concentration and when ligands are present in the reaction solution, the stripelike structures seem to be the preferred shape of lead sulfide nanocrystals. This holds true for all considered chloroalkanes coligands, with just a slight variation of when which shape is obtained. In Figure 2, HRTEM and SAED of a stripe show that they are single crystals and the borders of the crystal consists of {110} planes, which confirms that stripes also grow in the same manner as PbS nanosheets.[40]

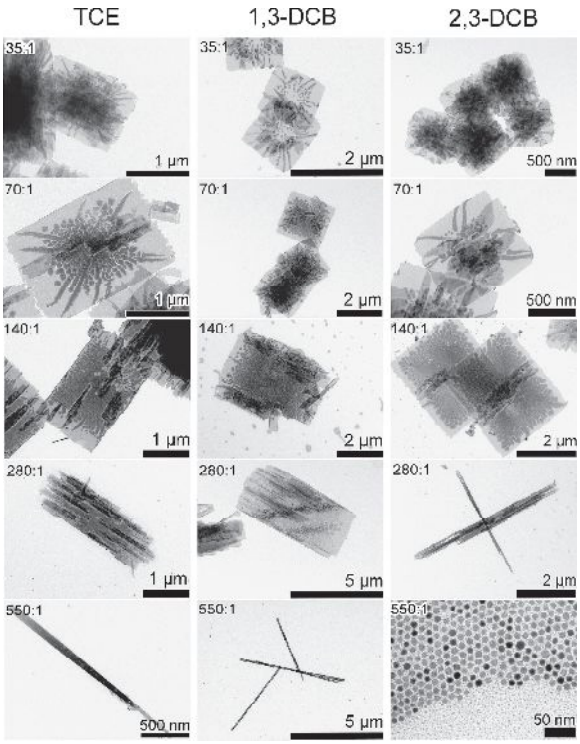

Figure 1. PbS nanoparticle shape evolution as a function of sulfur source concentration. Three different chloroalkanes were used at the same reaction temperature of 135 °C. The numbers in the images correspond to the molar ratio of Pb:S. A shape evolution can be seen with all chloroalkanes. The results are basically the same for the different chloroalkanes. Only 2,3-DCB leads to stripes earlier than the other two, but the shape is comparable with the others. The amount of each chloroalkane used was 0.3 mL.

Chloroalkane Concentration. The chloroalkanes function as coligands on the various crystal facets. It seems that they are mandatory for the PbS nanosheet synthesis. The sulfide concentration study showed that all three chloroalkanes yield very similar products. Thus, we take one of those chloroalkanes (2,3-DCB) and a structurally very different one, 1-chlorote-

DOI: 10.1021/acs.chemmater.5b03088
Chem. Mater. 2015, 27, 8248−8254

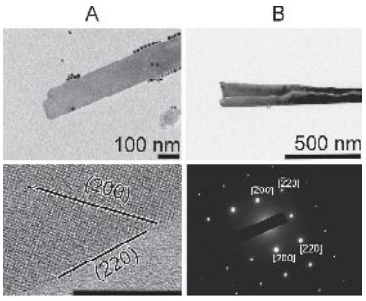

Figure 2. HRTEM and SAED of PbS stripes. (A) HRTEM images show a PbS stripe synthesized at 135 °C with a molar ratio of 550:1 and 0.3 mL of TCE as coligand shown on top. The bottom image of A shows the crystal structure of the same stripe (the scale bar corresponds to a length of 10 nm.) The calculated *d*-spacing measured in the image (d = 0.3 nm) is in good agreement with the (200) spacing from literature which is 0.2969 nm (JCPDS 5−592: galena PbS). To confirm that the planar surface of the structure is the (001) plane a SAED pattern of a stripe was performed which can be seen in B. By dividing the distances from the transmitting beam in the middle in the [220] direction by the distance from the middle in the [200] direction a value of 1.406 was calculated which is in very good agreement with the theoretical value of a face centered cubic (fcc) crystal of 1.414.[45]

tradecane (1-CTD), to perform experiments varying the concentration of the chloroalkanes (Figure 3). While with smaller amounts of chloroalkane sheet-like structures are formed, larger amounts lead to stripelike structures and eventually to spherical nanoparticles. Omitting the chloroalkanes leads to mostly spherical nanoparticles. Thus, the chloroalkanes play a decisive role in the shape formation of the product. It is remarkable that even long-chained chloroalkanes such as 1-CTD behave the same way as the other short ones at the same reaction temperature of 135 °C.

With 1-CTD, it is also possible to conduct a reaction with 1-CTD as sole solvent, omitting the original solvent diphenyl ether (DPE) completely. This reaction yielded spherical nanoparticles only. This supports our understanding that chloroalkanes function as a stabilizing agent for nanocrystals and such very high chloroalkane concentrations (in this case, nearly four times the oleic acid molar amount) coordinate the crystals efficiently so that no oriented attachment can take place.

One could argue that the shape evolution is just a matter of reaction volume and not the chloroalkane concentration. To make sure the chloroalkanes play a role in the lead sulfide nanoparticle formation, we have performed two reactions without the chloroalkanes but with 0.2 and 2 mL of diphenyl ether instead, which has been injected at the same time as the chloroalkanes would have been. The outcome of these experiments shows that no two-dimensional nanosheets are formed when the chlorine source is not present (Figure S1).

It is worth pointing out that PbS sheets and stripes, obtained by the aforementioned methods, manifest comparable semiconducting behaviors. We fabricated field-effect transistors (FETs) using individual PbS stripes, in order to compare their electrical properties with the formerly investigated sheets.[42] As depicted in Figure 4, application of a back-gate voltage can modulate the electrical conductivity of the channel significantly. The measurements reveal that the stripes in contact with Au electrodes show p-type behavior, indicated by a decrease of the current with increasing gate voltage. This means that the holes

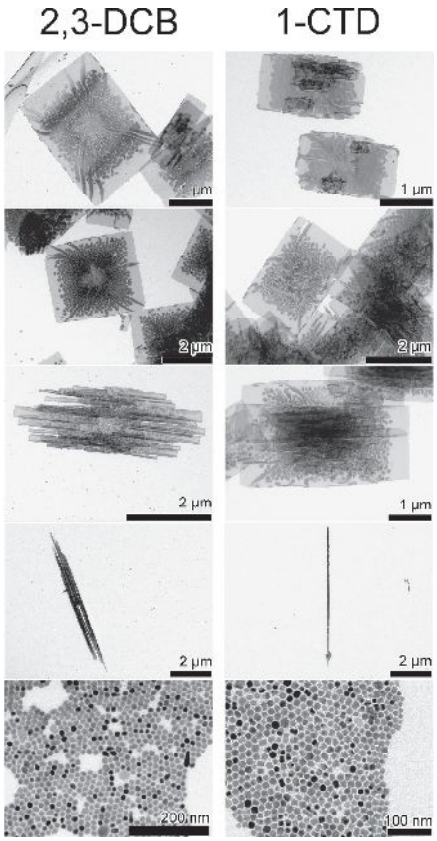

Figure 3. PbS nanoparticle shape evolution as a function of chloroalkane concentration. On the left the chloroalkane 2,3-DCB was used to change the shape. The volume from top to bottom is 0.15, 0.3, 0.6, 0.9, and 1.25 mL, respectively. The molar ratio between Pb:S was fixed to 120:1 and the reaction temperature was 135 °C. Here, the shape of the sheets evolves from sheets to stripes to spherical nanoparticles. On the right PbS nanosheet reaction with changing 1-CTD volume at a synthesis temperature of 135 °C and a Pb:S ratio of 120:1. From top to bottom the volume is 0.4, 0.8, 1.6, 4, and 10 mL. The shape of the PbS nanoparticles changes from spherical nanoparticles to stripes and finally to sheets.

are the majority charge carriers in the device. A similar behavior was also observed in quantum dot FETs.[43] This similarity in type of the majority carriers is originated from the analogy in their structural properties (crystal structure, thickness, etc.). Therefore, the bandgaps of both PbS shapes, sheets and stripes, are equally affected by quantum confinement.[42,18,19] Moreover, using stripes with the same thickness as squared nanosheets as the active material improves the switching behavior. The on/off ratio for such devices can reach to over 3400 at room temperature, while the maximum field-effect mobility of the carriers is calculated to be up to 5.59 $cm^2 V^{-1} s^{-1}$. The lateral confinement of the active channel may affect the performance of the FETs. In particular it reduces the current flowing in the "off" state, leading to higher on/off ratios and field-effect mobility.

Effect of Temperature. Bhandari et al. recently reported on the synthesis of PbS nanosheets. They were able to tune the thickness of the nanosheets by using different chloroalkanes at different temperatures.[41] We believe that the thickness is a

DOI: 10.1021/acs.chemmater.5b03088
Chem. Mater. 2015, 27, 8248−8254

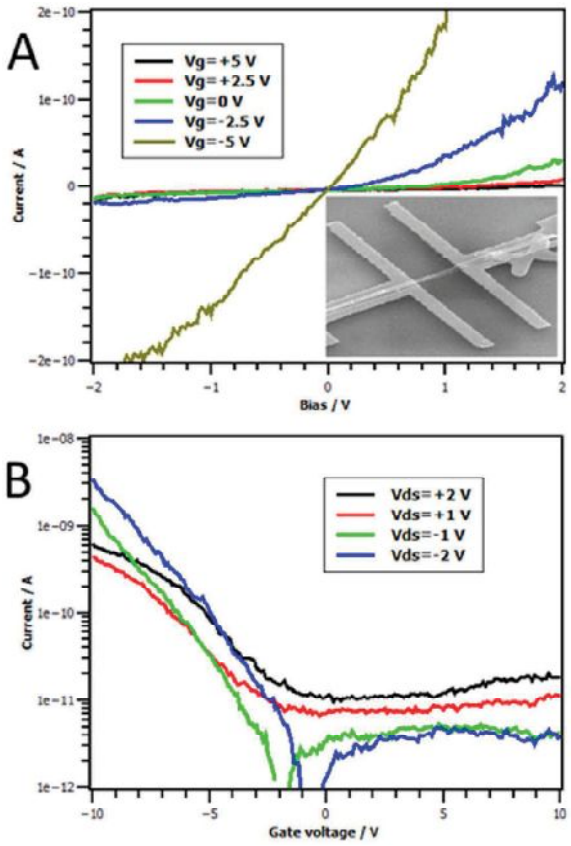

Figure 4. Electrical transport measurements on individual PbS stripes. (A) Room-temperature output characteristics of the field effect transistors using a PbS stripe as channel. The inset is the SEM image of the FET with an individual PbS stripe contacted with Au electrodes. (B) Transfer characteristics of the same PbS nanostripe FET. A switching effect and a p-type behavior are observed. This implies that holes are the majority carriers in these devices. The strong current changes at negative gate voltages can be understood as high field effect mobility of the carriers (holes).

matter of the temperature only and is largely independent of the nature of the chloroalkanes. To further study this question, we chose a Pb:S ratio of 120:1 since this yielded the smoothest and largest nanosheets up to now. The syntheses were performed at 100, 120, 160, and 200 °C, respectively. The chloroalkane used for all the different temperatures has to be the same to show that only the temperature has the major effect on the thickness of the sheets. We used TCE and 1-CTD in the temperature study because their structure and thus, their chemical and physical properties are most different but the results from both chloroalkanes are basically the same, as we will show.

The first apparent difference in the reaction is the time the reaction solution took to turn black after the injection of the sulfur source, as a sign for PbS formation. While at 100 °C it takes about 4 min for the reaction solution to turn completely black, the time shortens to around 3 min at 120 °C and only 20 s at 160 °C. At 200 °C the solution turns black instantly after injection of the sulfur source.

The received products at the different temperatures vary significantly in shape. At 100 °C the sheets are very thin while being close to 1 μm in lateral dimensions (Figure 5). AFM measurements show the thickness to be around 5 nm including the ligand sphere. With only 20 °C more the nanosheets are larger in their lateral dimensions, but also in height. This is observable by the more pronounced vertical growth over a larger area of the sheets compared to a reaction temperature of 100 °C. In our previous findings where we varied the height of the sheets by changing the oleic acid concentration, the "second layer" did not grow to the borders of the nanosheets, even with the thickest sheets.[18] There, all reactions were performed at the same reaction temperature of 130 °C.

AFM shows that the thickness of the nanosheets synthesized at 160 °C is higher than the ones obtained at lower reaction temperatures. The surface of these nanosheets is also smoother as the vertical growth happened uniformly on the whole sheet (a calculated root-mean-square value over 3500 thickness data points on the nanosheet results in 0.1 nm). The lateral dimensions increased again while at the same time also more spherical nanoparticles were produced in parallel. At elevated temperatures the reactivity and decomposition of TAA was increased in such a way, that there is a quite high sulfide monomer concentration. Spherical particle growth also takes place from the beginning on while at the same time the lead oleate complex bonds are weakened, which should also favor a spherical particle growth as the lead complex is more reactive. The amount of nanoparticles can be reduced postsynthetically by washing the product more often with toluene until the supernatant becomes clear in color. This procedure has no visible negative influence on the nanosheets, as there could be increased stacking or breaking apart.

At 200 °C, the sheets become more squarelike and there are less spherical nanoparticles in the product than at 160 °C. TAA decomposes faster at this temperature so there are more nuclei formed and less sulfide monomer is available in the growth phase—both favoring the kinetic product only. The product exhibits holes in the structures. Some structures are even more degenerated and do not resemble a sheet anymore. Besides the large almost quadratic holes, the borders are much rounder than the ones of the nanosheets received at 160 °C. The borders also show stronger contrast in the TEM images compared to the center of the nanosheets. AFM measurements prove that the border is the thickest part of the structures while there is not much change in thickness over the whole cross-section of nanosheets synthesized at 160 °C in comparison.

The holes and rounded borders could be due to a decomposition process of the nanosheets. The decomposition could be induced by acetate/oleic acid, as acids can etch lead sulfide nanoparticles.[46] We remove the acetate as acetic acid during the degassing step of the reaction. Anyhow, when the sulfide source TAA decomposes it forms acetate, which could initiate the etching. The two-dimensional structures would probably start to decompose especially at their thinnest spots and already existing small holes. We observed such holes in sheets only at temperatures higher than 160 °C. By decreasing the TAA amount the decomposition at higher temperatures can be prevented which is shown in Figure S2, where a 550:1 Pb:S ratio was chosen and the sheets show no holes at a reaction temperature of 200 °C anymore.

To track possible loss or decomposition of TCE, we performed NMR (Figure S3). Despite TCE's boiling point of 113 °C all proton signals from TCE could be detected and their integrals are in good agreement with the molecular structure of TCE. At the same time, no new signals were observed, which

DOI: 10.1021/acs.chemmater.5b03088
Chem. Mater. 2015, 27, 8248−8254

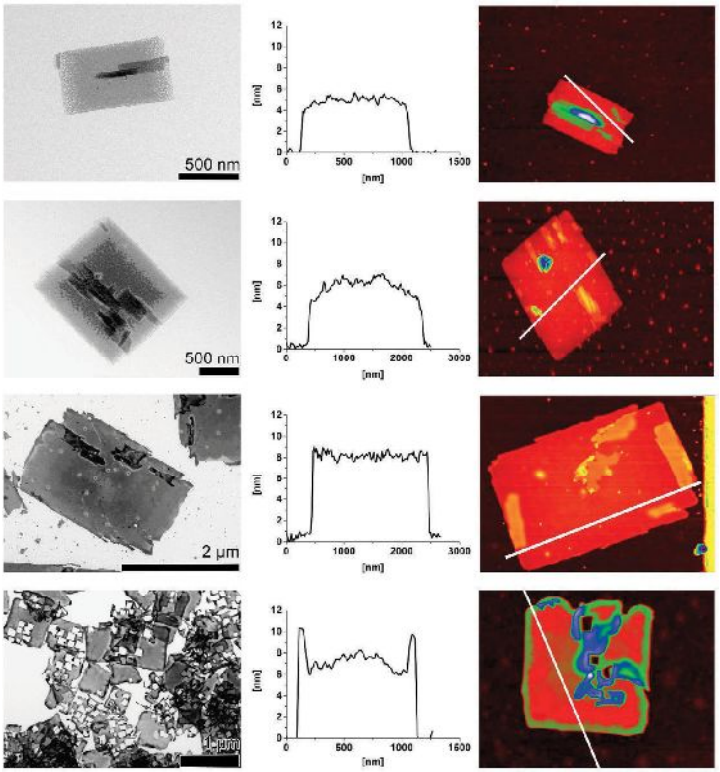

Figure 5. Shape and thickness evolution with temperature. All parameters are constant and only the temperature was varied. Shown are the TEM pictures of the reaction product with TCE (0.7 mL) as coligand. The temperature increases from top to bottom from 100 to 120 to 160 and finally to 200 °C. Sheets at 200 °C show a holey structure and become smaller in lateral dimensions. AFM clearly shows an increase in thickness with higher temperature while at 200 °C the borders become the thickest part of the sheet. For 1-CTD TEM images see Figure S4 (100 and 200 °C) and Figure 3 (135 °C).

implies that TCE is still present in the reaction solution well above its boiling point.

The PbS nanostructures are stabilized by a self-assembled monolayer of oleate with a height of 1.8 nm.[47] Considering the thinnest nanosheets synthesized at 100 °C, subtracting twice the height of the ligands (for top and bottom) leads to a height of the inorganic core part of about 2.4 nm which corresponds to only 4 times the lattice constant. We calculated the mean sheet thicknesses obtained at the different reaction temperatures (Figure S5) by fitting the (200) XRD peak and using Scherrer's equation with a form factor of 1.[48] The results for both, TCE and 1-CTD, are shown in Figure 6. A dependence of the sheet thickness with the reaction temperature is apparent, whereas the type of chloroalkane plays a minor role.

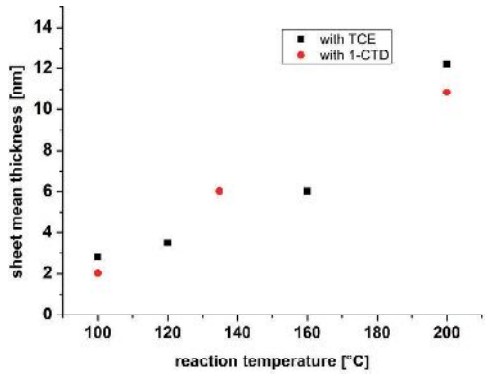

Figure 6. Thickness of PbS sheets as a function of the reaction temperature. The black rectangles represent the results with TCE as coligand while the red circles represent the ones with 1-CTD. The thickness was calculated using the Scherrer's equation[48] by fitting the (200) XRD peak of the lead sulfide sheets. Despite their different structure both chloroalkanes produce nanosheets with comparable thickness at similar reaction temperatures (Figure 5 and Figure S4). With elevated temperature the sheets become thicker.

CONCLUSION

By varying the concentration of the sulfur source in the PbS synthesis, it was possible to change the shape of the product. Depending on the chosen concentrations formed nuclei at the beginning of the reaction can change to spherical nanoparticles, elongated stripes or large sheets. Starting from high molar ratios between lead and sulfur (550:1) a reaction at 135 °C takes place and yields elongated stripelike structures. Through HRTEM, we could show that the borders of the stripes are {110} planes and the growth occurs via oriented attachment. By reducing the molar ratio, more squarelike sheets are formed with all chloroalkanes used in this study.

By changing the chloroalkane amount, the same transition between spherical nanoparticles to stripes and sheets takes place. Changing the chloroalkane amount has the same effect on the shape of the PbS sheets as changing the sulfur amount.

DOI: 10.1021/acs.chemmater.5b03088
Chem. Mater. 2015, 27, 8248−8254

This behavior is the same for all chloroalkanes used in this study independent of the molecules' structure, making reaction temperature and the concentrations of the chloroalkane the crucial parameters for shape change of the PbS structures. Thus, less toxic and cheaper chlorine compounds can be used to fabricate 2D PbS nanosheets.

By changing the reaction temperature, we could drive the synthesis to obtain larger nanosheets with a flat and smooth surface over several microns, whereas at the same time, the thickness also increases with temperature from around 2 nm at 100 °C to 10 nm at 200 °C. The thinnest sheets could be good candidates for PbS solar cells.[14] In principle, the synthesis is scalable, but a protocol for the recycling of lead oleate should be developed due to the high precursor concentration.

METHODS

Synthesis. Lead(II) acetate trihydrate (Aldrich, 99.999%), thioacetamide (Sigma-Aldrich, ≥ 99.0%), diphenyl ether (Aldrich, 99%+), dimethylformamide (Sigma-Aldrich, 99.8% anhydrous), oleic acid (Aldrich, 90%), 1,1,2-trichloroethane (Aldrich, 96%), 1,3-dichlorobutane (Aldrich, 99%), 1-chlorotetradecane (Aldrich, 98%), and 2,3-dichlorobutane (Acros, 98%) were all used as received.

In a typical synthesis, a three neck 50 mL flask was used with a condenser, septum and thermocouple. 860 mg of lead acetate trihydrate (2.3 mmol) were dissolved in 10 mL of diphenyl ether and 3.5 mL of oleic acid (OA, 10 mmol) and heated to 75 °C until the solution turned clear. Then vacuum was applied to transform the lead acetate into lead oleate and to remove the acetic acid in the same step. The solution was heated under nitrogen flow to the desired reaction temperature between 100 and 200 °C), whereas at 100 °C the chloroalkane (volume depending on the desired shape) was added under reflux to the solution. After 12 min, 0.05−2 mL of a 0.04 g thioacetamide (TAA, 0.5 mmol) in 6.5 mL of dimethylformamide (DMF) solution was added to the reaction solution. After 5 min, the heat source was removed and the solution was left to cool down below 60 °C which took approximately 15−30 min depending on the reaction temperature. Afterward, it was centrifuged at 4000 rpm for 3 min. The precipitant was washed two times in toluene before the product was finally suspended in toluene again for storage.

TEM. The TEM samples were prepared by diluting the nanosheet suspension with toluene and then drop casting 10 μL of the suspension on a TEM copper grid coated with a carbon film. Standard images were done on a JEOL-1011 with a thermal emitter operated at an acceleration voltage of 100 kV. HRTEM images were done on a JEOL JEM 2200FS (UHR) equipped with a field emitter, CESCOR and CETCOR correctors at an acceleration voltage of 200 kV.

XRD. X-ray diffraction measurements were performed on a Philips X'Pert System with a Bragg−Brentano geometry and a copper anode with a X-ray wavelength of 0.154 nm. The samples were measured by drop-casting the suspended nanosheets on a ⟨911⟩ or ⟨711⟩ grown silicon substrate.

AFM. Atomic force microscopy measurements were performed in tapping mode on a Veeco MultiMode NanoScope 3A and a JPK Nano Wizard 3 AFM in contact mode. The samples were prepared by spin-coating the nanosheet suspension on a silicon wafer.

Device Preparations and Characterization. PbS nanostripes with a length of serveral micrometers, a width of about 100 nm, and a height of about 15 nm suspended in toluene were spin-coated on silicon wafers with 300 nm thermal silicon oxide as gate dielectric. The highly doped silicon was used as backgate. The individual nanosheets were contacted by e-beam lithography followed by thermal evaporation of gold and lift-off. Immediately after device fabrication the devices were transferred to a probe station (Lakeshore-Desert) connected to a semiconductor parameter analyzer (Agilent B1500a). The transfer and output characteristics have been performed in vacuum at room temperature.

ASSOCIATED CONTENT

Supporting Information

The Supporting Information is available free of charge on the ACS Publications website at DOI: 10.1021/acs.chemmater.5b03088.

Additional TEM images showing the products of the syntheses, NMR spectra of the ligands, and XRD patterns of the nanosheets at different synthesis temperatures (PDF)

AUTHOR INFORMATION

Corresponding Author

*E-mail: klinke@chemie.uni-hamburg.de.

Notes

The authors declare no competing financial interest.

ACKNOWLEDGMENTS

The authors thank the German Research Foundation DFG for financial support in the frame of the Cluster of Excellence "Center of ultrafast imaging CUI" and for granting the project KL 1453/9-1. The European Research Council is acknowledged for funding an ERC Starting Grant (Project: 2D-SYNETRA (304980), Seventh Framework Program FP7).

REFERENCES

(1) Peng, X. G.; Manna, L.; Yang, W. D.; Wickham, J.; Scher, E.; Kadavanich, A.; Alivisatos, A. P. Shape Control of CdSe Nanocrystals. *Nature* **2000**, *404*, 59−61.

(2) Murray, C. B.; Norris, D. J.; Bawendi, M. G. Synthesis and Characterization of Nearly Monodisperse CdE (E = Sulfur, Selenium, Tellurium) Semiconductor Nanocrystallites. *J. Am. Chem. Soc.* **1993**, *115*, 8706−8715.

(3) Milliron, D. J.; Hughes, S. M.; Cui, Y.; Manna, L.; Li, J.; Wang, L.-W.; Alivisatos, A. P. Colloidal Nanocrystal Heterostructures with Linear and Branched Topology. *Nature* **2004**, *430*, 190−195.

(4) Klimov, V. I. Mechanisms for Photogeneration and Recombination of Multiexcitons in Semiconductor Nanocrystals: Implications for Lasing and Solar Energy Conversion. *J. Phys. Chem. B* **2006**, *110*, 16827−16845.

(5) Charlier, J. C.; Blasé, X.; Roche, S. Electronic and Transport Properties of Nanotubes. *Rev. Mod. Phys.* **2007**, *79*, 677−733.

(6) Novoselov, K. S.; Geim, A. K.; Morozov, S. V.; Jiang, D.; Zhang, Y.; Dubonos, S. V.; Grigorieva, I. V.; Firsov, A. A. Electric Field Effect in Atomically Thin Carbon Films. *Science* **2004**, *306*, 666−669.

(7) Geim, A. K.; Novoselov, K. S. The Rise of Graphene. *Nat. Mater.* **2007**, *6*, 183−191.

(8) Nicolosi, V.; Chhowalla, M.; Kanatzidis, M. G.; Strano, M. S.; Coleman, J. N. Liquid Exfoliation of Layered Materials. *Science* **2013**, *340*, 1226419.

(9) Mas-Ballesté, R.; Gómez-Navarro, C.; Gómez-Herrero, J.; Zamora, F. 2D materials: to graphene and beyond. *Nanoscale* **2011**, *3*, 20−30.

(10) Zhao, W.; Ghorannevis, Z.; Chu, L.; Toh, M.; Kloc, C.; Tan, P.-H.; Eda, G. Evolution of Electronic Structure in Atomically Thin Sheets of WS2 and WSe2. *ACS Nano* **2013**, *7*, 791−797.

(11) Yin, Z.; Li, H.; Li, H.; Jiang, L.; Shi, Y.; Sun, Y.; Lu, G.; Zhang, Q.; Chen, X.; Zhang, H. Single-layer MoS2 Phototransistors. *ACS Nano* **2012**, *6*, 74−80.

(12) Bouet, C.; Mahler, B.; Nadal, B.; Abecassis, B.; Tessier, M. D.; Ithurria, S.; Xu, X.; Dubertret, B. Two-Dimensional Growth of CdSe Nanocrystals, from Nanoplatelets to Nanosheets. *Chem. Mater.* **2013**, *25*, 639−645.

(13) Vaughn, D. D., II; In, S.-I.; Schaak, R. E. A Precursor-Limited Nanoparticle Coalescence Pathway for Tuning the Thickness of

Laterally-Uniform Colloidal Nanosheets: The Case of SnSe. *ACS Nano* **2011**, *5*, 8852−8860.
(14) Kramer, I. J.; Sargent, E. H. The Architecture of Colloidal Quantum Dot Solar Cells: Materials to Devices. *Chem. Rev.* **2014**, *114*, 863−882.
(15) Mcdonald, S. A.; Konstantatos, G.; Zhang, S.; Cyr, P. W.; Klem, J. D. E.; Levina, L.; Edward, H.; Sargent, E. H. Solution-processed PbS Quantum Dot Infrared Photodetectors and Photovoltaics. *Nat. Mater.* **2005**, *4*, 138−142.
(16) Khan, A. H.; Thupakula, U.; Dalui, A.; Maji, S.; Debangshi, A.; Acharya, S. Evolution of Long Range Bandgap Tunable Lead Sulfide Nanocrystals with Photovoltaic Properties. *J. Phys. Chem. C* **2013**, *117*, 7934−7939.
(17) Piliego, C.; Protesescu, L.; Bisri, S. Z.; Kovalenko, M. V.; Loi, M. A. 5.2% Efficient PbS Nanocrystal Schottky Solar Cells. *Energy Environ. Sci.* **2013**, *6*, 3054−3059. (e) Luther, J. M.; Law, M.; Beard, M. C.; Song, Q.; Reese, M. O.; Ellingson, R. J.; Nozik, A. Schottky Solar Cells Based on Colloidal Nanocrystal Films. J. *Nano Lett.* **2008**, *8*, 3488−3492.
(18) Bielewicz, T.; Dogan, S.; Klinke, C. Tailoring the Height of Ultrathin PbS Nanosheets and Their Application as Field-Effect Transistors. *Small* **2015**, *11*, 826−833.
(19) Dogan, S.; Bielewicz, T.; Lebedeva, V.; Klinke, C. Photovoltaic effect in individual asymmetrically contacted lead sulfide nanosheets. *Nanoscale* **2015**, *7*, 4875−4883.
(20) Talapin, D. V.; Murray, C. B. PbSe Nanocrystal Solids for n- and p-Channel Thin Film Field-Effect Transistors. *Science* **2005**, *310*, 86−89.
(21) Claridge, S. A.; Castleman, A. W.; Khanna, S. N.; Murray, C. B.; Sen, A.; Weiss, P. S. Cluster-assembled Materials. *ACS Nano* **2009**, *3*, 244−255.
(22) Wang, Y.; Yang, X.; Xiao, G.; Zhou, B.; Liu, B.; Zou, G.; Zou, B. Shape-controlled Synthesis of PbS Nanostructures from 20 to 240 °C: the Competitive Process between Growth Kinetics and Thermodynamics. *CrystEngComm* **2013**, *15*, 5496−5505.
(23) Warner, J. H.; Cao, H. Shape Control of PbS Nanocrystals Using Multiple Surfactants. *Nanotechnology* **2008**, *19*, 305605−1−305605−5.
(24) (a) Khan, A. H.; Thupakula, U.; Dalui, A.; Maji, S.; Debangshi, A.; Acharya, S. Evolution of Long Range Bandgap Tunable Lead Sulfide Nanocrystals with Photovoltaic Properties. *J. Phys. Chem. C* **2013**, *117*, 7934−7939.
(25) Rogach, A. L.; Eychmüller, A.; Hickey, S. G.; Kershaw, S. V. Infrared-emitting Colloidal Nanocrystals: Synthesis, Assembly, Spectroscopy, and Applications. *Small* **2007**, *3*, 536−557.
(26) (a) Lee, S.-M.; Jun, Y.-W.; Cho, S.-N.; Cheon, J. Single-Crystalline Star-Shaped Nanocrystals and Their Evolution: Programming the Geometry of Nano-Building Blocks. *J. Am. Chem. Soc.* **2002**, *124*, 11244−11245.
(27) Evers, W. H.; Goris, B.; Bals, S.; Casavola, M.; de Graaf, J.; van Roij, R.; Dijkstra, M.; Vanmaekelbergh, D. Low-Dimensional Semiconductor Superlattices Formed by Geometric Control over Nanocrystal Attachment. *Nano Lett.* **2013**, *13*, 2317−2323.
(28) Acharya, S.; Das, B.; Thupakula, U.; Ariga, K.; Sarma, D. D.; Israelachvili, J.; Golan, Y. A Bottom-up Approach Toward Fabrication of Ultrathin PbS Sheets. *Nano Lett.* **2013**, *13*, 409−415.
(29) Wang, Z.; Schliehe, C.; Bian, K.; Dale, D.; Bassett, W. A.; Hanrath, T.; Klinke, C.; Weller, H. Correlating Superlattice Polymorphs to Internanoparticle Distance, Packing Density, and Surface Lattice in Assemblies of PbS Nanoparticles. *Nano Lett.* **2013**, *13*, 1303−1311.
(30) Gerdes, F.; Volkmann, M.; Schliehe, C.; Bielewicz, T.; Klinke, C. Sculpting of Lead Sulfide Nanoparticles by Means of Acetic Acid and Dichloroethane. *Z. Phys. Chem.* **2015**, *229*, 139−151.
(31) Nagel, M.; Hickey, G. S.; Frömsdorf, A.; Kornowski, A.; Weller, H. Synthesis of Monodisperse PbS Nanoparticles and Their Assembly into Highly Ordered 3D Colloidal Crystals. *Z. Phys. Chem.* **2007**, *221*, 427−437.
(32) Zhou, Y.; Itoh, H.; Uemura, T.; Naka, K.; Chujo, Y. Preparation, Optical Spectroscopy, and Electrochemical Studies of Novel π-Conjugated Polymer-Protected Stable PbS Colloidal Nanoparticles in a Nonaqueous Solution. *Langmuir* **2002**, *18*, 5287−5292.
(33) Machol, J. L.; Wise, F. W.; Patel, R. C.; Tanner, D. B. Vibronic Quantum Beats in PbS Microcrystallites. *Phys. Rev. B: Condens. Matter Mater. Phys.* **1993**, *48*, 2819−2823.
(34) Choi, H.; Ko, J.-H.; Kim, Y.-H.; Jeong, S. Steric-hindrance-driven Shape Transition in PbS Quantum Dots: Understanding Size-dependent Stability. *J. Am. Chem. Soc.* **2013**, *135*, 5278−5281.
(35) Gadenne, P.; Yagil, Y.; Deutscher, G. Scaling Theory Applied Far Infrared Absorption by Metal-Insulator Composite Materials. *J. Appl. Phys.* **1989**, *66*, 3019−3032.
(36) Plass, R.; Pelet, S.; Krueger, J.; Grätzel, M.; Bach, U. Quantum Dot Sensitization of Organic−Inorganic Hybrid Solar Cells. *J. Phys. Chem. B* **2002**, *106*, 7578−7580.
(37) Hyun, B.-R.; Zhong, Y.-W.; Bartnik, A. C.; Sun, L.; Abruna, H. D.; Wise, F. W.; Goodreau, J. D.; Matthews, J. R.; Leslie, T. M.; Borrelli, N. F. Electron Injection from Colloidal PbS Quantum Dots into Titanium Dioxide Nanoparticles. *ACS Nano* **2008**, *2*, 2206−2212.
(38) Nair, G.; Chang, L.-Y.; Geyer, S. M.; Bawendi, M. G. Perspective on the Prospects of a Carrier Multiplication Nanocrystal Solar Cell. *Nano Lett.* **2011**, *11*, 2145−2151.
(39) Aerts, M.; Bielewicz, T.; Klinke, C.; Grozema, F. C.; Houtepen, A. J.; Schins, J. M. S.; Siebbeles, L. D. A. Highly Efficient Carrier Multiplication in PbS Nanosheets. *Nat. Commun.* **2014**, *5*, 3789−3784.
(40) Schliehe, C.; Juarez, B. H.; Pelletier, M.; Jander, S.; Greshnykh, D.; Nagel, M.; Meyer, A.; Förster, S.; Kornowski, A.; Klinke, C.; Weller, H. Ultrathin PbS Sheets by Two-Dimensional Oriented Attachment. *Science* **2010**, *329*, 550−553.
(41) Bhandari, G. B.; Subedi, K.; He, Y.; Jiang, Z.; Leopold, M.; Reilly, N.; Lu, H. P.; Zayak, A. T.; Sun, L. Thickness-Controlled Synthesis of Colloidal PbS Nanosheets and Their Thickness-Dependent Energy Gaps. *Chem. Mater.* **2014**, *26*, 5433−5436.
(42) Dogan, S.; Bielewicz, T.; Cai, Y.; Klinke, C. Field−effect Transistors Made of Individual Colloidal PbS Nanosheets. *Appl. Phys. Lett.* **2012**, *101*, 073102−1−073102−4.
(43) Yu, K.; Liu, X.; Zeng, Q.; Leek, D. M.; Ouyang, J.; Whitmore, K. M.; Ripmeester, J. A.; Tao, Y.; Yang, M. Effect of Tertiary and Secondary Phosphines on Low-Temperature Formation of Quantum Dots. *Angew. Chem., Int. Ed.* **2013**, *52*, 4823−4828.
(44) Kiran, B.; Kandalam, A. K.; Rallabandi, R.; Koirala, P.; Li, X.; Tang, X.; Wang, Y.; Fairbrother, H.; Gantefoer, G.; Bowen, K. PbS)32: A Baby Crystal. *J. Chem. Phys.* **2012**, *136*, 024317−1−024317−7.
(45) Williams, D. B.; Carter, C. B. *Transmission Electron Microscopy, A Textbook for Materials Science*; Springer: New York, 2009; Chapter 18..
(46) Liu, J.; Aruguete, D. M.; Jinschek, J. R.; Rimstidt, J. D.; Hochella, M. F., Jr. The Non-oxidative Dissolution of Galena Nanocrystals: Insights into Mineral Dissolution Rates as a Function of Grain Size, Shape, and Aggregation State. *Geochim. Cosmochim. Acta* **2008**, *72*, 5984−5996.
(47) Kaneko, F.; Yamazaki, K.; Kitagawa, K.; Kikyo, T.; Kobayashi, M.; Kitagawa, Y.; Matsuura, Y.; Sato, K.; Suzuki, M. Structure and Crystallization Behavior of the β Phase of Oleic Acid. *J. Phys. Chem. B* **1997**, *101*, 1803−1809.
(48) Scherrer, P. Bestimmung der Größe und der Inneren Struktur von Kolloidteilchen mittels Röntgenstrahlen. *Nach. Ges. Wissen. Göttingen, Math.-physik. Kl.* **1918**, *2*, 98−100.

DOI: 10.1021/acs.chemmater.5b03088
Chem. Mater. 2015, 27, 8248−8254

3-6-2 High-Performance n- and p-Type Field-Effect Transistors Based on Hybridly Surface-Passivated Colloidal PbS Nanosheets

In this section, the experiments regarding the surface passivation of the nanosheets and their device engineering are presented in the form of a published article. For this article, my responsibility was to develop the idea, fabricating the devices based on the previously synthesized nanosheets and performing the electrical measurements, which also includes the analysis and the interpretation of the results. This is a reprint from: *High Performance n- and p-Type Field-Effect Transistors Based on Hybridly Surface-Passivated Colloidal PbS Nanosheets,* Mohammad Mehdi Ramin Moayed, Thomas Bielewicz, Heshmat Noei, Andreas Stierle, and Christian Klinke. Advanced Functional Materials, **2018**. 1706815[96]. Copyright ©2018 WILEY-VCH Verlag GmbH & Co.

ADVANCED FUNCTIONAL MATERIALS
www.afm-journal.de

High-Performance n- and p-Type Field-Effect Transistors Based on Hybridly Surface-Passivated Colloidal PbS Nanosheets

*Mohammad Mehdi Ramin Moayed, Thomas Bielewicz, Heshmat Noei, Andreas Stierle, and Christian Klinke**

Colloidally synthesized nanomaterials are among the promising candidates for future electronic devices due to their simplicity and the inexpensiveness of their production. Specifically, colloidal nanosheets are of great interest since they are conveniently producible through the colloidal approach while having the advantages of two-dimensionality. In order to employ these materials, according transistor behavior should be adjustable and of high performance. It is shown that the transistor performance of colloidal lead sulfide nanosheets is tunable by altering the surface passivation, the contact metal, or by exposing them to air. It is found that adding halide ions to the synthesis leads to an improvement of the conductivity, the field-effect mobility, and the on/off ratio of these transistors by passivating their surface defects. Superior n-type behavior with a field-effect mobility of 248 $cm^2 V^{-1} s^{-1}$ and an on/off ratio of 4×10^6 is achieved. The conductivity of these stripes can be changed from n-type to p-type by altering the contact metal and by adding oxygen to the working environment. As a possible solution for the post-Moore era, realizing new high-quality semiconductors such as colloidal materials is crucial. In this respect, the results can provide new insights which helps to accelerate their optimization for potential applications.

1. Introduction

The introduction of graphene, a monolayer of carbon atoms with extraordinary properties and potential application in field-effect transistors opened a new pathway for the semiconductor technology based on 2D electronics.[1,2] The field expanded with the realization of other 2D materials such as transition metal dichalcogenides. They showed to have high carrier mobilities (still lower than graphene) and at the same time, very effective gateability due to their sizable bandgap (in contrast to graphene which has a zero bandgap).[3–5] However, the cost-efficient production of such 2D materials on an industry-compatible scale has remained difficult.[6,7]

The colloidal synthesis of nanomaterials offers the possibility to produce high-quality and inexpensive crystals which are confined in one to three dimensions.[7–13] Recently, we showed that this method can also be used for the synthesis of 2D materials such as lead sulfide nanosheets.[14–17] Accurate control over the size and the thickness of these nanosheets makes them promising for future 2D electronics, as they have the advantages of two-dimensionality (superior electrical, optical, and mechanical properties) while they are extremely cheap and simple in production compared to other methods for growing 2D materials such as molecular beam epitaxy (MBE) or chemical vapor deposition (CVD) based methods which need expensive instrumentation.[14–17]

In addition to the size and shape of these nanosheets, controlling their semiconducting behavior and particularly, the polarity of their majority charge carriers are of great importance.[12,18–21] Early characterization of PbS nanosheets showed that they exhibit p-type behavior when they are probed as field-effect transistors.[22] In order to effectively implement these nanosheets into applications like transistors, solar cells, photodetectors, and spintronic devices (based on the Rashba spin–orbit coupling),[22–24] it is crucial to improve the p-type behavior and also to develop the possibility to switch the behavior to n-type.[11,18,19,21] Doping colloidal nanomaterials, in contrast to conventional semiconductors, is complex since it depends on

M. M. Ramin Moayed, Dr. T. Bielewicz, Prof. C. Klinke
Institute of Physical Chemistry
University of Hamburg
20146 Hamburg, Germany
E-mail: christian.klinke@swansea.ac.uk
Dr. H. Noei, Prof. A. Stierle
DESY NanoLab
Deutsches Elektronensynchrotron DESY
22607 Hamburg, Germany
Prof. A. Stierle
Physics Department
University of Hamburg
20355 Hamburg, Germany
Prof. C. Klinke
Department of Chemistry
Swansea University – Singleton Park
Swansea SA2 8PP, UK
The ORCID identification number(s) for the author(s) of this article can be found under https://doi.org/10.1002/adfm.201706815.

DOI: 10.1002/adfm.201706815

© 2018 WILEY-VCH Verlag GmbH & Co. KGaA, Weinheim

several parameters, such as the stoichiometry of the crystals, traps on the surface, passivating ligands and impurities.[18,19,25] Therefore, to successfully dope them, accurate tuning of these parameters is required.

Here, we show how the field-effect transistor (FET) behavior of PbS nanosheets can be tuned during the synthesis or by modification of the fabrication procedure. N-type behavior could be obtained by introducing halide ions to the surface of the nanosheets during the synthesis, while exposure to air was used for p-doping. For both groups, the effect of the contact material was investigated. Eventually, by appropriately adjusting the properties (effective n-doping, selecting the proper contact metal, and using narrower crystals with higher gateability), high-performance FETs with field-effect mobilities of 248 $cm^2 V^{-1} s^{-1}$ and on/off ratios of 4×10^6 could be achieved. This level of performance is significantly higher compared to other colloidal materials[26–31] and is comparable with the functionality of layered transition metal dichalcogenides (TMDs) and other similar 2D materials.[32,33] Tuning and improving the transistor behavior of PbS nanosheets is an important step in regard to potential implementations in future electronics, especially for the systems which require extremely low cost components, for example, for the internet of the things.[34]

2. Results and Discussion

Different PbS nanosheets were synthesized with a height of about 10 nm and lateral dimensions larger than 2 µm using different coligands for surface passivation[15–17] (Figure S1, Supporting Information, shows more details about the sheets). The products were suspended in toluene, to be used for the fabrication of field-effect transistors (details can be found in the Experimental Section). In the first set of the experiments, the surface passivation effect of different coligands on the FET behavior of the nanosheets was investigated. For this purpose, three types of nanosheets were synthesized: For the first sample, a fluoroalkane was employed for the passivation of the nanosheets, by adding 2.9 mmol fluoroheptane (FH) to the reaction. The second sample was prepared with a low amount of chloride ions. For this purpose, 2.9 mmol chloroheptane (CH) was added to the synthesis. Eventually, for the third sample a high amount of chloride ions was introduced by 7.5 mmol trichloroethylene (TCE). The amount of the main ligand (oleic acid) remained constant for all the samples. As a result, the nanosheets are comparable in thickness and lateral size (Figure S2, Supporting Information). **Figure 1** depicts a scanning-electron microscope (SEM) image of the fabricated devices for these measurements. In order to enhance the expected n-type behavior, the nanosheets were contacted with Ti, a low work-function metal which promotes electron transport due to the formation of Ohmic contacts for electrons and Schottky barriers for holes.[11,23,35,36] The devices were kept in vacuum for 1 d before starting the measurements in order to completely release adsorbed oxygen (as a promoter for p-type behavior[11,18,20,25,35,37,38]) from the surface.

Figure 2A–D shows the output characteristics of these devices. For the sample synthesized with FH (Figure 2A), at low bias voltages, the current is linearly proportional to the voltage, which shows the formation of low resistance contacts.[39,40] By increasing the bias voltage, a clear saturation is observable for the current. This can be attributed to the saturation of the carriers drift velocity in higher electric fields and is due to the relatively high level of scattering during charge transport.[41,42] By using Cl^- ions, the samples conduct more currents (Figure 2B). This effect is more pronounced when the amount of Cl^- ions is increased (Figure 2C). The conductivity increases from 0.78 (with FH) to 131 mS cm^{-1} (with the low amount of Cl^-), and to 300 mS cm^{-1} (with the high amount of Cl^-) due to optimization of the surface passivation. No significant current saturation can be observed for the Cl^- passivated samples, which manifests charge transports with lower scattering.[41,42] A comparison (Figure 2D) clearly shows the improvements in the conductivity and the linearity of the current, when Cl^- passivation is used or when more Cl^- ions are provided to the crystal.

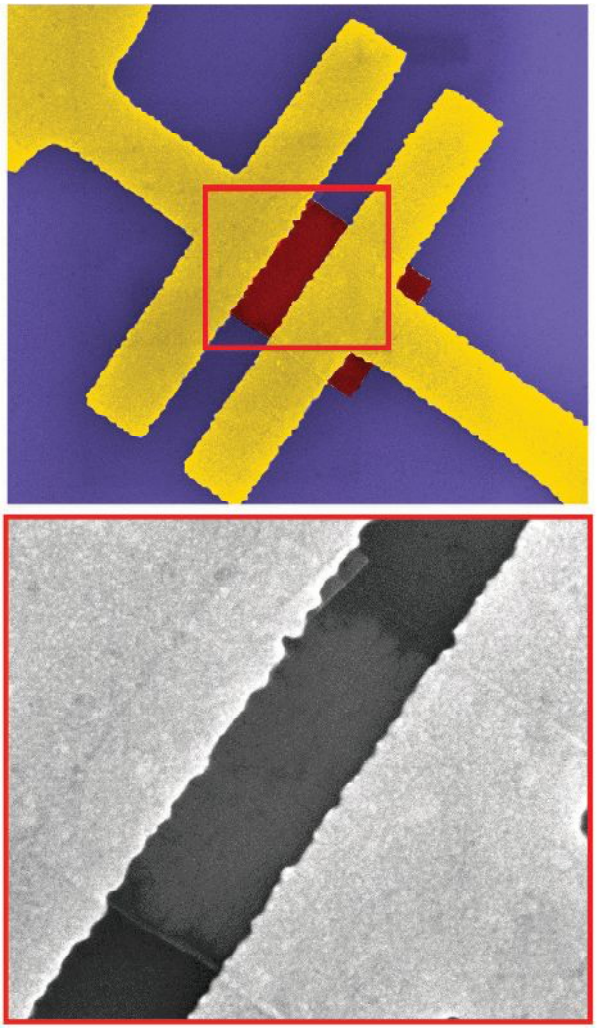

Figure 1. Device preparation. Colorized SEM image of the Ti contacted nanosheets synthesized with chloride coligands for surface passivation. The used coligands are a fluoroalkane (2.9 mmol fluoroheptane), a low amount of a chloroalkane (2.9 mmol chloroheptane), and a higher amount of a chloroalkane (7.5 mmol TCE).

© 2018 WILEY-VCH Verlag GmbH & Co. KGaA, Weinheim

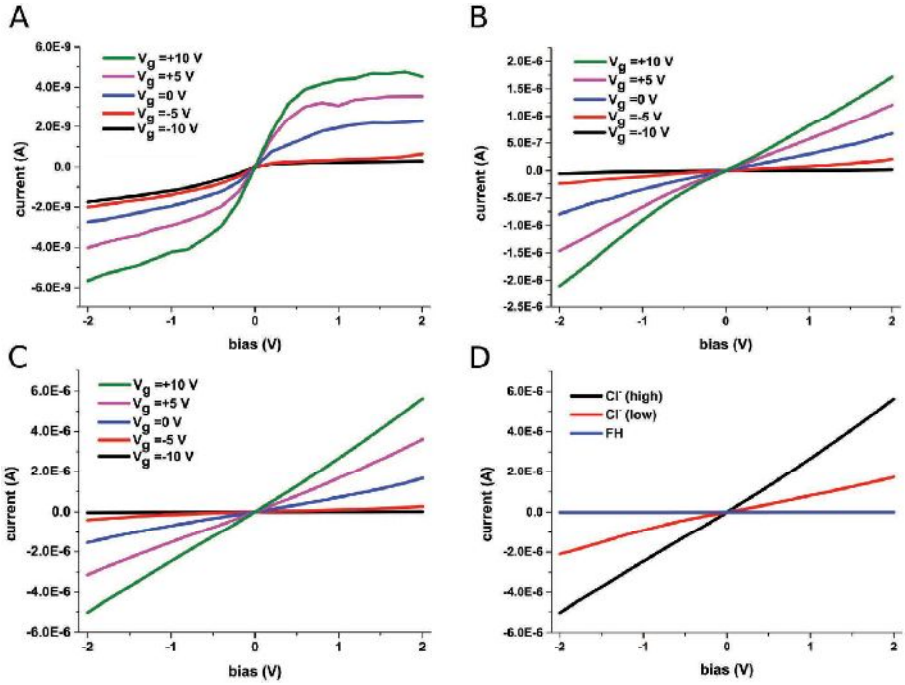

Figure 2. Output characteristics. A) Output characteristics of the fluoroalkane-based sample. The current saturation is a sign of scattering in the channel. B,C) Output characteristics of the samples passivated with a low amount and a high amount of Cl^- ions, respectively. D) Influence of the surface passivation on the *I*–*V* curve of the nanosheets (V_g = +10 V). Adding more Cl^- to the synthesis increases the current level and its linearity.

Further, we investigated the gate dependency by sweeping the back gate from −10 to 10 V. Devices prepared from FH-based nanosheets demonstrate a slight n-type behavior, introducing electrons as majority carriers (**Figure 3**A). The field-effect mobility of these devices was calculated by employing Equation (1) where L is the channel length and C is the gate capacitance, which can be calculated by Equation (2)

$$\mu_{FE} = \frac{dI_{DS}}{dV_g} \cdot \frac{L^2}{V_{DS} C} \quad (1)$$

$$C = \varepsilon_0 \varepsilon_r \frac{L \cdot W}{d} \quad (2)$$

In this equation, ε_0 and ε_r are the permittivity of vacuum and SiO_2, respectively, W is the channel width, and d is the thickness of the gate dielectric (SiO_2).[22] For this sample, the field-effect mobility was calculated to be up to 0.15 $cm^2\ V^{-1}\ s^{-1}$, which is relatively small compared to similar systems. The maximum achieved on/off ratio is 235 which is also a moderate value.

By adding chloroheptane to the synthesis, the transfer characteristics of the sheets are clearly improved, as can be seen in Figure 3B. More pronounced n-type behavior can be observed, while the field-effect mobility and the on/off ratio are, respectively, up to 5.5 $cm^2\ V^{-1}\ s^{-1}$ and 1300. By increasing the amount of Cl^-, further improvements can be achieved. Figure 3C shows the transfer characteristics of the related devices. Field-effect mobilities of up to 26.06 $cm^2\ V^{-1}\ s^{-1}$ and on/off ratios up to 8.8×10^4 introduce this group of nanosheets as superior compared to similar colloidal PbS nanosheets.[15,22,34] Significant improvements are also observable by considering the subthreshold swing of these devices, which decreases from 5 to 3 V dec^{-1} by replacing FH by CH, and to 1.1 V dec^{-1} by increasing the amount of Cl^-.

Figure 3D provides an overview about the gating behavior of these devices. One can clearly conclude that by adding Cl^- ions, the FET properties of the nanosheets are enhanced. For the best sample (the one with the highest amount of Cl^-) passivation leads to relatively low "off-currents" as well as relatively high "on-currents," which are both the main goals for the optimization of electronic materials.

The surface of colloidal nanocrystals like PbS nanosheets contains trap states originating from dangling bonds, due to the periodicity mismatch of the crystal facet and the surface ligands.[7,9,18–20,43,44] Because of the high surface-to-volume ratio, these trap states can significantly hamper the electron transport.[20,37,44–47] Although different organic ligands (e.g., oleic acid for our case) are used during the synthesis, they are not able to completely passivate the surface due to their molecule length, and a certain amount of dangling bonds remains unpassivated between the ligands, since they are unreachable for the long organic molecules.[9,18,44] To overcome this problem, the idea of hybrid passivation of these crystals has been suggested by employing X-type elemental inorganic ligands in addition to their organic ligands. It has been shown for 0D nanoparticles that halide ions, as atomic point-like ligands, can penetrate into the organic layer and passivate the remaining dangling bonds between them.[8–11,18,19,43,44,48] In

© 2018 WILEY-VCH Verlag GmbH & Co. KGaA, Weinheim

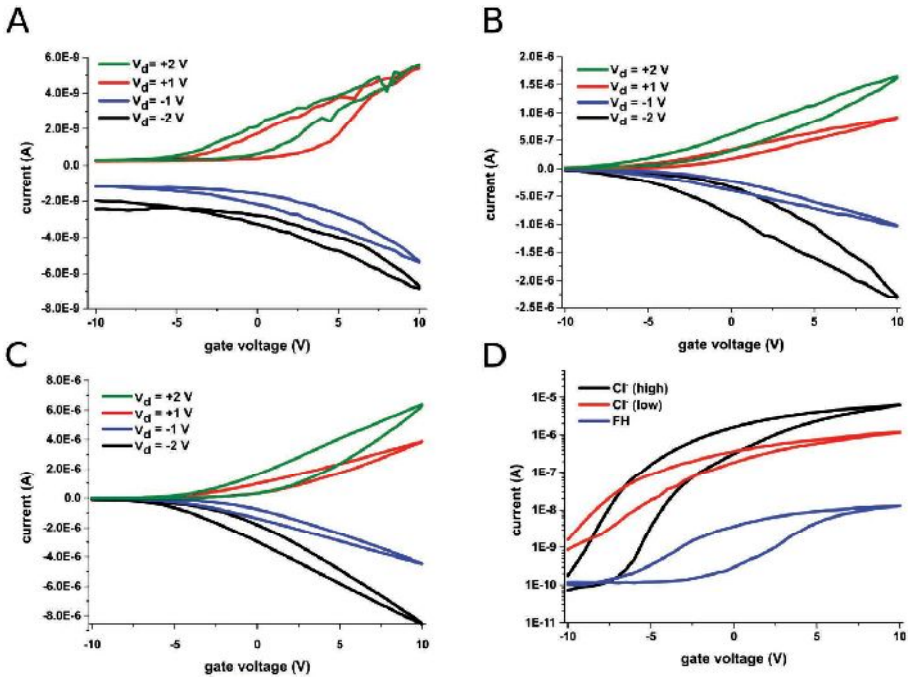

Figure 3. Transfer characteristics. A) Transfer characteristics of the fluoroalkane-based sample with poor gateability. B) Transfer characteristics for the sample passivated with the low amount of Cl^-, which shows improvements in the FET properties. C) Same measurement on the sample with the high amount of Cl^-, representing the highest field-effect mobility and on/off ratio among the three samples. D) Comparison between the transfer characteristics of all the samples.

order to passivate the surface, halide ions can be introduced to the crystal either after the synthesis.[8,12,18,44] or during the synthesis as the precursor or as the coligands.[8–10,43,48–50] In our case, halogenoalkanes which are used as coligands decompose during the synthesis and produce halide ions. These halide ions can be attached to the surface of the crystal and passivate the dangling bonds. Among the different used halogenoalkanes, passivation with fluoroalkanes is the least effective one. There are two reasons for that: First, decomposition of fluoroalkanes is the most difficult one among the halogenoalkanes due to the high electronegativity of F. Therefore, the production of F^- ions during the synthesis is also more difficult compared to other halide ions. Second, calculations show that the formation of the Pb—F bond is unlikely because of its positive formation energy, which decreases the adsorption possibility of F^- (to the crystal) and increases its desorption possibility (from the crystal), resulting in an unsuccessful or less effective passivation.[8,11] This explains the relatively poor transport properties in our fluoroalkane-based nanosheets. The remaining trap states hinder the transport of the electrons in the semiconductor channel, leading to lower field-effect mobilities.[18,20,45,51] Further, the resulting mid-gap states diminish the switching and reduce the on/off ratio.[7,9,18–20,43,44,46,51]

Replacing the fluoroalkane with chloroalkane improves the effectiveness of the passivation, since chloroalkanes decompose more easily compared to fluoroalkanes and the Pb—Cl bond has a negative formation energy, which makes it more probable than the Pb—F bond to be formed.[8,11,18,49] By increasing the amount of chloroalkane in the synthesis, more Cl^- is provided and passivation is improved by increasing the coverage. Such passivation reduces the amount of trap states on the surface. During the transport, more electrons are able to move freely, without being trapped which leads to more pronounced n-type behaviors.[8,9,11,18–20,37,46] Also due to less scattering, the field-effect mobility is increased.[7,18,20,45,51] These phenomena result in higher on-currents.[18,35,37,46] At the same time, passivating the traps removes the mid-gap states from the band structure of the crystal, leading to lower off-currents.[9,18–20,43,44,46,51]

As it can be observed in **Figure 4**A, the field-effect mobility and the on/off ratio can be improved by two and three orders of magnitude, respectively, which is the first and strongest proof for the effectiveness of our passivation procedure. Our results are also in agreement with other works, which use similar methods to passivate the surface of low-dimensional colloidal nanoparticles.[8–10,43,48–50] Eventually, to verify the mentioned reason for the observed improvements in the FET behavior of the nanosheets, we tracked the existence of the coligands on the surface by means of X-ray photoelectron spectroscopy (XPS) on thin films of nanosheets.[48,52] Also these measurements show that the nanosheets with the better performance have higher amounts of Cl on the surface (Figure 4B). To clarify this argument, Figure 4C shows the Pb 4f peaks for the Cl^- passivated samples (Figure S3, Supporting Information, shows these peaks for the sample made with FA). The Pb 4f peaks centered at 137.6 and 142.4 eV are attributed to the binding energy of Pb 4f 7/2 and Pb 4f 5/2 of PbS, respectively. The XPS peaks at 138.8 and 143.7 eV are assigned to Pb 4f 7/2 and Pb 4f 5/2 of Pb^{2+} in $PbCl_2$, showing the existence of Cl on the surface with

© 2018 WILEY-VCH Verlag GmbH & Co. KGaA, Weinheim

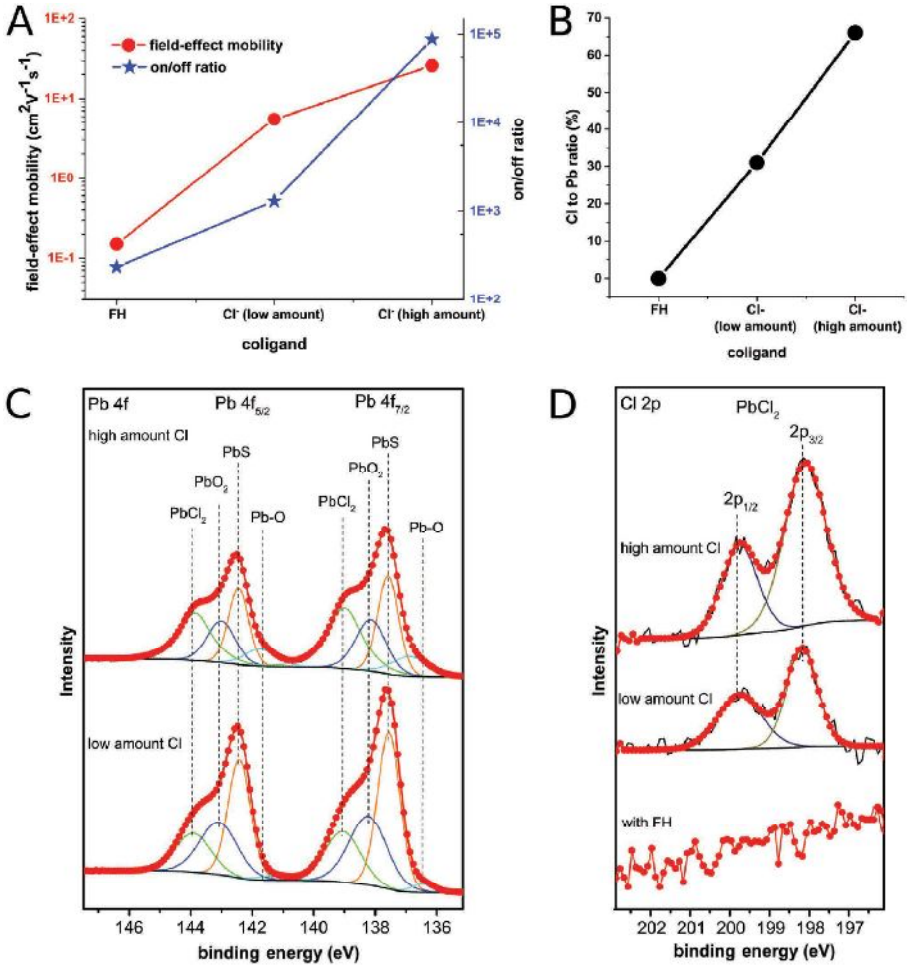

Figure 4. Device and chemical analysis. The passivation effect on the FET behavior of the nanosheets. A) Field-effect mobility and on/off ratio of the samples with different passivations. By employing Cl^- ions, these parameters are improved by two and three orders of magnitude, respectively. B) The ratio of Cl to Pb acquired by the XPS measurements which is in agreement with the trend of the improvements in the electrical properties. C) Deconvoluted XPS spectra of the Cl^- passivated samples for the Pb 4f region show the existence of Cl^- bound to Pb^{2+}. D) XPS peaks of the samples for the Cl 2p region, showing the increase of the Cl content, for the samples with better electrical properties.

the highest amount for the sample synthesized with the high amount of Cl, which is in agreement with the observed improvements in electrical properties. The peaks at 138.2, 143.1 eV and 136.9, 141.7 eV are assigned to Pb 4f 7/2 and Pb 4f 5/2 of PbO_2 and PbO, respectively. Further, Figure 4D shows the Cl 2p peaks of the samples, with the peaks at 198.2 and 199.8 eV which are attributed to $PbCl_2$. It also demonstrates the increase of the Cl content (due to the higher intensity of the peaks, relative to the PbS peaks), when more chloroalkane is used during the synthesis, in agreement with the previous observations. Therefore, it can be undoubtedly concluded that Cl^- ions, which are introduced to the synthesis by chloroalkanes, are attached to the surface of the nanosheets and improve their properties by surface passivation, although using fluoroalkanes might lead to a poorly passivated or even unpassivated surface.

One might argue that the observed effects can be attributed to the existence of mobile Cl^- ions in the system (e.g., n-type behavior with a high conductivity and mobility). However, there are clear reasons which exclude this possibility. All the nanosheets are washed several times at the end of the synthesis, which removes any kind of impurities including mobile ions. The XPS spectra (Figure 4C,D) also show that Cl is bound to Pb and does not exist as free Cl^- ions. More importantly, by investigating the off-currents of the devices, which are extremely low, it can be concluded that no mobile ions are present in the system. Mobile ions normally reduce the on/off ratio by increasing the subthreshold leakage current of the FETs. Since the off-current of our devices decreases by applying more ions, it can be concluded that the employed ions do not remain as mobile ions and therefore, the improvements are solely due to the passivation effect from the bound ions.

It is worthy to point out, that even higher conductivities, field-effect mobilities and on/off ratios are expected when the nanosheets are passivated with Br^- ions (due to the same reason for the superiority of Cl^- over F^-).[8,11,18] However, it has been shown that adding Br^- ions to the synthesis hinders the

© 2018 WILEY-VCH Verlag GmbH & Co. KGaA, Weinheim

growth of 2D crystals, leading to the production of only 0D nanoparticles, which cannot be individually measured as a field-effect transistor.[17]

As recently shown, by increasing the amount of chloroalkane in the synthesis (the number of Cl^- ions on the crystal), the lateral shape of the nanosheets is transformed to stripes.[16] Field-effect transistors based on these stripes show even higher performances (compared to the squared sheets), since the gate has a more effective influence on the channel conductivity, resulting from the reduced width of the quasi-1D crystal.[16,53–56]

In order to fabricate high-performance devices, we used 5.9 mmol of chlorotetradecane (CTD) to synthesize the nanosheets. Since the amount of chloroalkane is relatively high, surface traps are effectively passivated while the shape of the crystal changes to laterally confined stripes, with a width below 100 nm. Ti contacts were used (an SEM image of the device is depicted in Figure S4, Supporting Information) and adsorbed O_2 molecules were released from the surface by keeping the sample in vacuum, in order to further improve the n-type conductivity. **Figure 5**A shows the output characteristics of these stripes. The current is linearly proportional to the voltage without being saturated, which is a sign for the formation of Ohmic contacts (linearity in the low voltage regime)[39,40] and for the successful surface passivation (no scattering at higher voltages).[41,42] The conductivity of these crystals is up to 1916 mS cm^{-1}.

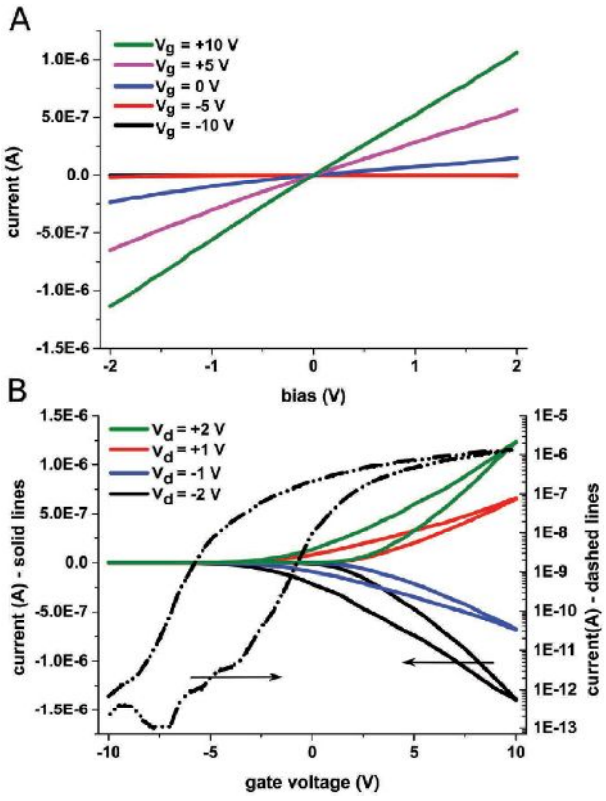

Figure 5. Stripe characteristics. A) Output characteristics of the highly passivated stripes, contacted with Ti, and measured in vacuum. B) Transfer characteristics for the same sample. Effective switching can be observed with the high field-effect mobility and on/off ratio.

By investigating the transfer characteristics (Figure 5B), a significantly improved n-type behavior can be observed. The field-effect mobility for these stripes can be up to 248 $cm^2\ V^{-1}\ s^{-1}$ with an on/off ratio of 4×10^6 and a subthreshold swing of 650 mV dec^{-1}. The FET behavior of these stripes shows significant improvements compared to almost all the previously reported systems based on 2D PbS crystals or other forms of colloidal materials.[26–28] The field-effect mobility of electrons approaches even the bulk value. Such improvements are achieved since tunnel barriers which normally exist between the 0D nanoparticles are not present here in the continuous 2D or quasi 1D crystal (leading to a higher conductivity). Having the confinement in the height improves the gateability of the sheets, or in other words, increases the on/off ratio. Eventually, the passivation effect removes the surface defects of the crystal and signifies the functionality. The unique superiority of these stripes compared to other colloidally made crystals is that they show high field-effect mobility and on/off ratio simultaneously, the property which has been rarely reported in literature.[26–31] The performance of these FETs can also be further improved simply by employing thinner gate dielectrics, which is 300 nm for the current devices.[40,47] High amounts of mobile electrons, low scattering, and negligible amounts of mid-gap states (all achieved by eliminating the trap states and by releasing oxygen from the surface), formation of Ohmic contacts, and effective control over the channel (due to its quasi-1D shape) result in high conductivities, remarkably low off-currents (below the noise level of the measurement), and sharp transitions between the on-state and the off-state.

As already mentioned, in order to properly employ the n-type character of the sheets, it is necessary to use Ti contacts (a material with a low work function)[11,23,35,36] and keep the sample in vacuum to release adsorbed O_2.[11,18,20,25,35,37,38] However, these factors can be exploited to induce p-type behavior.

In order to examine the effect of adsorbed O_2 on the FET behavior of the stripes, the measurements were repeated in air after exposing the devices to air for a few hours. As can be seen in **Figure 6**, the n-type behavior of the stripes is significantly weakened and poor functionality with reduced field-effect mobilities and on/off ratios is detected (mobility: 46 $cm^2\ V^{-1}\ s^{-1}$, on/off ratio: 82×10^3, subthreshold swing: 1.4 V dec^{-1}). Comparable effects from air are also observed for the normal (squared) nanosheets with different coligands (Figure S5, Supporting Information). By adsorption of oxygen (as a p-dopant) from air to the surface, electrons are withdrawn from the channel, resulting in less electron concentrations and poor n-type behaviors.[11,18,20,25,35,37,38] It can also change the band alignment of the semiconductor and the contact metal, which hinders the n-type transport.[21,47]

Figure 6 also demonstrates the transfer characteristics of the stripes contacted with Au (a material with a high work function) and measured in vacuum. As can be seen, by weakening the n-type conduction, the field-effect mobility and the on/off ratio decrease drastically, when the stripes are contacted with Au (mobility: 6.8 $cm^2\ V^{-1}\ s^{-1}$, on/off ratio: 100, subthreshold swing: 3.3 V dec^{-1}), which is also true for the squared nanosheets (Figure S6, Supporting Information). By changing the work function of the contact metal, the band alignment between the crystal and the contacts is changed. Using a

© 2018 WILEY-VCH Verlag GmbH & Co. KGaA, Weinheim

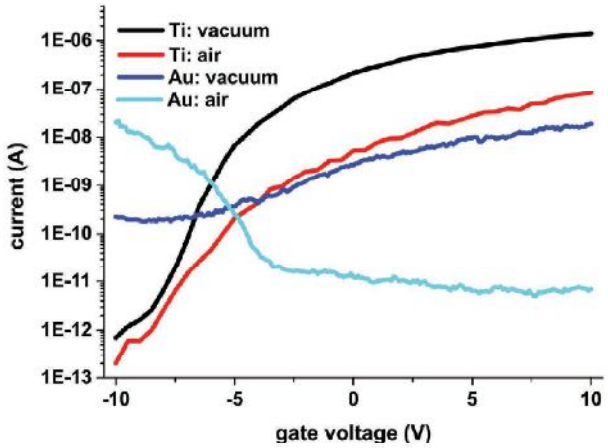

Figure 6. Charge carrier manipulation. Variation of the transfer characteristics of the stripes, by changing the contact metal (Ti or Au) and the working environment (vacuum or air). Using the Au contacts or measuring in air weakens the n-type behavior. Au contacted stripes show p-type behavior in air.

material with a high work function, such as Au, leads to the appearance of a Schottky barrier for electrons and Ohmic contacts for holes. This hampers the electron transfer and facilitates the hole transfer in the system.[11,23,35,36] Since these measurements have been performed in vacuum, the effect of O_2 adsorption is not contributing to the poor behavior of the stripes.

By employing both effects (using Au contacts and measuring in air), the character of the stripes is changed to a clear p-type behavior. The same stripes which show n-type behavior were contacted with gold and were measured in air. The result is shown in Figure 6. Analysis of the p-type conduction in the transfer characteristics reveals that holes are the majority carriers in these devices. Their field-effect mobility reaches 10.1 $cm^2 V^{-1} s^{-1}$ with an on/off ratio of 5000 and a subthreshold swing of 1 V dec^{-1}. The p-type conductivity of the crystal is intensified by increasing the hole concentration, since O_2 acts as a p-dopant,[11,18,20,25,35,37,38] supported by the formation of Ohmic contacts for holes.[11,21,23,35,36,47] Compared to other colloidal materials, these stripes represent relatively higher field-effect mobilities and on/off ratios also in the p-type regime,[22,28] originating from the continuity of the crystal and the effective surface passivation. However, their functionality is still superior in the n-type regime.

3. Conclusion

In conclusion, we have investigated the tunability of 2D colloidal PbS nanosheets by changing the surface passivation, the contact metal, and the working environment. By adding chloroalkanes to the synthesis of these nanosheets, their surface defects were passivated, leading to improved n-type transistor behaviors. The results revealed that chloride is a more efficient passivator compared to fluoride, and its effect can be improved by increasing the amount of chloride in the synthesis. By using passivated narrow stripes, contacted with Ti, record high-performance n-type FETs could be realized when operating in vacuum. On the other hand, the same crystal was contacted with Au and measured in air which showed p-type behavior. Our results can be the next step in improving and fine-tuning the recently introduced colloidal semiconductors for future electronics, especially for inexpensive applications.

4. Experimental Section

Synthesis of Nanosheets: All chemicals were used as received. The chemicals used were: lead(II) acetate trihydrate (Aldrich, 99.999%), diphenyl ether (Aldrich, 99%+), oleic acid (Aldrich, 90%), trioctylphosphine (TOP; ABCR, 97%), FH (Aldrich, 98%), CH (Aldrich, 99%), TCE (Aldrich, 96%), CTD (Aldrich, 98%), thioacetamide (TAA; Sigma-Aldrich, >99.0%), thiourea (TU; Aldrich, >99.0%), and dimethyl formamide (DMF; Sigma- Aldrich, 99.8% anhydrous).

A 50 mL four-neck flask with a thermocouple, a thermometer, a condenser, and septum, was used. Lead acetate trihydrate (860 mg, 2.3 mmol) was dissolved in diphenyl ether (10 mL) and oleic acid (3.5 mL, 10 mmol). For the synthesis of the sheets with TCE, TOP was added (0.2 mmol). The solution was heated to 75 °C and a vacuum was applied for 2 h at 0.3 mbar, to transform lead acetate into lead oleate and to remove acetic acid in the same step. Then, under a nitrogen atmosphere, the solution was heated to 100 °C, in which, the desired coligands were added rapidly. After that, the temperature was increased to the reaction temperature (the sample with FH: 170 °C, the sample with CH: 170 °C, the sample with TCE: 130 °C, and the stripes with CTD: 160 °C). To start the reaction, 0.2 mL of 0.04 g TAA (0.5 mmol) in DMF (6.5 mL) was added (for stripes: 0.2 mL of 0.04 g TU in 6 mL DMF). The solution was stirred at 700 rpm for 5 min before cooling down. To separate the product from the solvent and by-products, the reaction solution was centrifuged at 4000 rpm for 3 min and the precipitant washed two times with toluene. The product was stored suspended in toluene.

Device Preparation and Measurements: After the synthesis, a diluted suspension of the nanosheets was spin-coated on a Si/SiO_2 substrate, and contacted individually by electron-beam lithography, followed by thermal evaporation of the desired metal (according to the scope of the measurement). The achieved devices were transferred to a probe station (Lakeshore-Desert) connected to a semiconductor parameter analyser (Agilent B1500a), for room-temperature electrical measurements in air or vacuum. All the measurements were carried out with back-gate geometry, using a highly doped silicon substrate with 300 nm thermal oxide as gate dielectric.

XPS Measurements: XPS measurements were carried out using a high-resolution 2D delay line detector. A monochromatic Al Kα X-ray source (photon energy 1486.6 eV; anode operating at 15 kV) was used as incident radiation. XPS spectra were recorded in fixed transmission mode. A pass energy of 20 eV was chosen, resulting in an overall energy resolution better than 0.4 eV. Charging effects were compensated by using a flood gun. The binding energies were calibrated based on the graphitic carbon 1 s peak at 284.8 eV.[57]

Supporting Information

Supporting Information is available from the Wiley Online Library or from the author.

Acknowledgements

M.M.R.M., T.B., and C.K. gratefully acknowledge financial support of the European Research Council via the ERC Starting Grant "2D-SYNETRA" (Seventh Framework Program FP7, Project: 304980). C.K. thanks the

© 2018 WILEY-VCH Verlag GmbH & Co. KGaA, Weinheim

German Research Foundation DFG for financial support in the frame of the Cluster of Excellence "Center of ultrafast imaging CUI" and the Heisenberg scholarship KL 1453/9-2. M.M.R.M. thanks the PIER Helmholtz Graduate School for the Ph.D. grant. Michael Wagstaffe is acknowledged for helping with the XPS measurements.

Conflict of Interest

The authors declare no conflict of interest.

Keywords

colloidal synthesis, high-performance field-effect transistors, hybrid surface passivation, lead sulfide, nanosheets

Received: November 23, 2017
Revised: February 22, 2018
Published online:

[1] A. K. Geim, K. S. Novoselov, *Nat. Mater.* **2007**, *6*, 183.
[2] F. Schwierz, *Nat. Nanotechnol.* **2010**, *5*, 487.
[3] K. F. Mak, C. Lee, J. Hone, J. Shan, T. F. Heinz, *Phys. Rev. Lett.* **2010**, *105*, 136805.
[4] B. Radisavljevic, A. Radenovic, J. Brivio, V. Giacometti, A. Kis, *Nat. Nanotechnol.* **2011**, *6*, 147.
[5] L. Li, Y. Yu, G. J. Ye, Q. Ge, X. Ou, H. Wu, D. Feng, X. H. Chen, Y. Zhang, *Nat. Nanotechnol.* **2014**, *9*, 372.
[6] F. Bonaccorso, A. Lombardo, T. Hasan, Z. Sun, L. Colombo, A. C. Ferrari, *Mater. Today* **2012**, *15*, 564.
[7] D. V. Talapin, C. B. Murray, *Science* **2005**, *310*, 86.
[8] J. Y. Woo, J. H. Ko, J. H. Song, K. Kim, H. Choi, Y. H. Kim, D. C. Lee, S. Jeong, *J. Am. Chem. Soc.* **2014**, *136*, 8883.
[9] J. Zhang, J. Gao, E. M. Miller, J. M. Luther, M. C. Beard, *ACS Nano* **2014**, *8*, 614.
[10] A. Shapiro, Y. Jang, A. Rubin-Brusilovski, A. K. Budniak, F. Horani, A. Sashchiuk, E. Lifshitz, *Chem. Mater.* **2016**, *28*, 6409.
[11] Z. Ning, O. Voznyy, J. Pan, S. Hoogland, V. Adinolfi, J. Xu, M. Li, A. R. Kirmani, J. P. Sun, J. Minor, K. W. Kemp, H. Dong, L. Rollny, A. Labelle, G. Carey, B. Sutherland, I. Hill, A. Amassian, H. Liu, J. Tang, O. M. Bakr, E. H. Sargent, *Nat. Mater.* **2014**, *13*, 822.
[12] W. K. Bae, J. Joo, L. A. Padilha, J. Won, D. C. Lee, Q. Lin, W. K. Koh, H. Luo, V. I. Klimov, J. M. Pietryga, *J. Am. Chem. Soc.* **2012**, *134*, 20160.
[13] F. Gerdes, C. Navío, B. H. Juárez, C. Klinke, *Nano Lett.* **2017**, *17*, 4165.
[14] C. Schliehe, B. H. Juarez, M. Pelletier, S. Jander, D. Greshnykh, M. Nagel, A. Meyer, S. Foerster, A. Kornowski, C. Klinke, H. Weller, *Science* **2010**, *329*, 550.
[15] T. Bielewicz, S. Dogan, C. Klinke, *Small* **2014**, *11*, 826.
[16] T. Bielewicz, M. M. R. Moayed, V. Lebedeva, C. Strelow, A. Rieckmann, C. Klinke, *Chem. Mater.* **2015**, *27*, 8248.
[17] T. Bielewicz, E. Klein, C. Klinke, *Nanotechnology* **2016**, *27*, 355602.
[18] A. Stavrinadis, G. Konstantatos, *ChemPhysChem* **2016**, *17*, 632.
[19] M. Shim, P. Guyot-Sionnest, *Nature* **2000**, *407*, 981.
[20] D. M. Balazs, M. I. Nugraha, S. Z. Bisri, M. Sytnyk, W. Heiss, M. A. Loi, *Appl. Phys. Lett.* **2014**, *104*, 112104.
[21] V. Derycke, R. Martel, J. Appenzeller, P. Avouris, *Appl. Phys. Lett.* **2002**, *80*, 2773.
[22] S. Dogan, T. Bielewicz, Y. Cai, C. Klinke, *Appl. Phys. Lett.* **2012**, *101*, 073102.
[23] S. Dogan, T. Bielewicz, V. Lebedeva, C. Klinke, *Nanoscale* **2015**, *7*, 4875.
[24] M. M. Ramin Moayed, T. Bielewicz, M. S. Zollner, C. Herrmann, C. Klinke, *Nat. Commun.* **2017**, *8*, 15721.
[25] S. J. Oh, C. Uswachoke, T. Zhao, J. H. Choi, B. T. Diroll, C. B. Murray, C. R. Kagan, *ACS Nano* **2015**, *9*, 7536.
[26] J. Lee, M. V. Kovalenko, J. Huang, D. S. Chung, D. V. Talapin, *Nat. Nanotechnol.* **2011**, *6*, 348.
[27] D. S. Dolzhnikov, H. Zhang, J. Jang, J. S. Son, M. G. Panthani, T. Shibata, S. Chattopadhyay, D. V. Talapin, *Science* **2015**, *347*, 425.
[28] D. M. Balazs, K. I. Bijlsma, H. Fang, D. N. Dirin, M. Döbeli, M. V. Kovalenko, M. A. Loi, *Sci. Adv.* **2017**, *3*, 1558.
[29] J. Jang, D. S. Dolzhnikov, W. Liu, S. Nam, M. Shim, D. V. Talapin, *Nano Lett.* **2015**, *15*, 6309.
[30] J. Choi, A. T. Fafarman, S. J. Oh, D. Ko, D. K. Kim, B. T. Diroll, S. Muramoto, J. G. Gillen, C. B. Murray, C. R. Kagan, *Nano Lett.* **2012**, *12*, 2631.
[31] D. K. Kim, Y. Lai, B. T. Diroll, C. B. Murray, C. R. Kagan, *Nat. Commun.* **2012**, *3*, 1216.
[32] B. Radisavljevic, A. Radenovic, J. Brivio, V. Giacometti, A. Kis, *Nat. Nanotechnol.* **2011**, *6*, 147.
[33] H. Qiu, L. Pan, Z. Yao, J. Li, Y. Shi, X. Wang, *Appl. Phys. Lett.* **2012**, *100*, 123104.
[34] D. K. Kim, Y. Lai, T. R. Vemulkar, C. R. Kagan, *ACS Nano* **2011**, *5*, 10074.
[35] Y. Cheng, R. Yang, J. P. Zheng, Z. L. Wang, P. Xiong, *Mater. Chem. Phys.* **2012**, *137*, 372.
[36] H. Fang, S. Chuang, T. C. Chang, K. Takei, T. Takahashi, A. Javey, *Nano Lett.* **2012**, *12*, 3788.
[37] Y. Pan, Y. Tao, G. Qin, Y. Fedoryshyn, S. N. Raja, M. Hu, C. L. Degen, D. Poulikakos, *Nano Lett.* **2016**, *16*, 6364.
[38] K. S. Leschkies, M. S. Kang, E. S. Aydil, D. J. Norris, *J. Phys. Chem. C* **2010**, *114*, 9988.
[39] D. Xiang, C. Han, J. Wu, S. Zhong, Y. Liu, J. Lin, X. Zhang, W. Hu, B. Ozyilmaz, A. H. C. Neto, A. T. S. Wee, W. Chen, *Nat. Commun.* **2015**, *6*, 6485.
[40] C. Klinke, J. B. Hannon, A. Afzali, P. Avouris, *Nano Lett.* **2006**, *6*, 906.
[41] C. Hsieh, Y. Chen, J. Lou, *Appl. Phys. Lett.* **2010**, *96*, 022905.
[42] I. Meric, M. Y. Han, A. F. Young, B. Ozyilmaz, P. Kim, K. L. Shepard, *Nat. Nanotechnol.* **2008**, *3*, 654.
[43] K. Kim, D. Yoo, H. Choi, S. Tamang, J. Ko, S. Kim, Y. Kim, S. Jeongm, *Angew. Chem., Int. Ed.* **2016**, *55*, 3714.
[44] A. H. Ip, S. M. Thon, S. Hoogland, O. Voznyy, D. Zhitomirsky, R. Debnath, L. Levina, L. R. Rollny, G. H. Carey, A. Fischer, K. W. Kemp, I. J. Kramer, Z. Ning, A. J. Labelle, K. W. Chou, A. Amassian, E. H. Sargent, *Nat. Nanotechnol.* **2012**, *7*, 577.
[45] Y. Cui, Z. Zhong, D. Wang, W. U. Wang, C. M. Lieber, *Nano Lett.* **2003**, *3*, 149.
[46] E. Polydorou, A. Zeniou, D. Tsikritzis, A. Soultati, I. Sakellis, S. Gardelis, T. A. Papadopoulos, J. Briscoe, L. C. Palilis, S. Kennou, E. Gogolides, P. Argitis, D. Davazogloua, M. Vasilopou, *J. Mater. Chem. A* **2016**, *4*, 11844.
[47] C. Klinke, J. Chen, A. Afzali, P. Avouris, *Nano Lett.* **2005**, *5*, 555.
[48] L. Yuan, R. Patterson, W. Cao, Z. Zhang, Z. Zhang, J. A. Stride, P. Reece, G. Conibeer, S. Huang, *RSC Adv.* **2015**, *5*, 68579.
[49] R. Wang, Y. Shang, P. Kanjanaboos, W. Zhou, Z. Ning, E. H. Sargent, *Energy Environ. Sci.* **2016**, *9*, 1130.
[50] S. R. Kandel, S. Chiluwal, Z. Jiang, Y. Tang, P. J. Roland, K. Subedi, D. M. Dimick, P. Moroz, M. Zamkov, R. Ellingson, J. Hu, A. A. Voevodin, L. Sun, *Phys. Status Solidi RRL* **2016**, *10*, 833.
[51] J. Chang, S. Mao, Y. Zhang, S. Cui, D. A. Steeber, J. Chen, *Biosens. Bioelectron.* **2013**, *42*, 186.
[52] A. J. Morris-Cohen, M. Malicki, M. D. Peterson, J. W. J. Slavin, E. A. Weiss, *Chem. Mater.* **2013**, *25*, 1155.

© 2018 WILEY-VCH Verlag GmbH & Co. KGaA, Weinheim

[53] K. Vamvoukakis, D. Stefanakis, A. Stavrinidis, K. Vassilevski, G. Konstantinidis, M. Kayambak, K. Zekentesi, *Phys. Status Solidi* **2017**, *214*, 1600452.
[54] X. Wang, Y. Chen, M. K. Hong, S. Erramilli, P. Mohanty, *Channel-Width Dependent Enhancement in Nanoscale Field Effect Transistor* **2008**, arXiv preprint arXiv:0802.2140.
[55] M. S. Kang, J. H. Lee, H. S. Lee, S. M. Koo, *J. Nanosci. Nanotechnol.* **2013**, *13*, 7042.
[56] E. Leobandung, J. Gu, L. Guo, S. Y. Chou, *J. Vac. Sci. Technol., B* **1997**, *15*, 2791.
[57] H. Noei, V. Vonk, T. F. Keller, R. Röhlsberger, A. Stierle, *J. Large-Scale Res. Facil.* **2016**, *2*, A76.

© 2018 WILEY-VCH Verlag GmbH & Co. KGaA, Weinheim

3-6-3 Towards colloidal spintronics through Rashba spin-orbit interaction in lead sulphide nanosheets

This section summarizes the findings about the spin transport in the PbS nanosheets through the Rashba spin-orbit coupling, as a published article. For this part of the project, my duty was to develop the idea and the test setup, to fabricate the devices based on the previously synthesized nanosheets, and to perform the spin transport measurements, including the analysis and the interpretation of the results. This is a reprint from: *Towards colloidal spintronics through Rashba spin-orbit interaction in lead sulphide nanosheets,* Mohammad Mehdi Ramin Moayed, Thomas Bielewicz, Martin Sebastian Zöllner, Carmen Herrmann, and Christian Klinke. Nature Communications **2017**, 8, 15721[97]. Copyright ©2017 Macmillan Publishers Limited.

nature COMMUNICATIONS

ARTICLE

Received 13 Dec 2016 | Accepted 20 Apr 2017 | Published 7 Jun 2017

DOI: 10.1038/ncomms15721 OPEN

Towards colloidal spintronics through Rashba spin-orbit interaction in lead sulphide nanosheets

Mohammad Mehdi Ramin Moayed[1], Thomas Bielewicz[1], Martin Sebastian Zöllner[2], Carmen Herrmann[2] & Christian Klinke[1]

Employing the spin degree of freedom of charge carriers offers the possibility to extend the functionality of conventional electronic devices, while colloidal chemistry can be used to synthesize inexpensive and tunable nanomaterials. Here, in order to benefit from both concepts, we investigate Rashba spin–orbit interaction in colloidal lead sulphide nanosheets by electrical measurements on the circular photo-galvanic effect. Lead sulphide nanosheets possess rock salt crystal structure, which is centrosymmetric. The symmetry can be broken by quantum confinement, asymmetric vertical interfaces and a gate electric field leading to Rashba-type band splitting in momentum space at the M points, which results in an unconventional selection mechanism for the excitation of the carriers. The effect, which is supported by simulations of the band structure using density functional theory, can be tuned by the gate electric field and by the thickness of the sheets. Spin-related electrical transport phenomena in colloidal materials open a promising pathway towards future inexpensive spintronic devices.

[1] Institute of Physical Chemistry, University of Hamburg, 20146 Hamburg, Germany. [2] Institute of Inorganic and Applied Chemistry, University of Hamburg, 20146 Hamburg, Germany. Correspondence and requests for materials should be addressed to C.K. (email: klinke@chemie.uni-hamburg.de).

Though in the last decades developments in semiconductor device engineering led to constantly improved performances, nowadays it is very difficult to keep this pace[1,2]. Further challenges in terms of manufacturing cost, flexibility, power consumption and device functionality are ahead, for example, for the internet of things[2,3]. Recent ideas try to address these issues by the introduction of new materials as the active semiconductor channel or new mechanisms of information processing[2,4]. One solution is replacing the electron charge by its spin as an information carrier[4,5]. For this purpose, materials with strong spin–orbit coupling (SOC) are particularly interesting since in these materials spin orientation can be manipulated by an external electrical field[5–8]. In semiconductors, SOC can originate from bulk inversion asymmetry (Dresselhaus SOC) or from structural inversion asymmetry (Rashba SOC)[5–7,9,10]. Since Rashba SOC can be influenced by customizing the structure (for example, by confining the material) or by a gate voltage, it is being studied comprehensively[5–7,10]. As a further development in data processing, the concept of valleytronics has been introduced for materials with multiple valleys (multiple extrema with equal energies) in the band structure[11–14]. By controlling the number of carriers in each valley, a so-called valley-polarized current can be produced, which leads to an additional degree of freedom[4,12–14]. As a consequence of spin–valley coupling in these materials, it has been shown that the valleys can be also populated selectively based on the spin of the carriers[11–13,15].

Up to now, spin/valley-dependent transport phenomena have been investigated mostly in two-dimensional nanostructures prepared by industry-incompatible methods (for example, mechanical exfoliation) or by cost-intensive instruments such as molecular-beam epitaxy[6,9,16]. In this work, we demonstrate the presence of easily accessible SOC in nanomaterials synthesized by colloidal chemistry. The solution-based synthesis of colloidal nanomaterials offers enormous opportunities in the production of inexpensive and high-quality crystals for electronic and, as we will show, spintronic devices[17–19]. Colloidal lead sulphide (PbS) nanosheets as continuous 2D crystals with promising properties do not suffer from tunnel barriers like other colloidal systems, such as thin films of nanoparticles[17,18,20]. However, their rock salt crystal structure is centrosymmetric. In order to break the inversion symmetry, we apply an electric field (gate) to the crystal as well as different boundaries underneath and above the PbS nanosheet (SiO_2 and vacuum)[6,21]. In combination with strong SOC, this suggests Rashba-type band splitting, which is confirmed by Kohn-Sham density functional theory (KS-DFT). In PbS nanosheets, the band splitting occurs in momentum space at the four M points. Upon illumination with circularly polarized light, the circular photo-galvanic effect (CPGE) leads to a net current that can be explained by an unconventional selection mechanism, depending on the spin orientation of the carriers. The observed effect is precisely tunable by changing the gate voltage or by changing the confinement (thickness of the sheets).

Results

Circular photo-galvanic measurements on the nanosheets. We synthesized PbS nanosheets with lateral dimensions of up to 5 μm and tunable thickness of 2–20 nm by introducing different amounts of oleic acid to the synthesis[19,20,22] (for crystallographic characterization see Supplementary Fig. 1). The height of the

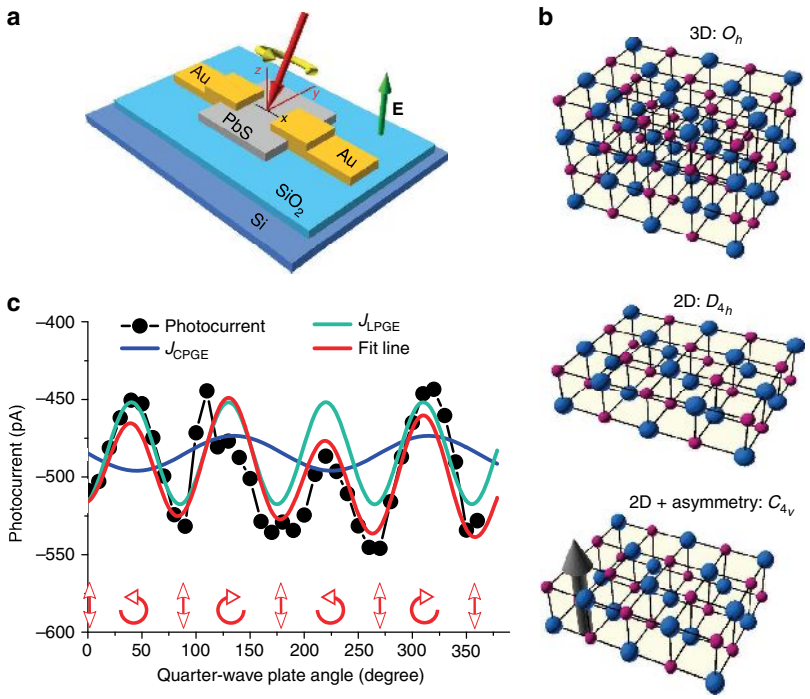

Figure 1 | Circular photo-galvanic effect in lead sulfide nanosheet devices. (**a**) Schematic image of the experimental setup. The semiconductor channel (PbS nanosheet, shown in grey) experiences an electric field and asymmetric interfaces (vacuum and SiO_2, shown in blue) and is illuminated with circularly polarized light. (**b**) Breaking the inversion symmetry in a PbS crystal. The symmetry is reduced from O_h point group (for the bulk crystal) to C_{4v} (2D crystal with external asymmetries). The blue and violet spheres represent lead and sulfur atoms respectively. The arrow shows the asymmetry in the crystal, including the gate electric field and the asymmetric interfaces. (**c**) Photocurrent at zero bias as a function of the quarter-wave plate angle (with a small non-zero incidence illumination angle). Fitting the results shows the existence of a non-zero CPGE current, suggested to originate from Rashba SOC in PbS nanosheets (LPGE: linear photo-galvanic effect). The arrows show the quarter-wave plate angles, in which the light is circularly or linearly polarized.

nanosheets directly determines the band gap of the material by confinement[23]. This tunability is of advantage for the performance of applications such as transistors, photodetectors and solar cells[17,18,20,23]. The synthesis of the nanosheets is independent of the fabrication of the devices, which makes it practical for industrial applications. The nanosheets were spin-coated on Si/SiO_2 substrates and contacted individually with Au electrodes by electron-beam lithography (see Supplementary Fig. 2). The contacts were placed in <110> direction of the crystal (corresponding to the M point direction in **k**-space) which is also the lateral growth direction of the nanosheets.

In order to evidence the possibility of spin manipulation in PbS nanosheets, we performed measurements on the CPGE as a function of light polarization[6,7,9–12]. For this purpose, photo-excited charge carriers with preferred spin orientation were prepared by illumination with circularly polarized light produced by a linearly polarized laser beam ($\lambda = 627$ nm) through a quarter-wave plate. The helicity of the exciting light was determined by the angle of the quarter-wave plate, which controls the spin orientation of the carriers. The beam was pointed to the sample obliquely in the yz plane (x is the direction of the current flow, z is normal to the nanosheet and y is perpendicular to these two).

Figure 1a schematically illustrates the experimental setup. This configuration provides the required inversion asymmetry (including the gate electric field and asymmetric vertical boundaries) in order to detect the CPGE. Bulk PbS with a rock salt crystal structure obeys the O_h point group symmetry which is inversion symmetric. By confining the material in z direction (height of the nanosheets), the symmetry is reduced first to the D_{4h} point group and then, by application of asymmetric vertical interfaces on top and underneath (SiO_2 and vacuum) as well as by the gate electric field, to C_{4v}. For this symmetry group, the inversion centre is absent, which supports the band splitting by SOC (Fig. 1b). Figure 1c depicts the variation of the photocurrent with changing the angle of the quarter-wave plate. It shows that illumination of the unbiased devices can yield a non-zero helicity-dependent photocurrent whose direction can be reversed by changing the light polarization from right-handed to left-handed, which is a sign for a spin-polarized current, generated as a consequence of spin injection into a spin–orbit coupled system[5,6,12]. In addition to that, other polarization-independent currents are detected which should be distinguished from the spin-related current.

The generated photocurrent is described by the expression

$$J_{\text{total}} = J_0 + J_{\text{CPGE}}\sin(2\varphi) + J_{\text{LPGE}}\sin(2\varphi)\cos(2\varphi) \qquad (1)$$

which can be employed for fitting the measurement results to determine the contribution of each effect[5,9–12,16]. In the equation, J_0 is the background current, resulting from, for example, photovoltaic effects, the Damber effect or hot electron injection. This component is independent of the helicity of the light. J_{LPGE} is the amplitude of the linear photo-galvanic effect which is due to asymmetric scattering of electrons along the conduction path. Although the LPGE is a function of the quarter-wave plate angle, it is equal for the right-handed and left-handed polarized light, which implies its independency from the helicity or respectively the spin orientation of the carriers. The oscillation period of the LPGE is equal to 90°. Eventually, J_{CPGE} is the amplitude of the CPGE, the current which is attributed to the population of the conduction band with spin-polarized charge carriers. In contrast to the LPGE, the CPGE oscillates with a period of 180°. It is maximum at a helicity of $+1$ (45° and 225°), minimum when the helicity is -1 (135° and 315°) and zero when the light is linearly polarized (0°, 90°, 180° and 270°) (refs 11,16).

Origin of the effect. Generally, different phenomena can lead to the existence of a CPGE in a 2D material, including Rashba/Dresselhaus SOC[5,6,9], orbital interactions[16], spin–valley coupling[11,12] or topological surface states[24]. Even in centrosymmetric materials with negligible SOC, in silicon or graphene for instance, this effect has been detected due to the asymmetry at the edges or contacts[16,25] (in-plane asymmetries). Lead sulphide as a crystal including high atomic-number Pb atoms ($Z(\text{Pb}) = 82$) can be considered as having strong SOC[15,26]. Further, the band structure of 2D PbS consists of a rectangular Brillouin zone with four equal valleys at the corners, the M points. By selectively exciting the carriers in each valley, a valley-polarized current might occur[11–13,15,27]. Such effects can be detected by the CPGE current since the angular momentum of

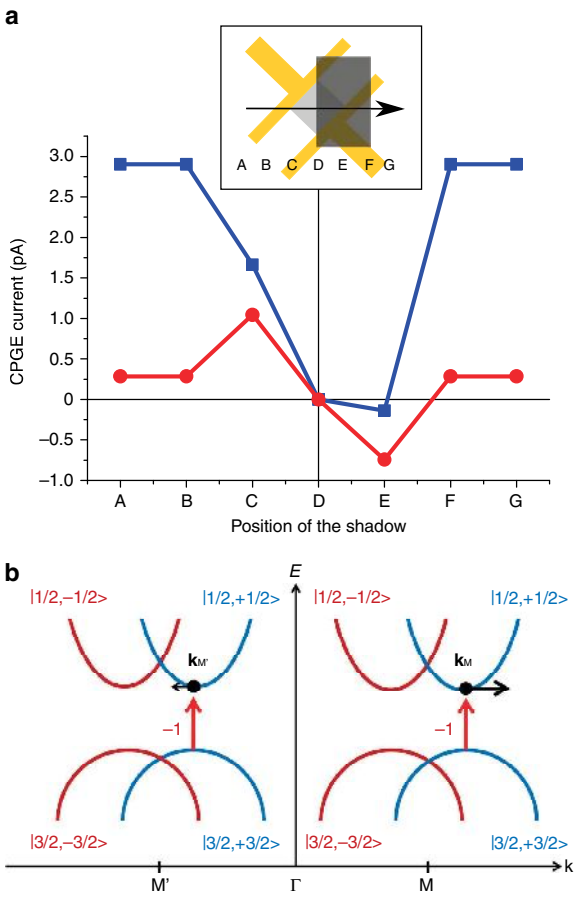

Figure 2 | Origin of the circular photo-galvanic effect in lead sulfide nanosheets. (**a**) The generated CPGE by shadowing different positions of the device, and with different illumination angles. The blue and the red lines represent the high and the low illumination angles respectively. The letters indicate the position of the centre of the shadow. The contribution of the vertical asymmetry and the enhanced in-plane asymmetry can be observed (I_{vertical} and $I_{\text{in-plane}}$). The inset is a schematic top view of the device to illustrate the position of the shadow during the experiment. In position D the whole device is covered, in C and E half of the device (I_{shadow}), and A, B, F, and G represent the full illumination of the device (I_{full}). (**b**) Illustration of the possible selection mechanism for exciting the carriers over the band gap. Illumination of the PbS crystal with circularly polarized light leads to transitions in both valleys but excitation of only one spin orientation. ($\mathbf{k}_{M,M'}$: momentum of the excited carriers in a valley). Here, the angular momentum of exciting photons is -1, which is added to the spin-angular momentum of electrons. The states are labeled as |J,M_J>.

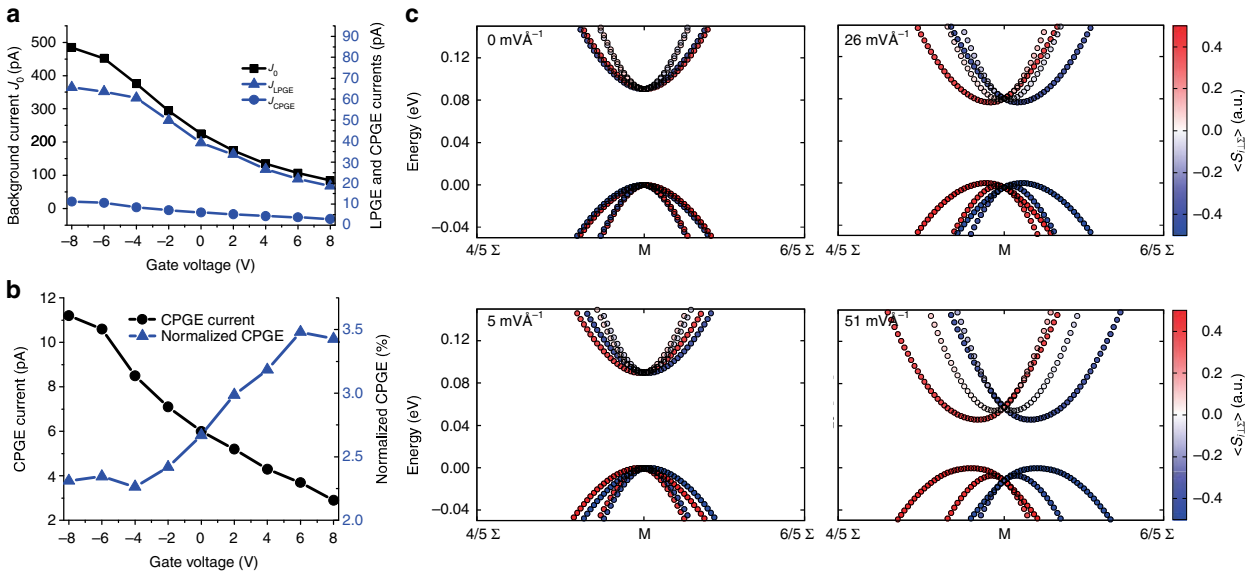

Figure 3 | Dependency of the effect on the back-gate voltage. (**a**) Dependence of different components of the photocurrent on the gate voltage. Similar gate dependencies can be observed for J_O, J_{LPGE} and J_{CPGE} (background current, linear photo-galvanic effect and circular photo-galvanic effect). (**b**) The measured CPGE current and its normalized value as a function of back-gate voltages for an 18 nm thick sheet. (**c**) Calculated (DFT) valence and conduction bands at the M point with application of different external electric fields—modelling the gate (15 layers). Σ denotes the path from Γ to M. The red and the blue colours denote the sign of the spin projection on the in-plane axis perpendicular to the Γ-M path ($<S_{i\perp\Sigma}>$).The valence-band maximum was set to 0 eV.

circularly polarized photons couples to the spin or valley index of the carriers, or leads to asymmetric scattering of the carriers. In any case, an inversion asymmetry must be present in the structure, which results in an asymmetric distribution of carriers in momentum space or asymmetric movement of the carriers in a certain direction. Therefore, a net CPGE current can be observed[5,6,9–12,16,25].

As the first step to explain the effect, we show that it mainly originates from the imposed vertical asymmetry to the crystal and not from the contacts/edges. For this purpose, we measured the CPGE current while we shadowed different parts of the device, to control the position of the beam and to intentionally enhance the asymmetry between the contacts/edges. Figure 2a shows the measured CPGE according to the position of the shadow. The measurements were done with a high incidence angle (about 15 degrees, the max. incidence angle due to the size of the view port of the vacuum chamber) and a lower one (around 6 degrees). By moving the shadow from one side of the device to the other one under the low incident angle, it is possible to reverse the direction of the in-plane asymmetry[12,16,24,25], expressed by a sign change of the shadowed CPGE current I_{shadow} (Fig. 2a, positions C and E). On the other hand, the function shows an offset which implies that a part of the current is independent of the in-plane asymmetry. In the following, this part will be shown to be the current originating from the vertical asymmetry ($I_{vertical}$), caused by the two interfaces and the gate. By increasing the incidence angle, firstly it can be observed that the unshadowed current (I_{full}) increases, which shows that the vertical asymmetry is an effective factor for generating I_{full}. In fact, to observe the CPGE based on in-plane asymmetry ($I_{in\text{-}plane}$), illumination should be perpendicular to the surface of the nanosheets. For a vertical asymmetry, such illumination leads to a zero CPGE current, and $I_{vertical}$ increases with increasing the incidence angle[6,12,16,24–26], which explains the increase of the measured I_{full} with the larger angle. When the shadow is applied, the imbalance of I_{shadow} (difference between the currents in positions C and E) becomes more pronounced with the higher illumination angle. It shows that $I_{vertical}$ has a larger part in I_{shadow}, while $I_{in\text{-}plane}$ is almost constant. By shadowing, we cover half of the device, which decreases the effective part of the crystal to generate $I_{vertical}$. In contrast, it leads to a higher $I_{in\text{-}plane}$, as we magnify the asymmetry. Since the share of $I_{vertical}$ is larger now, I_{shadow} becomes less than I_{full} (for the ideal contribution of $I_{vertical}$ and $I_{in\text{-}plane}$ see Supplementary Fig. 3). All of these observations prove that the vertical asymmetry is indeed able to generate a net CPGE current by changing the distribution of the carriers in the band structure, although they do not exclude the possibility of local in-plane asymmetries, such as contacts or edges.

Simulation of the band structure and the selection mechanism. In order to further investigate the origin of CPGE in PbS nanosheets, we calculated the band structure of clean PbS (001) slabs (with 15 atomic layers) including an external electric field using DFT based on the general-gradient approximation, employing the Perdew–Burke–Ernzerhof (PBE) exchange-correlation functional[28] (see Supplementary Fig. 4). SOC was taken into account by using fully relativistic projector-augmented-wave (PAW) potentials. It should be pointed out that when SOC is considered, general-gradient approximation functionals are known to underestimate the band gap in bulk PbS and even predict a band inversion[29,30]. The usage of hybrid functionals (for example, Heyd–Scuseria–Ernzerhof) or many-body corrections like the GW approximation were shown to improve the agreement with experimental band gaps, but they are much more computationally demanding than pure DFT[29,30]. The qualitative trend of the influence of an external electric field on the band structure is expected to be described well enough by PBE to get reliable results, as this functional was already used to describe Rashba systems[31–33].

Without an external electric field, inversion symmetry is maintained, and no Rashba spin splitting can be observed along

the Γ–M–X path (see Supplementary Fig. 5a). At the band gap (M point), the two highest filled bands split in direction of the Γ point. Adding an external electric field along the surface normal breaks the inversion symmetry, and Rashba spin splitting occurs at the M point (see Supplementary Fig. 5b), which is confirmed by a spin texture typical for the Rashba effect (see Supplementary Fig. 5c). The Rashba spin splitting of the highest filled band differs from the splitting of the second highest filled band. Rashba spin splitting can be also observed for the conduction band.

The calculated band structure implies that by exciting the material with right-handed (left-handed) polarized light, that is photons with angular momentum of $+1$ (-1), some of the possible transitions between the valence and conduction bands are forbidden since energy and angular momentum must be conserved during the transition. The possible excitation mechanism of the carriers over the band gap is illustrated schematically in Fig. 2b. The bands are split around the M point. However, in contrast to other multi-valley materials, the splitting occurs in momentum space and the split bands, corresponding to the two opposite spin orientations, have equal energies. For materials with rectangular Brillouin zone, both valleys (M and M′) represent similar orbital characters. Therefore, they are not selectively populated by adjusting the angular momentum of the exciting photons (which is done by selecting the handedness of the circular polarization)[27]. On the other hand, by splitting the bands in momentum space, the angular momentum of the split bands becomes different for each spin. As it can be observed in Supplementary Fig. 6, total angular momentum of the valence band and the conduction band are respectively 3/2 and 1/2 with spin-angular momentum of 1/2 (ref. 34). By controlling the helicity of the exciting light, carriers can be selectively excited based on their spin orientation[12,14,26]. Upon illumination with circularly polarized light and population of the conduction band with spin-polarized electrons, the number of excited carriers is equal in the M valley and in the M′ valley, but the linear momentum differs, since splitting is asymmetric at these two points. For instance, the spin-up band is shifted away from the Gamma point (to higher momentum) at the M point, but towards the Gamma point (to lower momentum) at M′. Therefore, spin-up electrons at the M point have higher momentum compared to those at the M′ point. This results in the generation of the spin-polarized CPGE current based on Rashba SOC which splits the valleys of the band structure.

The current generated by the CPGE in the direction of a specific crystal orientation (λ) can be expressed by

$$J_{\mathrm{CPGE}-\lambda} = \sum_{\mu} \chi_{\lambda\mu} e_{\mu} E_0^2 P_{\mathrm{circ}}, \qquad (2)$$

where μ is one of the different crystal orientations (x, y, z), χ is the CPGE second-rank pseudo tensor which is directly affected by the crystal asymmetry, $\mathbf{E}_0$ is the electric field (complex amplitude) of the light wave, P_{circ} is the helicity of the circularly polarized light (degree of polarization), $\mathbf{e}=\mathbf{q}/q$ is the unit vector for the light propagation, and $\mathbf{q}$ is the wave vector of the light in the medium[5,6,9]. For the C_{4v} point group, the pseudo tensor χ has non-zero elements, which results in a non-zero CPGE current[35,36].

Gate dependency of the effect. Having introduced confinement and symmetry breaking by the gate electric field as the factors influencing the SOC, we separately studied these elements under the low illumination angle in order to tune the band splitting in the PbS nanosheets. Figure 3 shows the dependence of the CPGE current on the gate voltage (see also Supplementary Fig. 7). Changing the gate voltage can influence the photocurrent in two ways: First, it affects the band splitting by modification of the inversion asymmetry[5,6,12]. Second, the band alignment of the material with the contact metals is altered, which results in changing the extraction probability and the recombination rate of all the excited carriers including the spin-polarized ones[37–39]. The former is observable only for the CPGE current, whereas the latter is a general effect and can govern all three components of the photocurrent (J_0, J_{CPGE}, J_{LPGE}). As a result, comparable responses to the gate can be observed for these components (Fig. 3a). In order to extract the pure gate dependence of SOC, the change in the band alignment or any other spin-independent effect should be excluded from the results. This can be done by normalizing the CPGE current by the background current[6,9,16]. The normalized value represents the internal tunability of the band splitting by the gate voltage.

As shown in Fig. 3b, by sweeping the back-gate voltage from -8 to 8 V, the CPGE current of the nanosheets changes significantly. The gate dependency of the normalized CPGE current also shows the clear tunability of the band splitting by the gate electric field. By changing the electric field in the

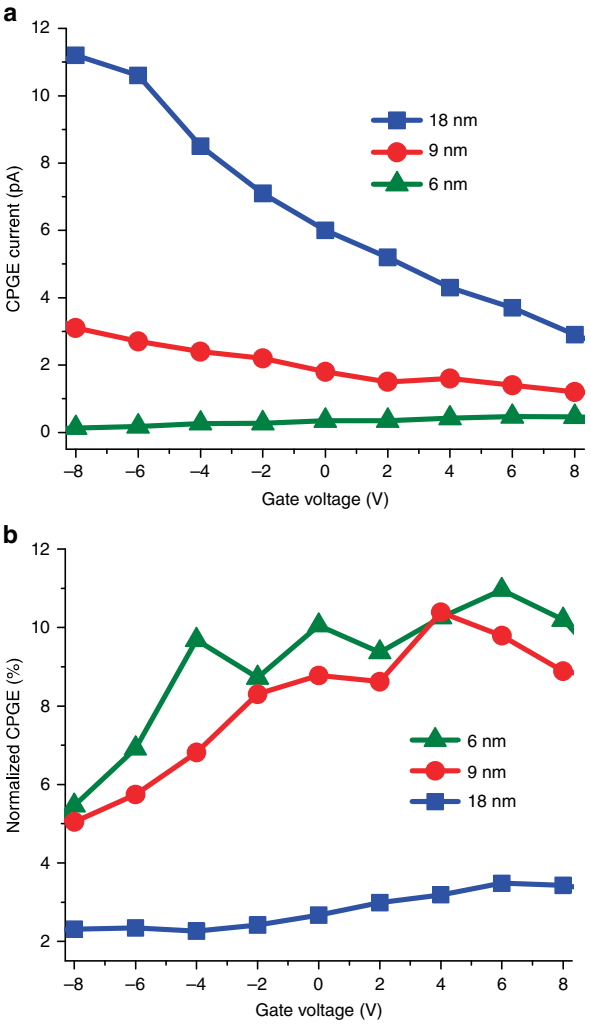

Figure 4 | Circular photo-galvanic current for different thicknesses. (**a**) The CPGE current for 6, 9 and 18 nm thick sheets, measured as a function of the gate voltage. (**b**) CPGE current normalized by the background current, as a function of the gate voltage. Thinner sheets show higher gate dependencies.

semiconductor channel, resulting from the back gate, the potential profile of the confined crystal can be modulated[6], resulting in the modulation of the degree of reduction in symmetry. As a result, by increasing the gate voltage, a larger band splitting can be expected[12], which causes a wider distribution of the carriers in momentum space and hence a higher CPGE current is generated. The DFT band structure calculations show that the strength of the gate electric field can modify the Rashba splitting of the valence and conduction bands (Fig. 3c). The gate effect is superimposed on the boundary conditions resulting from the asymmetric interfaces. Therefore, even at zero gate voltage, a CPGE current is generated (Fig. 3b). Dependency on the gate voltage is another confirmation that the vertical asymmetry is effective in the CPGE, since the vertical electric field is not expected to affect the in-plane asymmetry.

Thickness dependency of the effect. Moreover, we performed the CPGE measurements on devices based on nanosheets with three different thicknesses of 6, 9, and 18 nm to investigate the influence of the quantum confinement on the Rashba effect (Fig. 4a and Supplementary Fig. 8). By sweeping the gate voltage, it can be seen that thicker sheets produce higher CPGE currents. The character of the gate dependency for the CPGE current is similar to the background current for all devices. Since the channel dimensions (thickness and width) are different for each sample, the absorption capability of the devices is different as well. In order to make the results comparable, the CPGE normalized by the background current was calculated (Fig. 4b). The measurements indicate that by decreasing the thickness of the sheets, which corresponds to an increase of the confinement effect, structural inversion asymmetry and consequently the Rashba SOC becomes more pronounced in PbS nanosheets. Despite the different gate dependencies of the CPGE currents, all thicknesses of nanosheets show comparable gateabilities for the normalized CPGE. To clearly see the effect of the thickness on the vertical asymmetry, tunability of the normalized CPGE with the gate voltage can be observed, which is only a character of the band splitting due to the vertical asymmetry and excludes the effects of any in-plane asymmetry. As shown in Fig. 4b, the thinner the nanosheet, the more effective is the gate voltage. By sweeping the back-gate voltage from -8 to 8 V, the normalized CPGE for the 6 nm sheets changes six times more than that for the 18 nm sheets. The gate voltage and the asymmetric boundaries result in an electric field in the crystal which breaks the symmetry. The thinner the nanosheets the stronger is the effective field. By increasing the effective electric field in the crystal, splitting becomes larger, and a stronger CPGE can be detected.

Discussion

A CPGE has been observed in colloidal PbS nanosheets, which could be assigned to Rashba SOC. The inversion symmetry in the rock salt crystal of bulk PbS was broken by quantum confinement, by asymmetric interfaces on two sides of the material, and by a gate electric field. The effect of these parameters was investigated experimentally, and the results were substantiated by DFT simulations of the band structure. The latter shows a splitting of the bands in momentum space, which results in an unconventional selection mechanism based on the spin of the photo-excited carriers. Our results are consistent with a higher Rashba SOC in thinner sheets. The observation of spin-related electrical transport phenomena in colloidal materials is promising in terms of future industrial applications, which supports the recently emerging spintronic approaches with simplicity, inexpensiveness and scalability of the colloidal synthesis of nanomaterials.

Methods

Synthesis. All chemicals were used as received: lead(II) acetate tri-hydrate (Aldrich, 99.999%), thioacetamide (Sigma-Aldrich, $\geqslant$99.0%), diphenyl ether (Aldrich, 99% +), dimethyl formamide (Sigma-Aldrich, 99.8% anhydrous), oleic acid (Aldrich, 90%), trioctylphosphine (ABCR, 97%), 1,1,2-trichloroethane (Aldrich, 96%). In a typical synthesis, a three neck 50 ml flask was used with a condenser, septum and thermocouple. 806 mg of lead acetate trihydrate (2.3 mmol) was dissolved in 10 ml of diphenyl ether. Depending on the targeted thickness, 2–10 ml of OA (5.7–28 mmol) was added. The mixture was heated to 75 °C until the solution turned clear. Then, vacuum was applied for 3.5 h to transform lead acetate into lead oleate and to remove acetic acid in the same step. The solution was heated under nitrogen flow to the desired reaction temperature of 130 °C, while at 100 °C, 0.7 ml of TCE (7.5 mmol) was added under reflux to the solution and the time has been started. After 12 min 0.23 ml of 0.04 g TAA (0.5 mmol) in 6.5 ml DMF was added to the reaction solution. After 5 min, the heat source was removed and the solution was let to cool down below 60 °C which took approximately 30 min and afterwards, centrifuged at 4,000 rpm for 3 min. The precipitant was washed two times in toluene before the nanosheets were finally suspended in toluene again for storage.

Device preparation. PbS nanosheets with lateral dimensions of up to 5 µm suspended in toluene were spin-coated on silicon wafers with 300 nm thermal silicon oxide as the gate dielectric. The highly doped silicon was used as the back gate. The individual nanosheets were contacted by e-beam lithography followed by thermal evaporation of Ti/Au (1/40 nm) and lift-off.

Measurements. Immediately after device fabrication, we transferred the samples to a probe station (Lakeshore-Desert) connected to a semiconductor parameter analyser (Agilent B1500a). All the measurements have been performed in vacuum at room temperature. The vacuum chamber had a view port above the sample which is used for sample illumination. For illumination of the nanosheets, an 18 mW red laser (627 nm) with a spot size of 4 mm was used. The laser was able to excite the electrons over the band gap, while its energy was not enough for excitations to higher levels of the conduction band[40]. The polarization of the laser beam was controlled by a polarization filter and a quarter-wave plate.

Density functional theory simulations. Density functional theory calculations were done by employing the electronic structure code Quantum Espresso 5.2.1 (ref. 41) in combination with the PBE exchange-correlation functional[28] and the PAW method. Relativistic effects (scalar- and spin–orbit coupling) were considered through the PAW potentials (Valence configuration: Pb: $5d^{10}6s^26p^2$; S: $3s^23p^4$) self-consistently (the used PAW potentials for lead and sulphur were taken from the pslibrary.1.0.0 downloadable at: http://www.qe-forge.org/gf/project/pslibrary/frs). A kinetic-energy cut-off for the wavefunction of 46 Ry and a kinetic-energy cut-off of the electronic density of 460 Ry were used. The Brillouin zone was sampled with a shifted $8 \times 8 \times 8$ grid for bulk PbS and a shifted $8 \times 8 \times 1$ mesh for two-dimensional (001)-PbS sheets. The default convergence thresholds were used for all calculations.

The atomic positions in the slab were allowed to relax, while the lattice constant was kept fixed at the value calculated for bulk PbS using the same computational settings (6.002 Å). SOC and dispersion interactions were not considered during the relaxation. The slabs were separated by a vacuum of 15 Å.

Band-structure calculations were carried out on those optimized structures considering SOC. External electric fields were simulated with a saw-like potential, changing along the surface normal. A larger vacuum layer (20 Å) was used, and the decrease of the saw-like potential to its initial value was set to be in the middle of the vacuum. Symmetry was not used to reduce the number of **k** points during the self-consistent field calculation.

The projected density of states resolved on the band structure was calculated using a Gaussian smearing with a broadening of 0.0001 Ry. The projected density of states was summed over all atoms for any type of orbital.

Data availability. All the theoretical and experimental data supporting this study are available from the corresponding author.

References

1. Normile, D. The end—not here yet, but coming soon. *Science* **293,** 787 (2001).
2. Mack, C. A. in *Proc. SPIE 5037, Emerging Lithographic Technologies VII* (ed. Engelstad, R. L.) Vol. 5037, 1 (Society of Photo-Optical Instrumentation Engineers).
3. Waldrop, M. M. More than Moore. *Nature* **530,** 144–147 (2016).
4. Zeng, H., Dai, J., Yao, W., Xiao, D. & Cui, X. Valley polarization in MoS_2 monolayers by optical pumping. *Nat. Nanotech.* **7,** 490–493 (2012).
5. Zhang, S. *et al.* Generation of Rashba spin–orbit coupling in CdSe nanowire by ionic liquid gate. *Nano Lett.* **15,** 1152–1157 (2015).
6. Yin, C. *et al.* Tunable surface electron spin splitting with electric double-layer transistors based on InN. *Nano Lett.* **13,** 2024–2029 (2013).

7. Kohda, M. *et al.* Gate-controlled persistent spin helix state in (In,Ga) as quantum wells. *Phys. Rev. B* **86,** 081306 (2012).
8. Datta, S. & Das, B. Electronic analog of the electro-optic modulator. *Appl. Phys. Lett.* **56,** 665 (1990).
9. Zhang, Q. *et al.* Strong circular photogalvanic effect in ZnO epitaxial films. *Appl. Phys. Lett.* **97,** 041907 (2010).
10. He, X. W. *et al.* Circular photogalvanic effect of the two-dimensional electron gas in Al x Ga 1 − x N/GaN heterostructures under uniaxial strain. *Appl. Phys. Lett.* **91,** 071912 (2007).
11. Eginligil, M. *et al.* Dichroic spin–valley photocurrent in monolayer molybdenum disulphide. *Nat. Commun.* **6,** 7636 (2015).
12. Yuan, H. *et al.* Generation and electric control of spin–valley coupled circular photogalvanic current in WSe_2. *Nat. Nanotech.* **9,** 851–857 (2014).
13. Mak, K. F., He, K., Shan, J. & Heinz, T. F. Control of valley polarization in monolayer MoS_2 by optical helicity. *Nat. Nanotech.* **7,** 494–498 (2012).
14. Yao, W., Xiao, D. & Niu, Q. Valley-dependent optoelectronics from inversion symmetry breaking. *Phys. Rev. B* **77,** 235406 (2008).
15. Xiao, D., Liu, G., Feng, W., Xu, X. & Yao, W. Coupled spin and valley physics in monolayers of MoS_2 and other group-VI dichalcogenides. *Phys. Rev. Lett.* **108,** 196802 (2012).
16. Dhara, S., Mele, E. J. & Agarwal, R. Voltage-tunable circular photogalvanic effect in silicon nanowires. *Science* **349,** 726–729 (2015).
17. Dogan, S., Bielewicz, T., Cai, Y. & Klinke, C. Field-effect transistors made of individual colloidal PbS nanosheets. *Appl. Phys. Lett.* **101,** 073102 (2012).
18. Dogan, S., Bielewicz, T., Lebedeva, V. & Klinke, C. Photovoltaic effect in individual asymmetrically contacted lead sulfide nanosheets. *Nanoscale* **7,** 4875–4883 (2015).
19. Bielewicz, T. *et al.* From dots to stripes to sheets: shape control of lead sulfide nanostructures. *Chem. Mater.* **27,** 8248–8254 (2015).
20. Bielewicz, T., Dogan, S. & Klinke, C. Tailoring the height of ultrathin PbS nanosheets and their application as field-effect transistors. *Small* **11,** 826–833 (2014).
21. Wu, S. *et al.* Electrical tuning of valley magnetic moment through symmetry control in bilayer MoS_2. *Nat. Phys.* **9,** 149–153 (2013).
22. Schliehe, C. *et al.* Ultrathin PbS sheets by two-dimensional oriented attachment. *Science* **329,** 550–553 (2010).
23. Aerts, M. *et al.* Highly efficient carrier multiplication in PbS nanosheets. *Nat. Commun.* **5,** 3789 (2014).
24. McIver, J., Hsieh, W., Steinberg, D., Jarillo-Herrero, H. & Gedik, P. N., Control over topological insulator photocurrents with light polarization. *Nat. Nanotech.* **7,** 96–100 (2012).
25. Karch, J. *et al.* Terahertz radiation driven chiral edge currents in graphene. *Phys. Rev. Lett.* **107,** 276601 (2011).
26. Dyakonov, M. I. (ed. *Spin Physics in Semiconductors, vol. 157 of Springer Series in Solid-State Sciences* (Springer-Verlag, 2008).
27. Rodin, A. S., Gomes, L. C., Carvalho, A. & Castro Neto, A. H. Valley physics in tin (II) sulfide. *Phys. Rev. B* **93,** 045431 (2016).
28. Perdew, J. P., Burke, K. & Ernzerhof, M. Generalized gradient approximation made simple. *Phys. Rev. Lett.* **77,** 3865–3868 (1996).
29. Svane, A. *et al.* Quasiparticle self-consistent GW calculations for PbS, PbSe, and PbTe: Band structure and pressure coefficients. *Phys. Rev. B* **81,** 245120 (2010).
30. Hummer, K., Grüneis, A. & Kresse, G. Structural and electronic properties of lead chalcogenides from first principles. *Phys. Rev. B* **75,** 195211 (2007).
31. Ma, Y., Dai, Y., Yin, N., Jing, T. & Huang, B. Ideal two-dimensional systems with a gain Rashba-type spin splitting: SrFBiS2 and BiOBiS2 nanosheets. *J. Mater. Chem. C* **2,** 8539–8545 (2014).
32. Eremeev, S. V., Tsirkin, S. S., Nechaev, I. A., Echenique, P. M. & Chulkov, E. V. New generation of two-dimensional spintronic systems realized by coupling of Rashba and Dirac fermions. *Sci. Rep.* **5,** 12819 (2015).
33. Shanavas, K. V. & Satpathy, S. Electric field tuning of the Rashba effect in the polar perovskite structures. *Phys. Rev. Lett.* **112,** 086802 (2014).
34. Liu, J., Qian, X. & Fu, L. Crystal field effect induced topological crystalline insulators in monolayer IV–VI semiconductors. *Nano Lett.* **15,** 2657–2661 (2015).
35. Ganichev, S. D. & Golub, L. E. Interplay of Rashba/Dresselhaus spin splittings probed by photogalvanic spectroscopy—a review. *Phys. Status Solidi B* **251,** 1801–1823 (2014).
36. Vajna, S. z. *et al.* Higher-order contributions to the Rashba-Bychkov effect with application to the Bi/Ag(111) surface alloy. *Phys. Rev. B* **85,** 075404 (2012).
37. Vélez, S. *et al.* Gate-tunable diode and photovoltaic effect in an organic–2D layered material p–n junction. *Nanoscale* **7,** 15442–15449 (2015).
38. Hong, T. *et al.* Polarized photocurrent response in black phosphorus field-effect transistors. *Nanoscale* **6,** 8978–8983 (2014).
39. Chen, C., Zhang, W., Kong, E. S. & Zhang, Y. Carbon nanotube photovoltaic device with asymmetrical contacts. *Appl. Phys. Lett.* **94,** 263501 (2009).
40. Herman, F., Kortum, R., Ortenburger, I. & Van Dyke, J. P. Relativistic band structure of GeTe, SnTe, PbTe, PbSe, and PbS. *J. Phys. Colloques* **29,** C4-62–C4-77 (1968).
41. Giannozzi, P. *et al.* QUANTUM ESPRESSO: a modular and open-source software project for quantumsimulations of materials. *J. Phys. Condens. Matter* **21,** 395502–395520 (2009).

Acknowledgements

M.M.R.M., T.B. and C.K. gratefully acknowledge financial support of the European Research Council via the ERC Starting Grant '2D-SYNETRA' (Seventh Framework Program FP7, Project: 304980). C.K. thanks the German Research Foundation DFG for financial support in the frame of the Cluster of Excellence 'Center of ultrafast imaging CUI' and the Heisenberg scholarship KL 1453/9-2. M.S.Z. and C.H. thank the DFG for funding via the project SFB668 (project B17) and the North-German Supercomputing Alliance (HLRN) for computational resources. The authors thank Vladimiro Mujica (Arizona State University) for discussion and Sascha Kull for support in the synthesis of the nanosheets.

Author contributions

M.M.R.M. and C.K. conceived the main concepts. M.M.R.M. designed the experiments, prepared the samples and performed the electrical measurements. T.B. performed the nanosheets synthesis and characterization. M.S.Z. and C.H. performed the simulations and theoretical analysis of the results. M.M.R.M., T.B., M.S.Z., C.H. and C.K. wrote the manuscript.

Additional information

Supplementary Information accompanies this paper at http://www.nature.com/naturecommunications

Competing interests: The authors declare no competing financial interests.

Reprints and permission information is available online at http://npg.nature.com/reprintsandpermissions/

How to cite this article: Ramin Moayed, M. M. *et al.* Towards colloidal spintronics through Rashba spin-orbit interaction in lead sulphide nanosheets. *Nat. Commun.* **8**, 15721 doi: 10.1038/ncomms15721 (2017).

Publisher's note: Springer Nature remains neutral with regard to jurisdictional claims in published maps and institutional affiliations.

Open Access This article is licensed under a Creative Commons Attribution 4.0 International License, which permits use, sharing, adaptation, distribution and reproduction in any medium or format, as long as you give appropriate credit to the original author(s) and the source, provide a link to the Creative Commons license, and indicate if changes were made. The images or other third party material in this article are included in the article's Creative Commons license, unless indicated otherwise in a credit line to the material. If material is not included in the article's Creative Commons license and your intended use is not permitted by statutory regulation or exceeds the permitted use, you will need to obtain permission directly from the copyright holder. To view a copy of this license, visit http://creativecommons.org/licenses/by/4.0/

© The Author(s) 2017

3-7 Unpublished Project: Tuning the electrical properties of PbS nanowires by sculpting the crystal

The following section summarizes the results of the measurements on the electrical properties of metallic PbS nanowires. My contribution to this part was fabricating the devices based on the synthesized PbS wires, performing the electrical measurements, and the analysis and interpretation of the results. This part of the project has been carried out by: Mohammad Mehdi Ramin Moayed, Sascha Kull, Angelique Rieckmann, Philip Beck, Michael Wagstaffe, Heshmat Noei, Andreas Kornowski, Rostyslav Lesyuk, Andreas Stierle, and Christian Klinke.

Recently, the size reduction of different materials has led to the emergence of many novel properties due to the employment of quantum confinement[98]. For instance, the realization of spin-dependent phenomena[97], unconventional superconductivity regimes[99], and topological surface states[100] attracted considerable attention. Nevertheless, there is still room to further tune the shape and size of nanomaterials, which might further modify their properties or even fundamentally change their character[41,101]. In this respect, the colloidal synthesis of nanomaterials could play a crucial role, since it shows a great degree of flexibility in tuning the product. Further, it is cheap, fast, and scalable, which makes it suitable for commercial applications[37,102].

Up to now, the application of PbS has been limited to semiconductor based components such as photodetectors[103], field-effect transistors[49], and solar cells[50,104]. Considering the previously discussed advantages of this material, expanding its application beyond the limits of semiconductors would be of great interest (for applications such as flexible electrodes or interconnects[105,106]). For this purpose, a fundamental alteration of the electrical properties is required.

Here, a method is introduced to change the electrical properties of quasi-1D colloidal lead sulphide wires from normal semiconducting to metallic. This could be done by altering the surface facet of the crystal to the {111} facet, or in other words, by cutting the crystal through this facet. As discussed in section 1-2-1, this facet is a single element facet. Therefore, it forms a Pb rich metallic shell around the wires and makes them metallic, in contrast to other forms of PbS nanocrystals which are all semiconducting. Altering the surface facet is done by transforming the building blocks (cubes) to small octahedra during the early stages of the

synthesis. The formed wires by the attachment of these octahedra would have a zigzag shape, as shown in Fig. 5.

The zigzag wires, which are used in this work, are synthesized together with another form of wires, which have a straight shape. These straight wires are synthesized by the attachment of cubes (polyhedra) and therefore, their surface contains Pb and S. Comparable to the PbS nanosheets, they show semiconducting behavior. By altering the synthesis conditions, especially the ligands combination, it is possible to produce dominantly metallic wires, semiconducting ones, or even both of them together.

Here, metallic behavior of the zigzag wires is theoretically predicted by density-functional theory (DFT) calculations and experimentally confirmed by various transport measurements, including field-effect, photoconductivity, and the temperature dependency (of the conductivity) measurements. The outcome of these experiments introduces new applications for PbS, including flexible electrodes. In addition, it helps to better understand the previously studied PbS based systems.

Synthesis and crystallography

Two types of PbS nanowires (straight and zigzag) with the length of more than 10 µm and the diameter of 30-50 nm have been synthesized based on the receipt presented in part A2 of the appendix. Although these wires are the products of a single synthesis, their crystals have important differences. As can be observed in Fig. 25a, the first distinction is their shape. While one type has a smooth and flat surface (Fig. 25b), the other type grows in a zigzag form and therefore, its surface is rough (Fig. 25c). Small octahedra are the byproduct of this synthesis (Fig. 25a).

The difference in the shape of these wires could be a sign for different growth mechanisms. Therefore, the samples have been investigated with the high resolution TEM to gain more details about them.

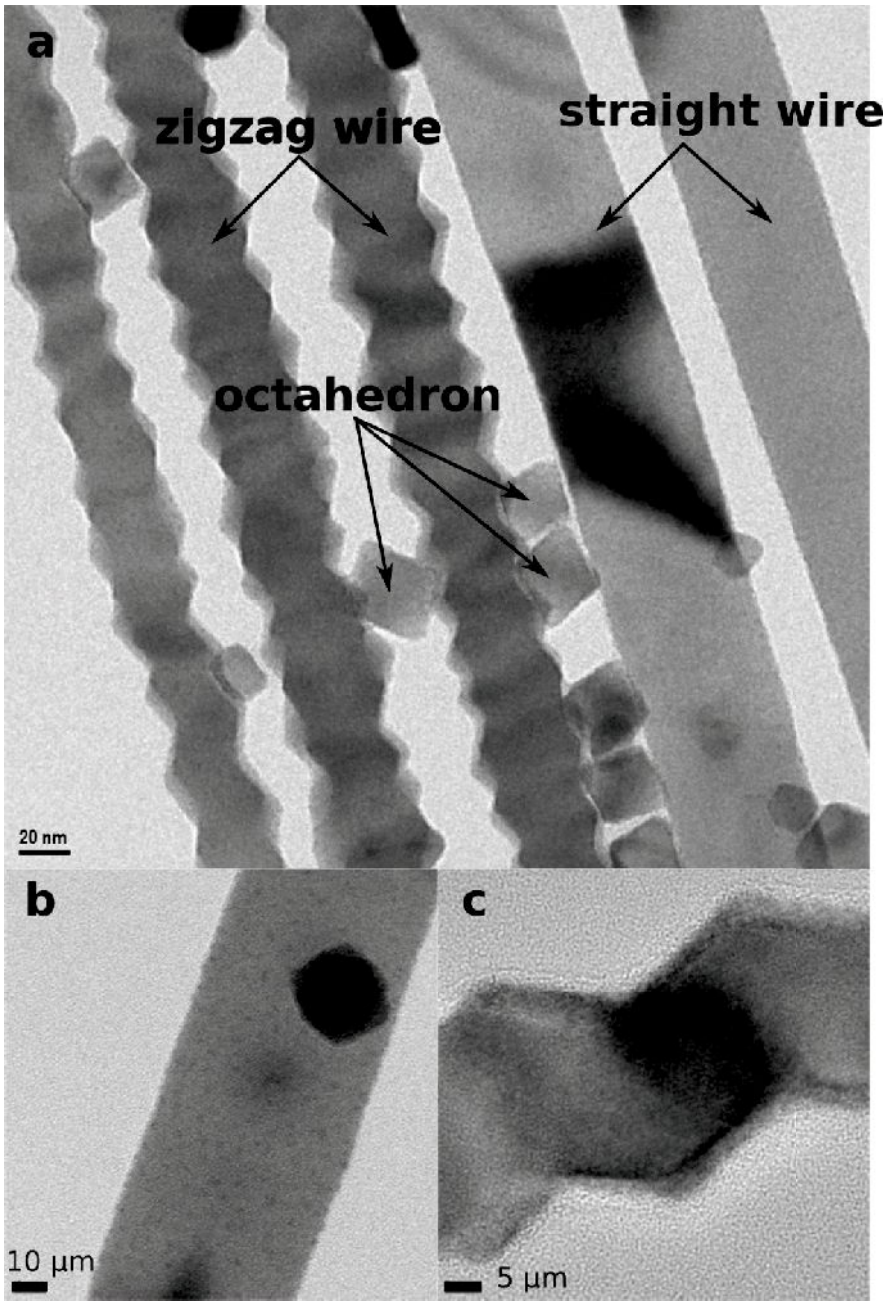

Figure 25. TEM images of the PbS nanowires, grown in two different forms. (a) Two types of nanowires are observable: straight ones and zigzag ones. In addition, small octahedra are also present. (b) The first type grows in a straight form and has a flat surface. (c) The second type has a zigzag form and therefore, a rough surface.

Figure 26a shows the HRTEM of the straight wires. First of all, it shows that their growth direction is (112). This is in agreement with the growth direction of similar straight wires, discussed in the literature[57]. Further, their top facet which is observed in the TEM images is the {111} facet. On the other hand, the HRTEM images of the zigzag wires (Fig. 26b) shows

that their growth direction is (100). With the TEM, these wires are observed through the {110} facet (the top facet). These observations are also in agreement with the literature[55-57,107-109]. It should be also mentioned that the atomic arrays on the surface of the zigzag wires form an angle of 109 deg (Fig. 26c).

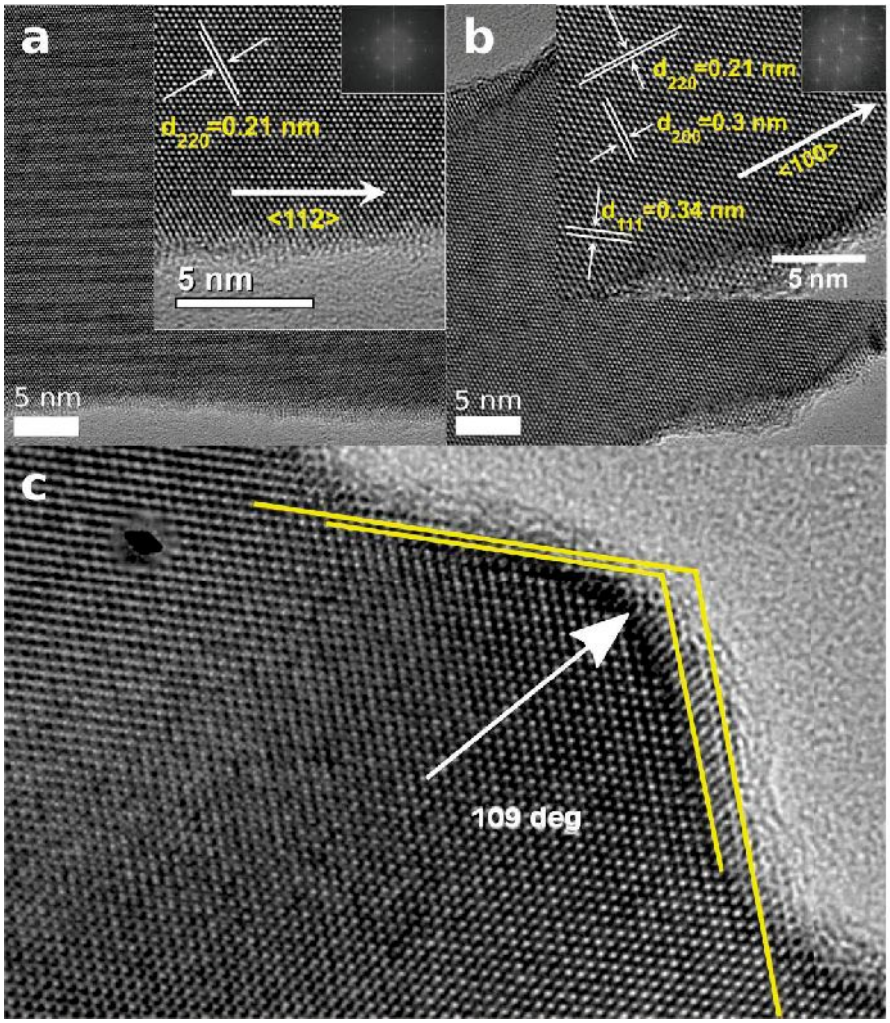

Figure 26. HRTEM images of the wires. (a) HRTEM image of the straight wires. Inset: enlarged fragment of the surface with the (220) spacing. The growth direction is indexed as (112). Inset top: fast Fourier transform electron diffraction patterns (zone axis <111>) confirming the {111} top facet and the specified growth direction. (b) HRTEM image of the zigzag wires. Inset: enlarged fragment of the surface with the (200), (220), and (111) spacing. The direction of the growth was defined as (100). Inset top: fast Fourier transform electron diffraction patterns (zone axis <110>), showing the {110} facet as the top facet. (c) The angle between the atomic arrays at the surface of the zigzag wires is equal to 109 deg.

Based on these observations, the growth mechanism of these wires could be compared with the suggested models in the literature, which were already discussed in detail in the theory part. During the formation of the straight wires, first small cubes (or polyhedra) are formed. Then, they are attached through the {112} facets and create the wires in the (112) direction. In this situation, the top facet of the wires could be the {111} facet, which is also observable in the HRTEM images. The growth of the straight wires is schematically shown in Fig. 27a. Since the building blocks of these wires are comparable with the normal nanosheets, their electrical properties are also similar (semiconducting)[53,57].

On the other hand, the zigzag wires are made by the attachment of octahedra. These octahedra are attached through the {100} facet (tip to tip) and form zigzag wires in the (100) direction[55-57,107-109]. This type of attachment is shown in Fig. 27b. As can be seen, the top facet of these wires must be the {110} face (in agreement with the HRTEM images), since this is the only stable way for them to lie on the TEM grid. Under this condition, the surface atomic arrays must be observed with the angle of 109 deg, which is also true for the synthesized zigzag wires. The existence of octahedra next to the zigzag wires (observable in the TEM images) is another sign that these wires are made of octahedra (Fig. 25a).

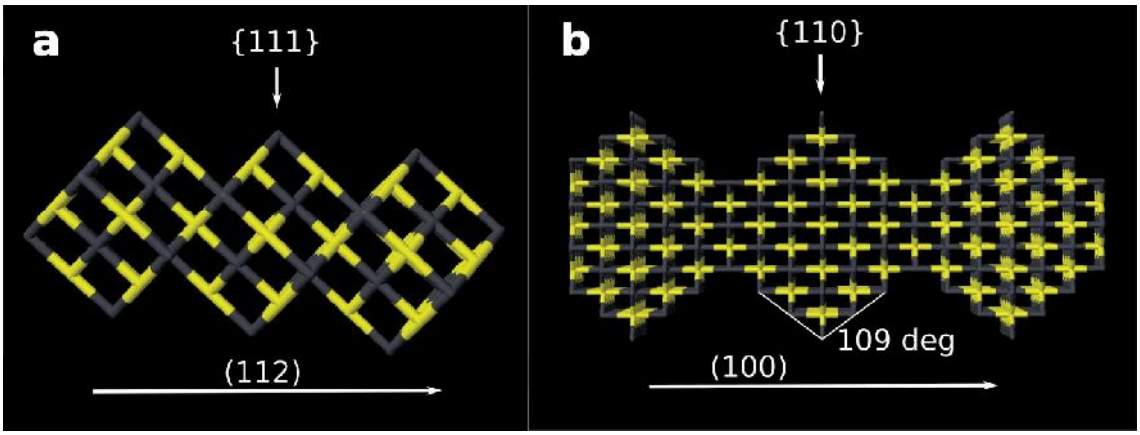

Figure 27. Growth mechanism of different types of wires. (a) The straight wires grow in the (112) direction by the attachment of cubes through the {112} facet. Their top facet is the {111} facet. (b) The zigzag wires with the growth direction of (100) are made of octahedra which are attached through the {100} facet. Their top facet is the {110} facet and their tips are observed with the angle of 109 deg.

Due to the extremely high Pb/S ratio in the synthesis, and also due to the high reactivity of the S rich {111} facets[110,111], the surface of the zigzag wires is only composed of the Pb rich {111} facets, as can be seen in Fig, 28.

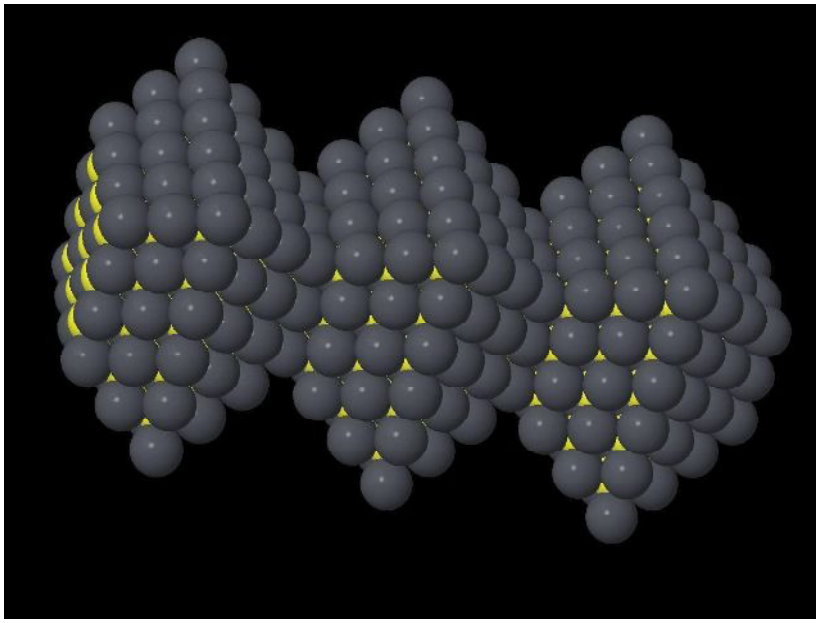

Figure 28. Formation of the zigzag wires. The surface of these wires is only composed of Pb atoms, which are shown here as gray spheres (the yellow spheres represent the S atoms).

DFT calculations

After identifying the building blocks of the wires, their electrical properties can be predicted by DFT calculations. For this purpose, the band structure of the PbS crystal was calculated, once by cutting the crystal through the {100} facet (similar to the cubes) and once by cutting through the {111} facet (representing the octahedra).

As can be seen in Fig. 29a, while the former shows the normal band structure of PbS, similar to the bulk material, the latter shows an overlap between the valence band and the conduction band (Fig. 29b). Calculating the density of states (DOS) of these crystals also shows that the DOS is zero in the bandgap of the former (Fig. 29c). In contrast, it is constantly non-zero when the crystal is cut through the {111} facet (Fig. 29d). The conclusion of these calculations, which are in agreement with the previously reported works[111-113], is that the crystal with the {100} cut (the straight wires) must represent normal semiconducting behavior of PbS but with the {111} cut (the zigzag wires), it must have a metallic character.

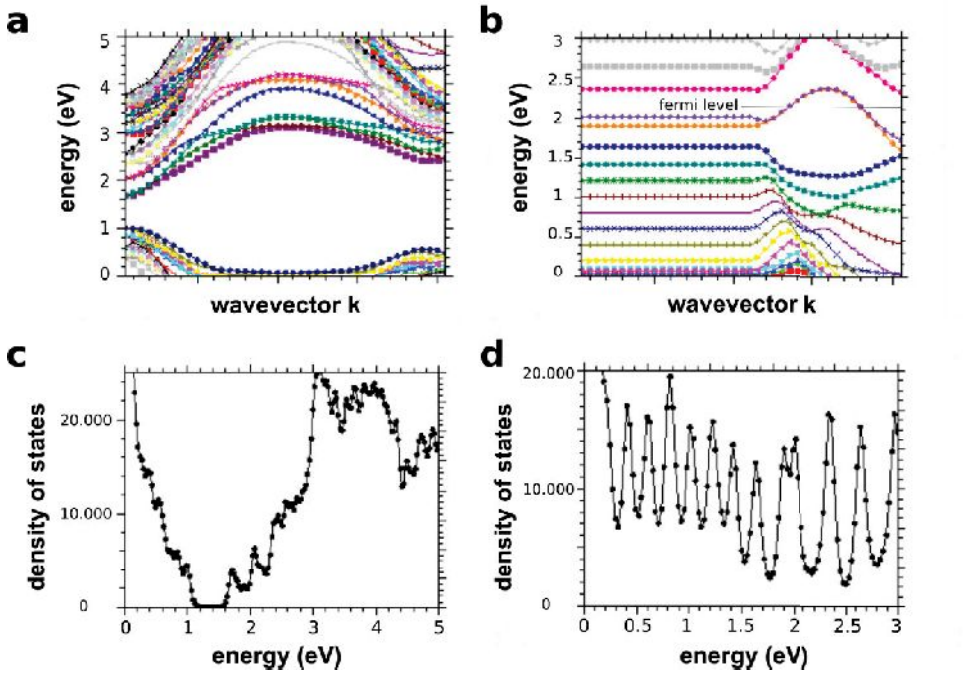

Figure 29. DFT calculations of the PbS band structure. (a) The crystal, cut through the {100} facet (representing the cubes), has a bandgap similar to the bulk material. (b) The crystal, cut through the {111} facet (representing the octahedra), has an overlap between the valence band and the conduction band. (c) The density of states for part a, showing the zero DOS at the bandgap. (d) The DOS for part b, which shows the continuously non-zero DOS.

Transistor behavior of the wires

In order to experimentally investigate the differences between the electrical properties of these wires, they have been contacted individually with Au electrodes and by means of electron-beam lithography. Figure 30 demonstrates a scanning-electron microscope (SEM) image of the fabricated devices. The shape of the employed wires for each device has been determined with the SEM after performing the electrical measurements.

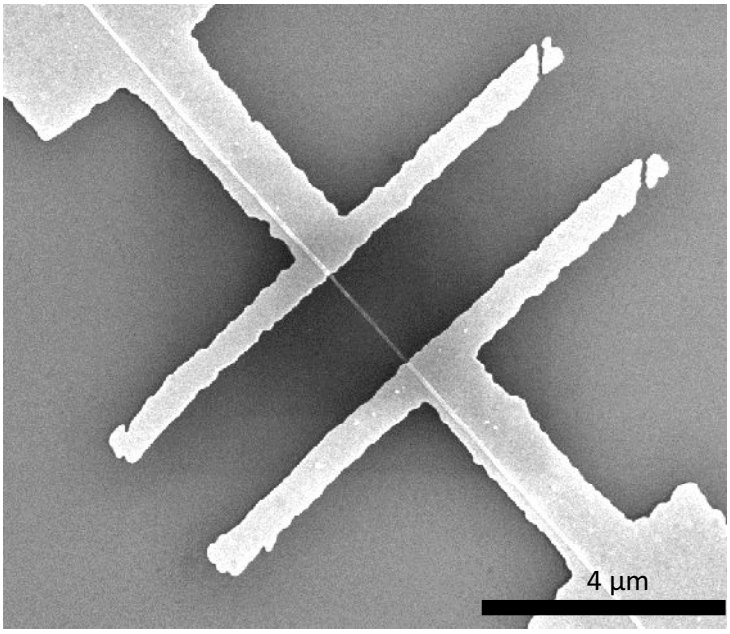

Figure 30. SEM image of the contacted wires with gold electrodes.

After the device fabrication, the sample has been immediately transferred to the vacuum probe station and measured with a back-gate geometry. Figure 31 shows the results of the measurements on the straight wires. Their transfer characteristics (Fig. 31a) demonstrates the clear dependency of their conductivity to the gate voltage. This can be also observed in the output characteristics of these wires, shown in Fig. 31b. The conductivity of these wires is calculated to be 18 ms/cm and they show p-type behavior. The gate dependency is the first sign for their semiconducting behavior.

For the next step, the photoconductivity of these wires has been investigated by the illumination of a red laser (λ = 630 nm). The straight wires experience an increase in the conductivity when they are illuminated with the laser, which is observable in the transfer characteristics (Fig. 31a) and the output characteristics (Fig. 31b). As semiconductors, illuminating these wires results in the optical excitation of the carriers over the bandgap, which increases the amount of the free charge carriers and the conductivity[114,115].

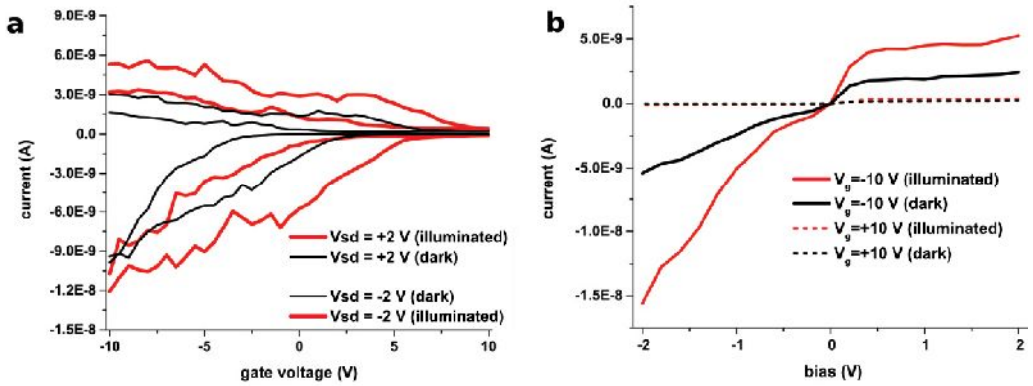

Figure 31. Transfer and output characteristics of the straight wires. (a) The transfer characteristics shows that the conductivity of the wires increases by applying a negative gate voltage or by illuminating them with the laser, as expected for a semiconductor. (b) The output characteristics of the wires also represents the dependency of the conductivity to the gate or to the illumination.

Similar experiments have been also conducted on the zigzag wires. As can be seen in Fig. 32a, the transfer characteristics of the zigzag wires shows that their conductivity cannot be adjusted by the gate-electric field. The same behavior is also observed through their output characteristics, which is depicted in Fig. 32b. Even by applying higher gate voltages (higher than 10 V), no current modulation could be observed. The conductivity of these wires reaches to 27260 mS/cm, which is significantly higher than the conductivity of their semiconducting analogue.

Further, no improvement of the conductivity is detectable when the zigzag wires are illuminated with the laser. As can be seen in Fig. 32, the dark current (shown with black lines) always overlaps with the photocurrent (shown with red lines). Due to the metallic character of these wires and because of the overlap between their valence band and their conduction band, the amount of their mobile carriers is not affected by applying a gate-electric field or by the optical excitation[116].

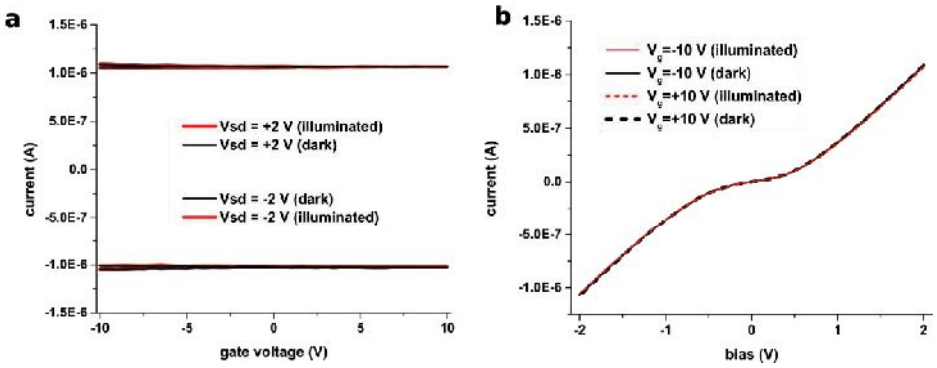

Figure 32. Transfer and output characteristics of the zigzag wires. (a) The transfer characteristics shows that the current is adjustable neither by the gate nor by the illumination, representing metallic behavior. (b) The output characteristics of the zigzag wires also exhibits metallic behavior with a higher conductivity compared to the straight wires and without any response to the gate or to the optical excitation.

Temperature dependency

To further investigate the properties of these wires, the samples have been cooled down in order to observe the temperature dependency of the conductivity. Figure 33a demonstrates the output characteristics of the straight wires in different temperatures, while the gate voltage is kept to zero. As expected for a semiconductor, the conductivity of the wires shows a positive temperature coefficient. By decreasing the temperature, the conductivity of the wires decreases and therefore, a lower current flows through them. A similar behavior has been already observed with the PbS nanosheets[49]. Moreover, Fig. 33b depicts the conductivity and the photoconductivity in different temperatures. Both of these parameters decrease by reducing the temperature, while the ratio of the photocurrent to the dark current increases at low temperatures. All of these observations are in agreement with the behavior of semiconductors. At low temperatures, the thermal excitation of the carriers is suppressed and therefore, less mobile carriers can contribute to the transport[49].

In contrast, the output characteristics of the zigzag wires, depicted in Fig. 33c, shows the increase of the current at lower temperatures. As can be also seen in Fig. 33d, the conductivity has a negative temperature coefficient and therefore, it is maximum for 5 K (the lowest measured temperature), while no photocurrents are detected even at low temperatures. These measurements are the other proof for the metallic character of the zigzag wires. In metals, the carrier concertation is not governed by the thermal excitation. Instead, by

reducing the temperature, phonon scattering is diminished, which increases the diffusion length of the carriers and therefore, the conductivity is improved[117].

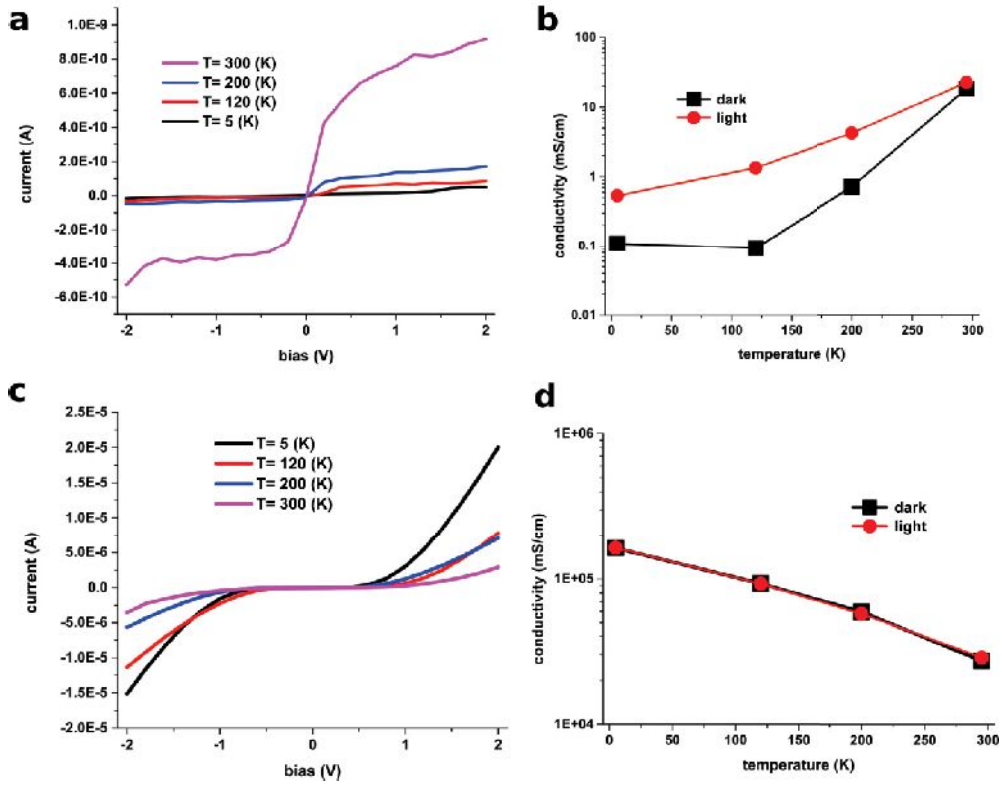

Figure 33. Dependency of the current and the photocurrent to the temperature. (a) The I-V characteristics of the straight wires at various temperatures. Lower currents flow at low temperatures. (b) Temperature dependency of the conductivity and the photoconductivity for the straight wires. At low temperatures, the conductivity and the photoconductivity are lower, while the photocurrent to dark current ratio is higher. (c) The I-V characteristics of the zigzag wires, with higher currents at lower temperatures. (d) The temperature dependency of the conductivity and the photoconductivity for the zigzag wires. The conductivity increases by reducing the temperatures. The photoresponse is absent at all temperatures.

Four point measurements

In order to exclude the effect of the contact resistance, which is mainly caused by the organic ligands on the surface of colloidal materials, the zigzag wires which show unusual metallic behavior have been measured with the four point geometry, and the result is shown in Fig. 34. As can be seen in the inset of this figure, without considering the contact resistance, a linear I-V characteristics is observed. It indicates that the contact resistance is responsible for the S-like shape of the wires' output characteristics (Fig. 32b). The room temperature

conductivity of the crystal (without the contact resistance) is calculated to be 99186 mS/cm, which is even higher than the reported value for bulk galena[118]. This is another sign for the metallic character of the wires.

By decreasing the temperature, a clear reduction is detected for the resistivity of the wires. This reduction saturates at very low temperatures (around 10 K), since the resistivity of metals is typically a power function of the temperature ($\rho \propto T^5$)[117]. The remaining resistivity at low temperatures originates from defects in the crystal, which cannot be compensated by lowering the temperature. These measurements together with the pervious experiments strongly confirm the assumption that the zigzag wires are metallic.

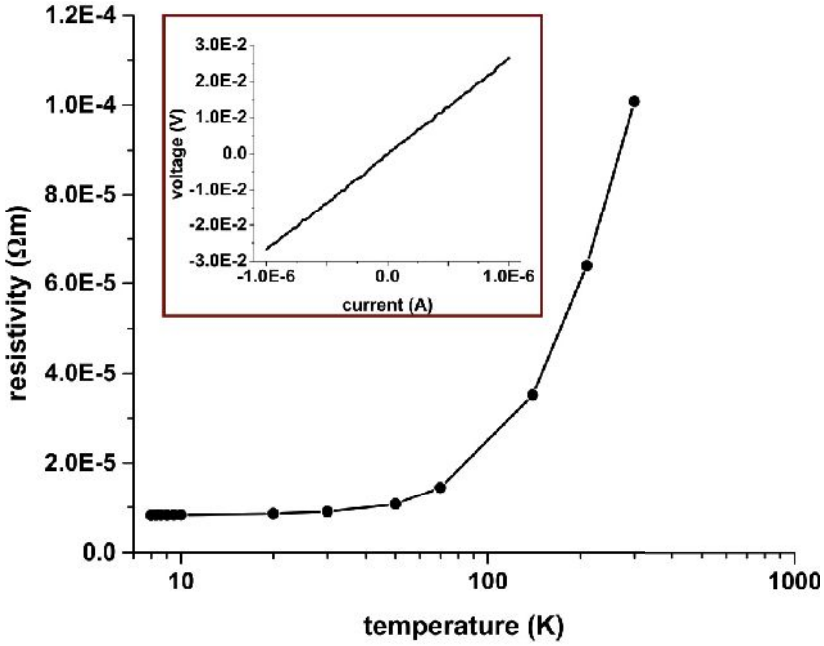

Figure 34. Resistivity of the zigzag wires at different temperatures, obtained by four point measurements. The resistivity decreases by reducing the temperature and saturates at very low temperatures. The inset shows the I-V characteristics of the zigzag wires without considering the contact resistance (achieved by four point measurements).

The other interesting property of the zigzag wires is observed at temperatures below 7.5 K. As already mentioned, these wires represent a constant resistivity at low temperatures. Nevertheless, they experience a resistivity drop below ~ 7.5 K (Fig. 35). This temperature is consistent with the transition temperature of Pb into the superconductivity phase[119-122]. Therefore, it might be concluded that the zigzag wires show superconductivity, resulting from

the Pb rich surface. In order to confirm this theory, more measurements are required. Especially, quenching the superconductivity phase must be observed by the application of magnetic fields. Such experiments could provide more information about the real origin of the detected resistivity drop.

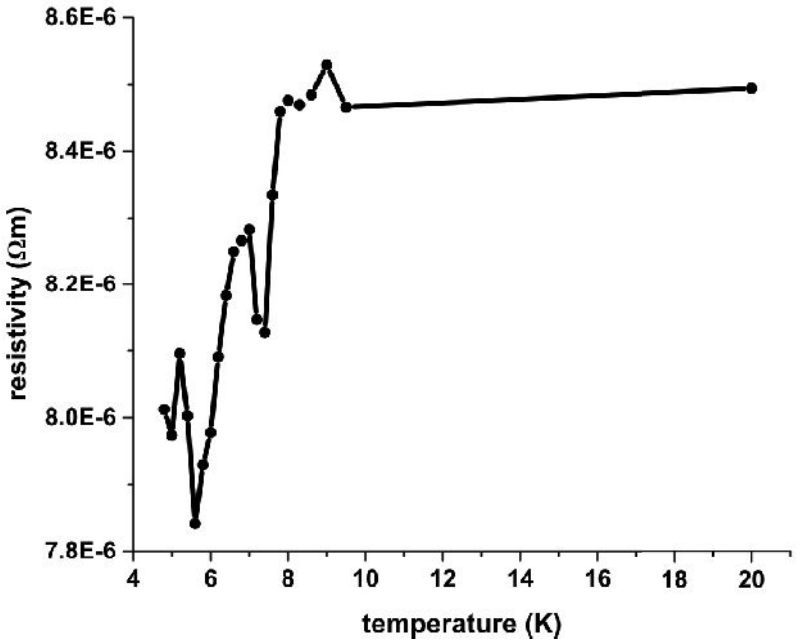

Figure 35. Resistivity of the zigzag wires at temperatures below 20 K. A resistivity drop is observed at around 7.5 K which could be a transition to superconductivity. This effect might originate from the Pb monolayer on the surface of the wires.

Discussion

The performed electrical measurements undoubtedly confirmed that the zigzag wires are metallic. This property originates from the crystal cut through the {111} facet which makes the surface Pb rich. In order to clarify why this specific cut results in metallic behavior, a closer look is required on Pb/S bonds of the PbS crystal. As can be seen in Fig. 36, every Pb atom is bound to 6 S atoms to form the crystal. It donates in total 2 positive charges to these S atoms. When the crystal is cut through the {111} facet, half of these bonds (3 of them) are broken and therefore, one uncompensated positive charge remains for the Pb atom. These uncompensated charges, which exist on the whole surface, change its character to metallic[112]. Although the octahedra, as the building blocks of the zigzag nanowires, are metallic, there are some conditions to observe this metallic behavior after their attachment (i.e. for the zigzag wires). First of all, the shape of the wires must be well-defined. After the attachment of the

octahedra and during the growth phase, the crystal expands in size. In this phase, if any facets other than the {111} facet grow, especially the {100} facets, the shape of the wires would be distorted. This leads to the discontinuity of the metallic path and to the destruction of metallic behavior. The uncontrolled growth of the wires can be seen schematically in Fig. 37a and through the TEM image in Fig. 37b.

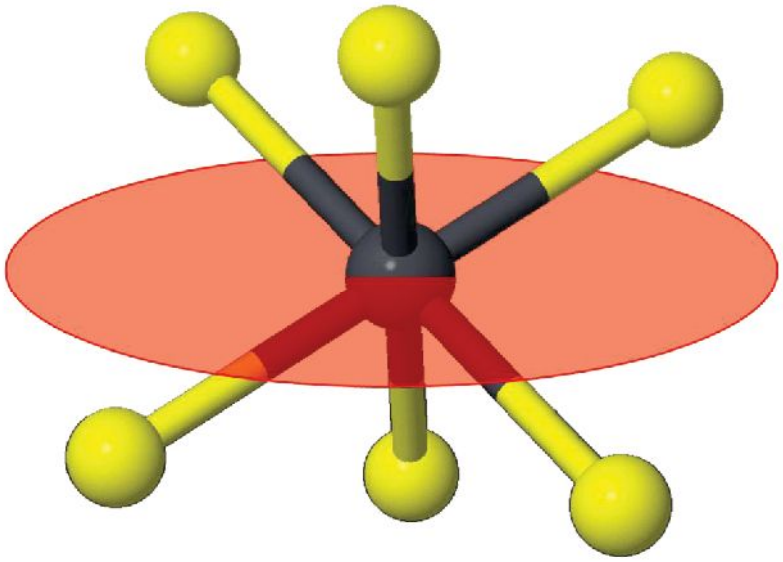

Figure 36. Pb and S atoms in the PbS crystal. By cutting the crystal through the {111} facet (the plane shown in red), three of the bonds are broken, leaving the Pb atom with one uncompensated charge.

Therefore, it is crucial to have a well-defined shape in order to preserve the metallic character. Here, accurately adjusting the synthesis time and employing the right amounts of ligands play a key role to accurately cut the crystal and to have a well-defined shape (more information in the Appendix).

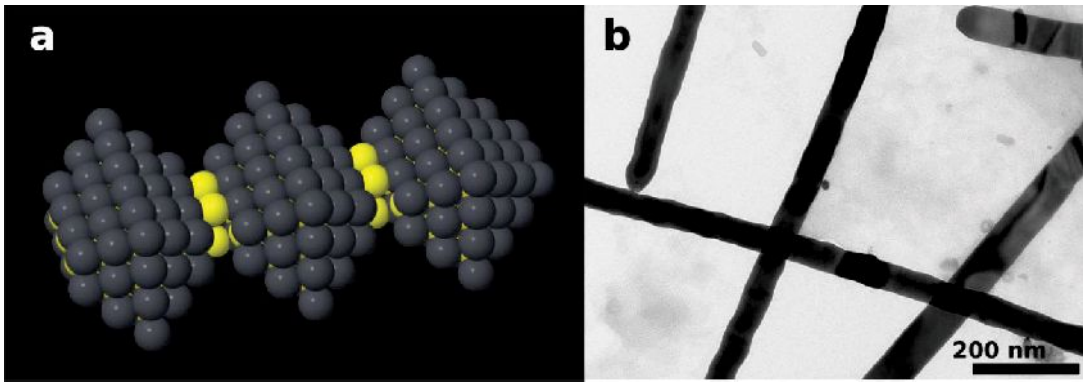

Figure 37. Losing the shape of the zigzag wires during the growth phase. (a) The schematic view of the zigzag wires with the grown {100} facets, which results in the discontinuity of the metallic surface. (b) The TEM image of the over-grown wires without the well-defined shape and metallic behavior.

The other important point is the coverage of Cl^- ions on the surface. As it can be found in the literature and as the DFT calculations show (Fig. 38a), when the surface of the crystal is completely covered with Cl^- ions, a forbidden gap is formed in the band structure of the crystal[112,113]. Therefore, semiconducting behavior must be observed, as the DOS also drops to zero for the bandgap of such a crystal (Fig. 38b).

To check the Cl content of the wires, they were probed with the X-ray photoelectron spectroscopy (XPS)[90,123]. Figure 38c shows the Pb 4f peaks for the flat and zigzag samples. The Pb 4f peaks centered at 137.4 eV and 142.3 eV are attributed to Pb 4f 7/2 and Pb 4f 5/2 of PbS, respectively. Further the peaks at 138.2 eV, 143.0 eV, 136.4, and 141.3 are assigned to Pb 4f 7/2 and Pb 4f 5/2 of PbO_2 and Pb-O. Eventually, the XPS peaks at 138.8 eV and 143.7 eV are assigned to Pb 4f 7/2 and Pb 4f 5/2 of Pb^{2+} in $PbCl_2$. By comparing the intensity of the peaks (the $PbCl_2$ peaks and the PbS peaks), it can be seen that the Cl content of the zigzag wires (15%) is rather low compared to the straight wires (20 %) and also compared to the previously studied PbS nanosheets (30-60 %)[96]. Therefore, it can be concluded that the performed synthesis fulfills this requirement and preserves metallic behavior of the wires by reducing the Cl content of the crystal.

It is worthy to point out that the metallic nature of the zigzag wires is further evidenced by the XPS spectra. Peak narrowing is observed for the core level spectra, compared to the straight wires, suggesting a relative increase in the conductivity[124] (the other peaks of the XPS spectra are shown in Fig. S8 in part A2 of the Appendix).

One might argue that the Pb terminated surface of the zigzag wires could be a foundation for the growth of a pure Pb shell around the wires, which could also make them metallic. To address this question, the HRTEM image of these wires (shown in Fig. 26c) was checked. As can be seen, there is no distortion of the crystal at the surface and its periodicity is constant. This demonstrates that the whole crystal is PbS or in other words, no Pb shell is formed around the wires. This could be also observed by the XPS measurements in Fig. 38c. It shows that metallic Pb species are absent from both samples, since their presence could be inferred by the observation of a sharp, asymmetric peak, observable at low binding energies[125].

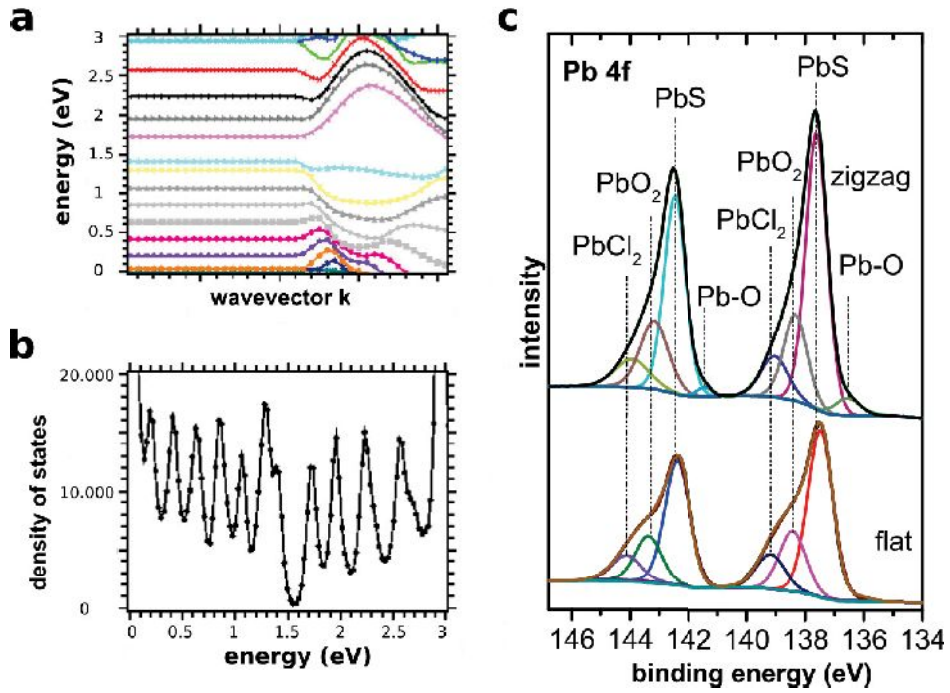

Figure 38. The Cl effect on the properties of the zigzag wires. (a) The band structure of the Cl covered crystal with the {111} cut. Reopening the bandgap is observable. (b) The calculated DOS for the mentioned crystal, which is equal to zero for the bandgap, showing semiconducting behavior. (c) Deconvoluted XPS peaks of the samples for the Pb 4f region. By considering the Cl/S ratio, achieved by comparing the $PbCl_2$ and PbS peaks, a low amount of Cl content is detected for the zigzag wires.

Conclusion

In summary, the electrical properties of PbS nanowires were tuned from semiconducting to metallic by cutting the crystal in a different way. While various forms of PbS nanostructures are semiconducting, when the crystal is cut through the {111} facets, a Pb rich layer remains around the crystal which makes it metallic. Such a crystal could be colloidally formed by the formation and the attachment of octahedra, which are made during the early stages of the synthesis. Several methods including DFT calculations, field-effect, photoconductivity, and temperature dependency measurements were employed to confirm the metallic character of these wires. It turned out that the well-defined shape and the low amounts of Cl content play crucial roles for preserving metallic behavior. These results provide the opportunity to further optimize the colloidal materials and to simply tune their properties according to the target application. Further, they introduce new applications for the PbS nanocrystals, including flexible interconnects.

3-8 Conference Proceedings: Rashba Spin-Orbit Coupling in Colloidal Lead Sulfide Stripes

This part presents the results of the spin transport measurements on the narrow stripes. This work has been published as conference proceedings. Similar to the previous works, I was responsible to design, perform and evaluate the experimental part. This is a reprint from: *Rashba Spin-Orbit Coupling in Colloidal Lead Sulfide Nanosheets,* Mohammad Mehdi Ramin Moayed, Thomas Bielewicz, Martin Sebastian Zöllner, Carmen Herrmann, and Christian Klinke. Advanced Photonics **2017**, OSA Technical Digest NoTu1C.3[126]. Copyright ©2017 Optical Society of America.

Rashba Spin-Orbit Coupling in Colloidal Lead Sulfide Nanosheets

Mohammad Mehdi Ramin Moayed[1], Thomas Bielewicz[1], Martin Sebastian Zoellner[2], Carmen Herrmann[2], Christian Klinke[1]

[1]Institute of Physical Chemistry, University of Hamburg, 20146 Hamburg, Germany
Phone: +49 (0)40 42838- 8210, E-mail: klinke@chemie.uni-hamburg.de
[2]Institute of Inorganic Chemistry, University of Hamburg, 20146 Hamburg, Germany

Abstract
We investigated the Rashba-type spin-orbit coupling in colloidal lead sulfide nanosheets and its dependency to the geometry of the nanosheets by performing circular photogalvanic effect measurements.

1. Introduction

Employing the spin degree of freedom instead of the electrical charge is one of the suggested ideas for the future of data processing due to the low power consumption and the superior functionality of this concept. Colloidal chemistry as an easy and inexpensive method for producing high-quality nanomaterials can be employed to synthesize the required materials for spin-dependent components. In order to evidence that, we have investigated the spin-orbit coupling (SOC) in colloidal lead sulfide nanosheets and its dependency to the geometry of the nanosheets by performing circular photogalvanic effect (CPGE) measurements. Although the PbS rock salt crystal has point symmetry, asymmetric interfaces on top of the material and underneath, as well as the gate electric field can affect the confined crystal and structurally break the symmetry, leading to the Rashba type SOC generation. Our results show that this effect can be tuned by altering the lateral size (width) of the nanosheets. Spin-orbit coupling is a key feature in spintronics which allows manipulating the spin direction by means of external electric fields. The observation of this effect in colloidal materials can be a breakthrough for future inexpensive spintronic devices.

By approaching the end of the Moore's law, it is crucial to develop new concepts or new materials for the future of data processing [1,2]. Using the spin/valley degree of freedom instead of the electrical charge is among the suggested ideas, leading to the introduction of spintronics and valleytronics concepts [3,4]. Up to now, these concepts have been mainly investigated in 2D materials produced by cost-intensive methods such as molecular-beam epitaxy (MBE) [1,5]. Here we show that materials synthesized by colloidal chemistry have the potential to be employed for spintronics, by realization of Rashba spin-orbit interactions through circular-photogalvanic effect measurements. Colloidal synthesis of nanomaterials offers the possibility to inexpensively produce high-quality crystals. Among the colloidal materials, 2D lead sulfide nanosheets show promising properties [6,7]. Although their rock salt crystal structure is centrosymmetric, the symmetry can be broken by the application of asymmetric boundaries underneath and above the crystal (SiO_2 and vacuum) as well as a gate electric field, leading to Rashba type splitting in the band structure. The effect can be tuned by altering the gate voltage, the thickness of the nanosheets (confinement) [1] and their lateral dimensions.

2. Device preparation

Lead sulfide nanosheets have been synthesized following the reported approaches [7] and spin-coated on a Si/SiO_2 substrate. Individual nanosheets were contacted with Ti/Au by means of electron-beam lithography and metal evaporation following by the lift-off process. Then, the sample was transferred to a vacuum probe station and measured at room temperature. In order to observe the circular-photogalvanic effect, a circularly-polarized laser beam (λ=627 nm) was obliquely illuminated to the sample, and the generated current was measured while the bias voltage was kept to zero.

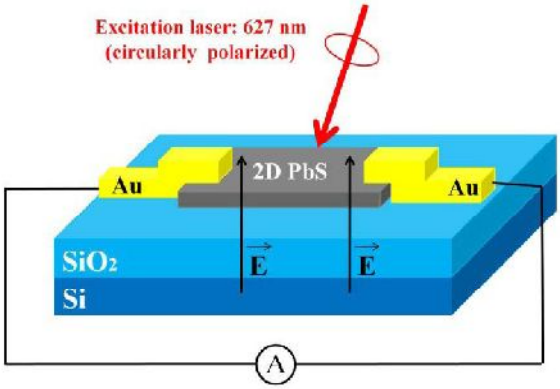

Fig. 1 Schematic of the test setup, which breaks the inversion symmetry by a gate electric field and by asymmetric vertical interfaces (SiO_2 and vacuum).

3. Results and discussion

Figure 1 schematically illustrates the setup of the CPGE measurements. By the application of a gate electric field and asymmetric vertical interfaces, this setup reduces the symmetry in the crystal from the O_h point group (inversion symmetric) to C_{4v} (asymmetric). As we recently showed in [1], breaking the symmetry in the PbS nanocrystal results in splitting the valence and the conduction bands at the M

point valleys, corresponding to the (110) direction, at the corners of the rectangular brillouin zone.

The angular momentum of such bands becomes different for the spin-up and spin-down carriers but remains equal for the M and M' valleys (valleys with opposite directions). Therefore, upon illumination with circularly-polarized light, photoexcited carriers are spin polarized but valley un-polarized [1].

Figure 2 shows the photocurrent of the nanosheets at 0 V bias and in different angles of the used quarter-wave plate, corresponding to different helicities of the circularly-polarized light (V_g= -10 V). The measured photocurrent includes a background current originating from the photovoltaic effect (I_0), a contribution from the linear-photogalvanic effect (I_{LPGE}), and eventually, the circular-photogalvanic current (I_{CPGE}), a helicity-dependent current which is attributed to the Rashba SOC in the crystal [1,4,8,9]. Population of the split bands with spin-polarized carriers results in asymmetric distribution of the carriers in momentum space (compared to the Γ point), and generation of I_{CPGE} [1,4,9]. By fitting the measured photocurrent by employing eq. (1) (φ is the angle of the quarter-wave plate), I_0 and I_{CPGE} are obtained equal to 28 and 4.6 pA respectively.

$$J_{total} = J_0 + J_{CPGE}\sin(2\varphi) + J_{LPGE}\sin(2\varphi)\cos(2\varphi) \qquad (1)$$

In order to exclude the spin-independent effects on I_{CPGE}, such as light absorption capability, the normalized CPGE (I_{CPGE}/I_0) is calculated to show the strength of the Rashba effect. As reported in [1] for a 2 µm wide nanosheet with a thickness of 10-12 nm, the normalized CPGE can reach to 7 %. Here, although the thickness is similar to the aforementioned nanosheets, by reducing the lateral size (width=100 nm), this parameter can be improved to 16 %.

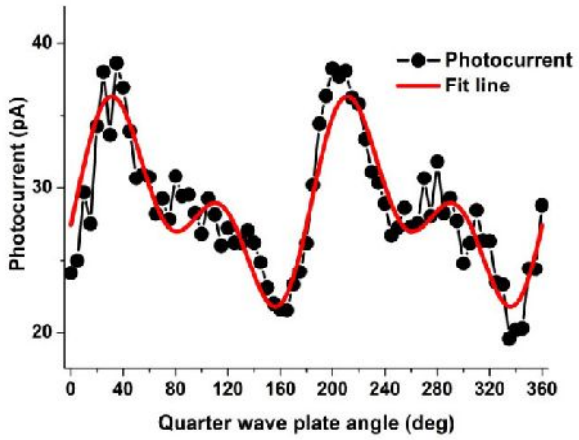

Fig. 2 Variation of the photocurrent at 0 V bias by changing the angle of the quarter-wave plate (light helicity). The CPGE current constitutes 16 % of the photocurrent (V_g = -10 V).

By confining the crystal also in the width, the effect of the back gate originating electric field on the crystal becomes more pronounced. By intensifying the effective electric field, higher degrees of asymmetry are imposed to the crystal which leads to the wider splitting of the bands. Therefore, a higher normalized CPGE current can be detected through illumination of the crystal with circularly-polarized light [1].

4. Conclusions

Rashba spin-orbit coupling has been investigated in colloidal lead sulfide nanosheets with reduced widths. Circular-photogalvanic measurements showed that Rashba band splitting can occur as a result of a gate electric field and asymmetric interfaces to the crystal. The effect could be improved by reducing the width of the crystal. Our observation suggests that colloidal chemistry can support the recent spintronic approaches by inexpensively providing the required active material.

Acknowledgements

M.M.R.M., T.B. and C.K. gratefully acknowledge financial support of the European Research Council via the ERC Starting Grant "2D-SYNETRA" (Seventh Framework Program FP7, Project: 304980). C.K. thanks the German Research Foundation DFG for financial support in the frame of the Cluster of Excellence "Center of ultrafast imaging CUI" and the Heisenberg scholarship KL 1453/9-2. M.S.Z. and C.H. thank the DFG for funding via the project SFB668 (project B17) and the North-German Supercomputing Alliance (HLRN) for computational resources.

References

[1] M. M. Ramin Moayed, T. Bielewicz, M. S. Zöllner, C. Herrmann, C. Klinke, Nature Commun. 8 (2017) 15721.
[2] M. M. Waldrop, Nature **530** (2016) 144-147.
[3] H. Zeng, J. Dai, W. Yao, D. Xiao, X. Cui, Nature Nanotech. **7** (2012) 490–493.
[4] S. Zhang, N. Tang, W. Jin, J. Duan, X. He, X. Rong, C. He, L. Zhang, X. Qin, L. Dai, Y. Chen, W. Ge, B. Shen, Nano Lett. **15** (2015) 1152-1157.
[5] S. Dhara, E. J. Mele, R. Agarwal, Science **349** (2015) 726-729.
[6] C. Schliehe, B. H. Juarez, M. Pelletier, S. Jander, D. Greshnykh, M. Nagel, A. Meyer, S. Foerster, A. Kornowski, C. Klinke, H. Weller, Science **329** (2010) 550-553.
[7] T. Bielewicz, M. M. Ramin Moayed, V. Lebedeva, C. Strelow, A. Rieckmann, C. Klinke, Chem. Mater. **27** (2015) 8248–8254.
[8] H. Yuan, X. Wang, B. Lian, H. Zhang, X. Fang, B. Shen, G. Xu, Y. Xu, S. Zhang, H. Y. Hwang, Y. Cui, Nature Nanotech. **9** (2014) 851–857.
[9] M. Eginligil, B. Cao, Z. Wang, X. Shen, C. Cong, J. Shang, C. Soci. T. Yu, Dichroic, Nature Commun. **6** (2015) 7636.

View publication stats

References

1 Moore, G. E. Cramming more components onto integrated circuits. *Proceedings of the IEEE* **86**, 82-85 (1998).

2 Moore, G. E. Progress in digital integrated electronics [Technical literaiture, copyright 1975 IEEE. reprinted, with permission. technical digest. international electron devices meeting, IEEE, 1975, pp. 11-13.]. *IEEE Solid-State Circuits Society Newsletter* **20**, 36-37 (1975).

3 Brock, D. C. & Moore, G. E. *Understanding Moore's law: four decades of innovation*. (Chemical Heritage Foundation, 2006).

4 Normile, D. The End--Not Here Yet, But Coming Soon. *Science* **293**, 787 (2001).

5 Waldrop, M. M. More than moore. *Nature* **530**, 144-148 (2016).

6 Mann, C. C. The end of Moores law. *Technology Review* **103**, 42-48 (2000).

7 Mack, C. A. The end of the semiconductor industry as we know it. *Emerging Lithographic Technologies VII, in Proceedings of SPIE.* **5037**, 1-11 (2013).

8 Moore, G. E. Lithography and the future of Moore's law. *Proc. SPIE 2439, Integrated Circuit Metrology, Inspection, and Process Control IX.* 2-18 (International Society for Optics and Photonics, 1995).

9 Tummala, R. R. SOP: What is it and why? A new microsystem-integration technology paradigm-Moore's law for system integration of miniaturized convergent systems of the next decade. *IEEE Transactions on Advanced Packaging* **27**, 241-249 (2004).

10 Tanida, K. *et al.* Ultra-high-density 3D chip stacking technology. *Electronic Components and Technology Conference, Proceedings. 53rd.* 1084-1089 (IEEE) *(*2003).

11 Takahashi, K. *et al.* Current status of research and development for three-dimensional chip stack technology. *Japanese Journal of Applied Physics* **40**, 3032 (2001).

12 Shalf, J. M. & Leland, R. Computing beyond moore's law. *Computer* **48**, 14-23 (2015).

13 Robert, F. Beyond graphene. *Science* **348**, 490-492 (2015).

14 DiVincenzo, D. P. The Physical Implementation of Quantum Computation. *Fortschritte der Physik* **48**, 771-783 (2000).

15 Monroe, D. Neuromorphic computing gets ready for the (really) big time. *Communications of the ACM* **57**, 13-15 (2014).

16 Monroe, C., Meekhof, D., King, B., Itano, W. M. & Wineland, D. J. Demonstration of a fundamental quantum logic gate. *Physical review letters* **75**, 4714 (1995).

17 Mead, C. Neuromorphic electronic systems. *Proceedings of the IEEE* **78**, 1629-1636 (1990).

18 Poon, C.-S. & Zhou, K. Neuromorphic silicon neurons and large-scale neural networks: challenges and opportunities. *Frontiers in neuroscience* **5**, 108 (2011).

19 Bhimanapati, G. R. *et al.* Recent advances in two-dimensional materials beyond graphene. *Acs Nano* **9**, 11509-11539 (2015).

20 Tian, H. *et al.* Low-symmetry two-dimensional materials for electronic and photonic applications. *Nano Today* **11**, 763-777 (2016).

21 Butler, S. Z. *et al.* Progress, challenges, and opportunities in two-dimensional materials beyond graphene. *ACS nano* **7**, 2898-2926 (2013).

22 Pulizzi, F. Spintronics. *Nature Materials* **11**, 367 (2012).

23 Nebel, C. E. Valleytronics: Electrons dance in diamond. *Nature materials* **12**, 690 (2013).

24 Geim, A. K. & Novoselov, K. S. The rise of graphene. *Nature materials* **6**, 183 (2007).

25 Schwierz, F. Graphene transistors. *Nature nanotechnology* **5**, 487 (2010).

26 Cooper, D. R. *et al.* Experimental review of graphene. *ISRN Condensed Matter Physics* **2012**, 501686 (2012).

27 Wakabayashi, K., Fujita, M., Ajiki, H. & Sigrist, M. Electronic and magnetic properties of nanographite ribbons. *Physical Review B* **59**, 8271 (1999).

28 Nakada, K., Fujita, M., Dresselhaus, G. & Dresselhaus, M. S. Edge state in graphene ribbons: Nanometer size effect and edge shape dependence. *Physical Review B* **54**, 17954 (1996).

29 Radisavljevic, B., Radenovic, A., Brivio, J., Giacometti, i. V. & Kis, A. Single-layer MoS 2 transistors. *Nature nanotechnology* **6**, 147 (2011).

30 Mak, K. F., Lee, C., Hone, J., Shan, J. & Heinz, T. F. Atomically thin MoS 2: a new direct-gap semiconductor. *Physical review letters* **105**, 136805 (2010).

31 Li, L. *et al.* Black phosphorus field-effect transistors. *Nature nanotechnology* **9**, 372 (2014).

32 Zeng, H., Dai, J., Yao, W., Xiao, D. & Cui, X. Valley polarization in MoS 2 monolayers by optical pumping. *Nature nanotechnology* **7**, 490 (2012).

33 Yuan, H. *et al.* Generation and electric control of spin–valley-coupled circular photogalvanic current in WSe 2. *Nature nanotechnology* **9**, 851 (2014).

34 Mak, K. F., He, K., Shan, J. & Heinz, T. F. Control of valley polarization in monolayer MoS 2 by optical helicity. *Nature nanotechnology* **7**, 494 (2012).

35 Novoselov, K. & Neto, A. C. Two-dimensional crystals-based heterostructures: materials with tailored properties. *Physica Scripta* **2012**, 014006 (2012).

36 Bonaccorso, F. *et al.* Production and processing of graphene and 2d crystals. *Materials today* **15**, 564-589 (2012).

37 Talapin, D. V., Lee, J.-S., Kovalenko, M. V. & Shevchenko, E. V. Prospects of colloidal nanocrystals for electronic and optoelectronic applications. *Chemical reviews* **110**, 389-458 (2009).

38 Talapin, D. V. & Murray, C. B. PbSe nanocrystal solids for n-and p-channel thin film field-effect transistors. *Science* **310**, 86-89 (2005).

39 Claridge, S. A. *et al.* Cluster-assembled materials. *ACS nano* **3**, 244-255 (2009).

40 Park, J., Joo, J., Kwon, S. G., Jang, Y. & Hyeon, T. Synthesis of monodisperse spherical nanocrystals. *Angewandte Chemie International Edition* **46**, 4630-4660 (2007).

41 Jun, Y. w., Choi, J. s. & Cheon, J. Shape control of semiconductor and metal oxide nanocrystals through nonhydrolytic colloidal routes. *Angewandte Chemie International Edition* **45**, 3414-3439 (2006).

42 Murray, C. B., Kagan, a. C. & Bawendi, M. Synthesis and characterization of monodisperse nanocrystals and close-packed nanocrystal assemblies. *Annual Review of Materials Science* **30**, 545-610 (2000).

43 Palmstrom, A. F., Santra, P. K. & Bent, S. F. Atomic layer deposition in nanostructured photovoltaics: tuning optical, electronic and surface properties. *Nanoscale* **7**, 12266-12283 (2015).

44 Ivanov, V. K., Fedorov, P. P., Baranchikov, A. Y. & Osiko, V. V. e. Oriented attachment of particles: 100 years of investigations of non-classical crystal growth. *Russian Chemical Reviews* **83**, 1204 (2014).

45 Lee, E. J., Ribeiro, C., Longo, E. & Leite, E. R. Oriented attachment: An effective mechanism in the formation of anisotropic nanocrystals. *The Journal of Physical Chemistry B* **109**, 20842-20846 (2005).

46 Zhou, Y., Itoh, H., Uemura, T., Naka, K. & Chujo, Y. Preparation, optical spectroscopy, and electrochemical studies of novel π-conjugated polymer-protected stable PbS colloidal nanoparticles in a nonaqueous solution. *Langmuir* **18**, 5287-5292 (2002).

47 Machol, J. L., Wise, F. W., Patel, R. C. & Tanner, D. B. Vibronic quantum beats in PbS microcrystallites. *Physical Review B* **48**, 2819 (1993).

48 Aerts, M. *et al.* Highly efficient carrier multiplication in PbS nanosheets. *Nature communications* **5**, 3789 (2014).

49 Dogan, S., Bielewicz, T., Cai, Y. & Klinke, C. Field–effect transistors made of individual colloidal PbS nanosheets. *Applied Physics Letters* **101**, 073102 (2012).

50 Dogan, S., Bielewicz, T., Lebedeva, V. & Klinke, C. Photovoltaic effect in individual asymmetrically contacted lead sulfide nanosheets. *Nanoscale* **7**, 4875-4883 (2015).

51 Schliehe, C. *et al.* Ultrathin PbS sheets by two-dimensional oriented attachment. *Science* **329**, 550-553 (2010).

52 Bielewicz, T., Dogan, S. & Klinke, C. Tailoring the Height of Ultrathin PbS Nanosheets and Their Application as Field-Effect Transistors. *Small* **11**, 826-833 (2015).

53 Bielewicz, T. *et al.* From dots to stripes to sheets: shape control of lead sulfide nanostructures. *Chemistry of Materials* **27**, 8248-8254 (2015).

54 Bielewicz, T., Klein, E. & Klinke, C. New ways to synthesize lead sulfide nanosheets—substituted alkanes direct the growth of 2D nanostructures. *Nanotechnology* **27**, 355602 (2016).

55 Cho, K.-S., Talapin, D. V., Gaschler, W. & Murray, C. B. Designing PbSe nanowires and nanorings through oriented attachment of nanoparticles. *Journal of the American Chemical Society* **127**, 7140-7147 (2005).

56 Xu, F., Ma, X., Gerlein, L. F. & Cloutier, S. G. Designing and building nanowires: directed nanocrystal self-assembly into radically branched and zigzag PbS nanowires. *Nanotechnology* **22**, 265604 (2011).

57 Jang, S. Y. *et al.* Three synthetic routes to single-crystalline PbS nanowires with controlled growth direction and their electrical transport properties. *ACS nano* **4**, 2391-2401 (2010).

58 Zha, C. *et al.* Facet engineering of monodisperse PbS nanocrystals with shape-and facet-dependent photoresponse activity. *RSC Advances* **6**, 107151-107157 (2016).

59 Fang, C., van Huis, M. A., Vanmaekelbergh, D. & Zandbergen, H. W. Energetics of polar and nonpolar facets of PbSe nanocrystals from theory and experiment. *ACS nano* **4**, 211-218 (2009).

60 Sze, S. M. *Semiconductor devices: physics and technology*. (John Wiley & Sons, 2002).

61 Herman, F., Kortum, R. L. & Ortenburger, I. B. Relativistic band structure of GeTe, SnTe, PbTe, PbSe, and PbS. *Le Journal de Physique Colloques* **29**, C4-62-C64-77 (1968).

62 Neamen, D. A. *Semiconductor physics and devices*. Vol. 3 (McGraw-Hill New York, 2003).

63 Pierret, R. F. *Semiconductor Device Fundamentals*. (Addison-Wesley Publishing Company, Inc. PNPN Devices, 1996).

64 Rogach, A. L. *et al.* Organization of matter on different size scales: monodisperse nanocrystals and their superstructures. *Advanced Functional Materials* **12**, 653-664 (2002).

65 Grundmann, M. *The Physics of Semiconductors: An Introduction Including Nanophysics and Applications*. (Springer, 2010).

66 Cao, G. *Nanostructures & nanomaterials: synthesis, properties & applications*. (Imperial college press, 2004).

67 Sze, S. M. & Ng, K. K. *Physics of semiconductor devices*. (John wiley & sons, 2006).

68 Chuang, H.-J. *et al.* High mobility WSe2 p-and n-type field-effect transistors contacted by highly doped graphene for low-resistance contacts. *Nano letters* **14**, 3594-3601 (2014).

69 Chuang, H.-J. *et al.* Low-resistance 2D/2D ohmic contacts: A universal approach to high-performance WSe2, MoS2, and MoSe2 transistors. *Nano letters* **16**, 1896-1902 (2016).

70 Wang, R. *et al.* Colloidal quantum dot ligand engineering for high performance solar cells. *Energy & Environmental Science* **9**, 1130-1143 (2016).

71 Zanella, M. *et al.* Atomic ligand passivation of colloidal nanocrystal films via their reaction with propyltrichlorosilane. *Chemistry of Materials* **25**, 1423-1429 (2013).

72 Fabian, J., Matos-Abiague, A., Ertler, C., Stano, P. & Zutic, I. Semiconductor spintronics. *arXiv preprint arXiv:0711.1461* (2007).

73 Fert, A. Nobel lecture: Origin, development, and future of spintronics. *Reviews of Modern Physics* **80**, 1517 (2008).

74 Chappert, C., Fert, A. & Van Dau, F. N. The emergence of spin electronics in data storage. *Nature materials* **6**, 813 (2007).

75 Koo, H. C. *et al.* Control of spin precession in a spin-injected field effect transistor. *Science* **325**, 1515-1518 (2009).

76 Dyakonov, M. I. & Khaetskii, A. *Spin physics in semiconductors*. Vol. 1 (Springer, 2008).

77 Žutić, I., Fabian, J. & Sarma, S. D. Spintronics: Fundamentals and applications. *Reviews of modern physics* **76**, 323 (2004).

78 Datta, S. & Das, B. Electronic analog of the electro-optic modulator. *Applied Physics Letters* **56**, 665-667 (1990).

79 Giglberger, S. *et al.* Rashba and Dresselhaus spin splittings in semiconductor quantum wells measured by spin photocurrents. *Physical Review B* **75**, 035327 (2007).

80 Ganichev, S. D. & Golub, L. E. Interplay of Rashba/Dresselhaus spin splittings probed by photogalvanic spectroscopy–A review. *physica status solidi (b)* **251**, 1801-1823 (2014).

81 Kohda, M. *et al.* Gate-controlled persistent spin helix state in (In, Ga) As quantum wells. *Physical Review B* **86**, 081306 (2012).

82 Zhang, S. *et al.* Generation of Rashba spin–orbit coupling in CdSe nanowire by ionic liquid gate. *Nano letters* **15**, 1152-1157 (2015).

83 Ivchenko, E. L. Circular photogalvanic effect in nanostructures. *Physics-Uspekhi* **45**, 1299-1303 (2002).

84 He, X. *et al.* Circular photogalvanic effect of the two-dimensional electron gas in Al x Ga 1− x N⁄ Ga N heterostructures under uniaxial strain. *Applied Physics Letters* **91**, 071912 (2007).

85 Ganichev, S. D. & Prettl, W. Spin photocurrents in quantum wells. *Journal of physics: Condensed matter* **15**, R935 (2003).

86 Ganichev, S., Ivchenko, E. & Prettl, W. Photogalvanic effects in quantum wells. *Physica E: Low-dimensional Systems and Nanostructures* **14**, 166-171 (2002).

87 Ganichev, S. *et al.* Conversion of spin into directed electric current in quantum wells. *Physical review letters* **86**, 4358 (2001).

88 Yin, C. *et al.* Tunable surface electron spin splitting with electric double-layer transistors based on InN. *Nano letters* **13**, 2024-2029 (2013).

89 Zhang, Q. *et al.* Strong circular photogalvanic effect in ZnO epitaxial films. *Applied Physics Letters* **97**, 041907 (2010).

90 Morris-Cohen, A. J., Malicki, M., Peterson, M. D., Slavin, J. W. & Weiss, E. A. Chemical, structural, and quantitative analysis of the ligand shells of colloidal quantum dots. *Chemistry of Materials* **25**, 1155-1165 (2012).

91 Stavrinadis, A. & Konstantatos, G. Strategies for the controlled electronic doping of colloidal quantum dot solids. *ChemPhysChem* **17**, 632-644 (2016).

92 Shim, M. & Guyot-Sionnest, P. N-type colloidal semiconductor nanocrystals. *Nature* **407**, 981 (2000).

93 Ning, Z. *et al.* Air-stable n-type colloidal quantum dot solids. *Nature materials* **13**, 822 (2014).

94 Kovalenko, M. V., Scheele, M. & Talapin, D. V. Colloidal nanocrystals with molecular metal chalcogenide surface ligands. *Science* **324**, 1417-1420 (2009).

95 Nag, A. *et al.* Metal-free inorganic ligands for colloidal nanocrystals: S2–, HS–, Se2–, HSe–, Te2–, HTe–, TeS32–, OH–, and NH2–as surface ligands. *Journal of the American Chemical Society* **133**, 10612-10620 (2011).

96 Ramin Moayed, M. M., Bielewicz, T., Noei, H., Stierle, A. & Klinke, C. High Performance n- and p-Type Field-Effect Transistors Based on Hybridly Surface-Passivated Colloidal PbS Nanosheets. *Advanced Functional Materials*, 1706815 (2018).

97 Moayed, M. M. R., Bielewicz, T., Zöllner, M. S., Herrmann, C. & Klinke, C. Towards colloidal spintronics through Rashba spin-orbit interaction in lead sulphide nanosheets. *Nature Communications* **8**, 15721 (2017).

98 Murph, S. E. H., Coopersmith, K. J. & Larsen, G. K. *Anisotropic and Shape-Selective Nanomaterials* 7-28 (Springer, 2017).

99 Di Bernardo, A. *et al.* p-wave triggered superconductivity in single-layer graphene on an electron-doped oxide superconductor. *Nature communications* **8**, 14024 (2017).

100 Xiu, F. *et al.* Manipulating surface states in topological insulator nanoribbons. *Nature nanotechnology* **6**, 216 (2011).

101 Grassian, V. H. When size really matters: size-dependent properties and surface chemistry of metal and metal oxide nanoparticles in gas and liquid phase environments. *The Journal of Physical Chemistry C* **112**, 18303-18313 (2008).

102 Franke, M. E., Koplin, T. J. & Simon, U. Metal and metal oxide nanoparticles in chemiresistors: does the nanoscale matter? *Small* **2**, 36-50 (2006).

103 Gadenne, P., Yagil, Y. & Deutscher, G. Transmittance and reflectance insitu measurements of semicontinuous gold films during deposition. *Journal of applied physics* **66**, 3019-3025 (1989).

104 Plass, R., Pelet, S., Krueger, J., Grätzel, M. & Bach, U. Quantum dot sensitization of organic–inorganic hybrid solar cells. *The Journal of Physical Chemistry B* **106**, 7578-7580 (2002).

105 Jiu, J. & Suganuma, K. Metallic Nanowires and Their Application. *IEEE Transactions on Components, Packaging and Manufacturing Technology* **6**, 1733-1751 (2016).

106 Lin, J. *et al.* Flexible metallic nanowires with self-adaptive contacts to semiconducting transition-metal dichalcogenide monolayers. *Nature nanotechnology* **9**, 436 (2014).

107 Loc, W. S. *et al.* Facet-controlled facilitation of PbS nanoarchitectures by understanding nanocrystal growth. *Nanoscale* **7**, 19047-19052 (2015).

108 Giraud, P. *et al.* Field effect transistors and phototransistors based upon p-type solution-processed PbS nanowires. *Nanotechnology* **29**, 075202 (2018).

109 Lu, W., Gao, P., Jian, W. B., Wang, Z. L. & Fang, J. Perfect orientation ordered in-situ one-dimensional self-assembly of Mn-doped PbSe nanocrystals. *Journal of the American Chemical Society* **126**, 14816-14821 (2004).

110 Beecher, A. N. *et al.* Atomic structures and gram scale synthesis of three tetrahedral quantum dots. *Journal of the American Chemical Society* **136**, 10645-10653 (2014).

111 Choi, H., Ko, J.-H., Kim, Y.-H. & Jeong, S. Steric-hindrance-driven shape transition in PbS quantum dots: understanding size-dependent stability. *Journal of the American Chemical Society* **135**, 5278-5281 (2013).

112 Ko, J.-H., Yoo, D. & Kim, Y.-H. Atomic models for anionic ligand passivation of cation-rich surfaces of IV–VI, II–VI, and III–V colloidal quantum dots. *Chemical Communications* **53**, 388-391 (2017).

113 Kim, K. *et al.* Halide–Amine Co-Passivated Indium Phosphide Colloidal Quantum Dots in Tetrahedral Shape. *Angewandte Chemie International Edition* **55**, 3714-3718 (2016).

114 Pintilie, L., Pentia, E., Matei, I., Pintilie, I. & Ozbay, E. Field-effect-assisted photoconductivity in PbS films deposited on silicon dioxide. *Journal of applied physics* **91**, 5782-5786 (2002).

115 Konstantatos, G. & Sargent, E. H. PbS colloidal quantum dot photoconductive photodetectors: Transport, traps, and gain. *Applied Physics Letters* **91**, 173505 (2007).

116 Klinke, C., Hannon, J. B., Afzali, A. & Avouris, P. Field-effect transistors assembled from functionalized carbon nanotubes. *Nano letters* **6**, 906-910 (2006).

117 Bid, A., Bora, A. & Raychaudhuri, A. Temperature dependence of the resistance of metallic nanowires of diameter$\geqslant$ 15 nm: Applicability of Bloch-Grüneisen theorem. *Physical Review B* **74**, 035426 (2006).

118 Pridmore, D. & Shuey, R. The electrical resistivity of galena, pyrite, and chalcopyrite. *American Mineralogist* **61**, 248-259 (1976).

119 Michotte, S., Mátéfi-Tempfli, S. & Piraux, L. 1D-transport properties of single superconducting lead nanowires. *Physica C: Superconductivity* **391**, 369-375 (2003).

120 Eom, D., Qin, S., Chou, M.-Y. & Shih, C. Persistent superconductivity in ultrathin Pb films: A scanning tunneling spectroscopy study. *Physical review letters* **96**, 027005 (2006).

121 Bao, X.-Y. *et al.* Quantum size effects on the perpendicular upper critical field in ultrathin lead films. *Physical review letters* **95**, 247005 (2005).

122 Michotte, S. *et al.* Superconducting properties of lead nanowires arrays. *Physica C: Superconductivity* **377**, 267-276 (2002).

123 Yuan, L. *et al.* Air-stable PbS quantum dots synthesized with slow reaction kinetics via a PbBr 2 precursor. *RSC Advances* **5**, 68579-68586 (2015).

124 Pantea, D., Darmstadt, H., Kaliaguine, S. & Roy, C. Electrical conductivity of conductive carbon blacks: influence of surface chemistry and topology. *Applied Surface Science* **217**, 181-193 (2003).

125 Doniach, S. & Sunjic, M. Many-electron singularity in X-ray photoemission and X-ray line spectra from metals. *Journal of Physics C: Solid State Physics* **3**, 285 (1970).

126 Ramin Moayed, M. M., Bielewicz, T., Zoellner, M., Herrmann, C. & Klinke, C. Rashba Spin-Orbit Coupling in Colloidal Lead Sulfide Nanosheets. *Novel Optical Materials and Applications. Advanced Photonics 2017*, OSA Technical Digest NoTu1C. 3 (Optical Society of America) (2017).

127 Stierle, A., Keller, T. F., Noei, H., Vonk, V. & Roehlsberger, R. DESY NanoLab. *Journal of large-scale research facilities JLSRF* **2**, 76 (2016).

Appendix

A1 Online available “Supporting Information”

Copyright WILEY-VCH Verlag GmbH & Co. KGaA, 69469 Weinheim, Germany, 2018.

ADVANCED FUNCTIONAL MATERIALS

Supporting Information

for *Adv. Funct. Mater.,* DOI: 10.1002/adfm.201706815

High-Performance n- and p-Type Field-Effect Transistors Based on Hybridly Surface-Passivated Colloidal PbS Nanosheets

*Mohammad Mehdi Ramin Moayed, Thomas Bielewicz, Heshmat Noei, Andreas Stierle, and Christian Klinke**

Supporting Information

High Performance n- and p-Type Field-Effect Transistors Based on Hybridly Surface-Passivated Colloidal PbS Nanosheets

Mohammad Mehdi Ramin Moayed, Thomas Bielewicz,
*Heshmat Noei, Andreas Stierle, Christian Klinke**

M. M. Ramin Moayed, Dr. T. Bielewicz, Prof. Dr. C. Klinke
Institute of Physical Chemistry, University of Hamburg, 20146 Hamburg, Germany

Dr. H. Noei, Prof. A. Stierle
DESY NanoLab, Deutsches Elektronensynchrotron DESY, 22607 Hamburg, Germany

Prof. A. Stierle
Physics Department, University of Hamburg, 20355 Hamburg, Germany

Prof. Dr. C. Klinke
Department of Chemistry, Swansea University - Singleton Park, Swansea SA2 8PP, UK

*Correspondence to: christian.klinke@swansea.ac.uk

Keywords: Colloidal synthesis, Nanosheets, Hybrid surface passivation, High performance field-effect transistors, Lead sulfide

1. TEM image of the sheets

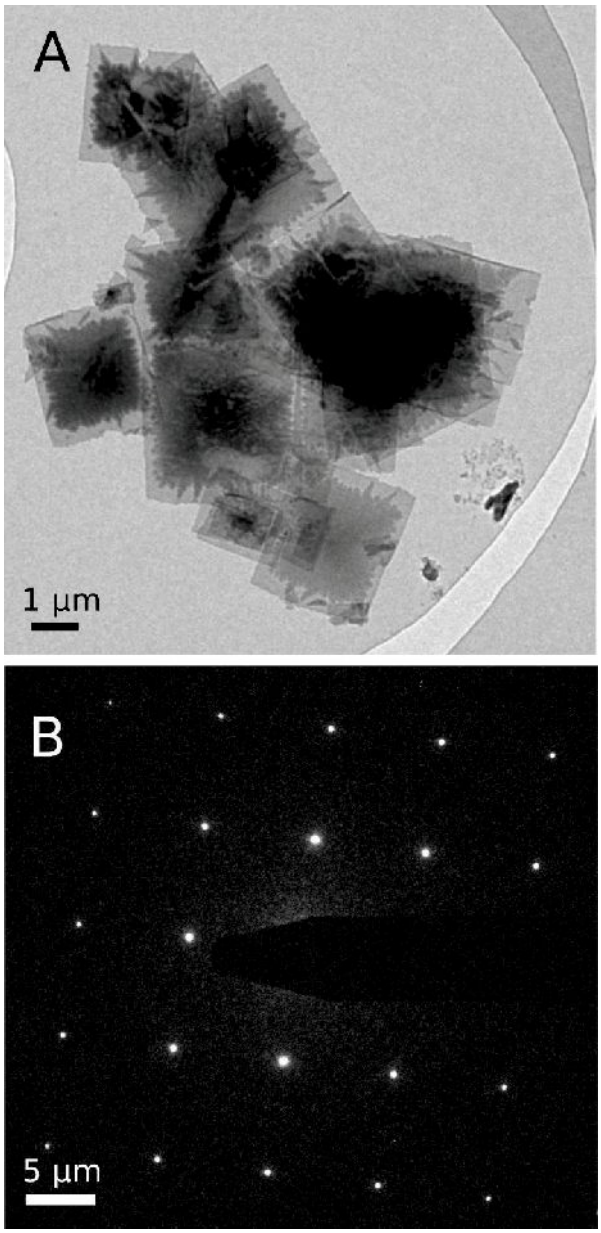

Figure S1. Transmission-electron microscopy (TEM) of the sheets. (A) TEM image of the nanosheets passivated by the high amount of Cl^-, as an exemplary demonstration of the sheets. (B) Electron-diffraction pattern of a single sheet, which shows that they are monocrystalline.

2. XRD data

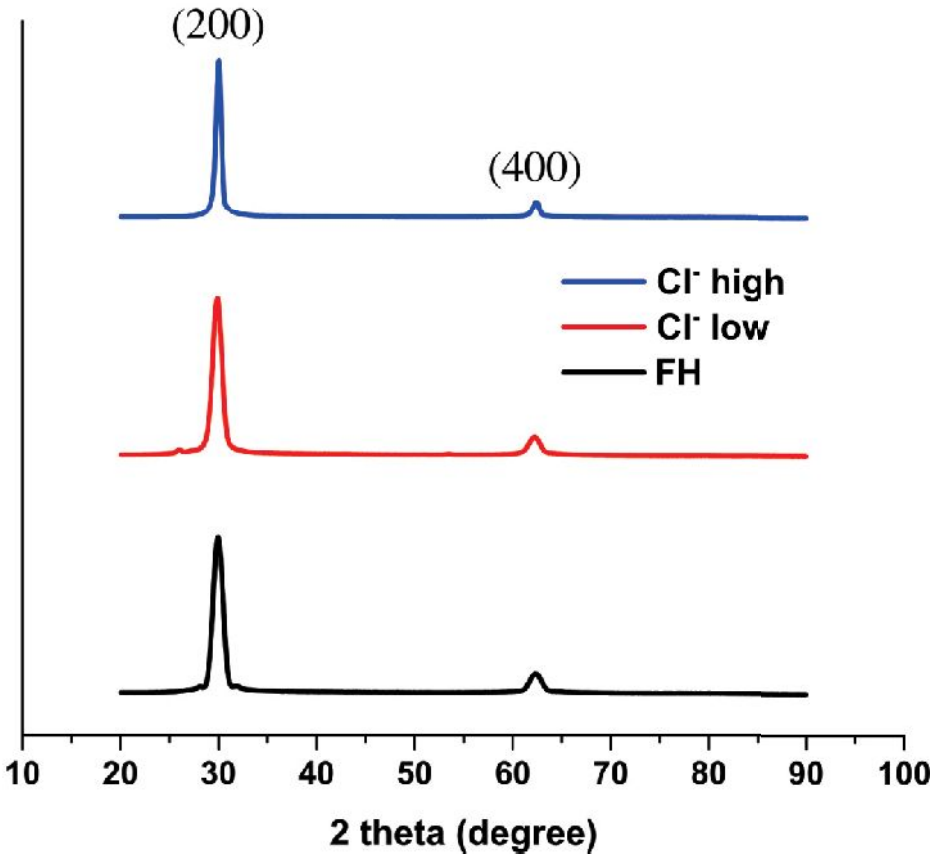

Figure S2. X-ray powder diffraction (XRD) of the samples, passivated with different coligands, which only show the (200) and (400) planes due to texture effects. Comparable broadening of the peaks shows the comparable thickness of the nanosheets.

3. Pb 4f (XPS) peaks for the sample made with FH

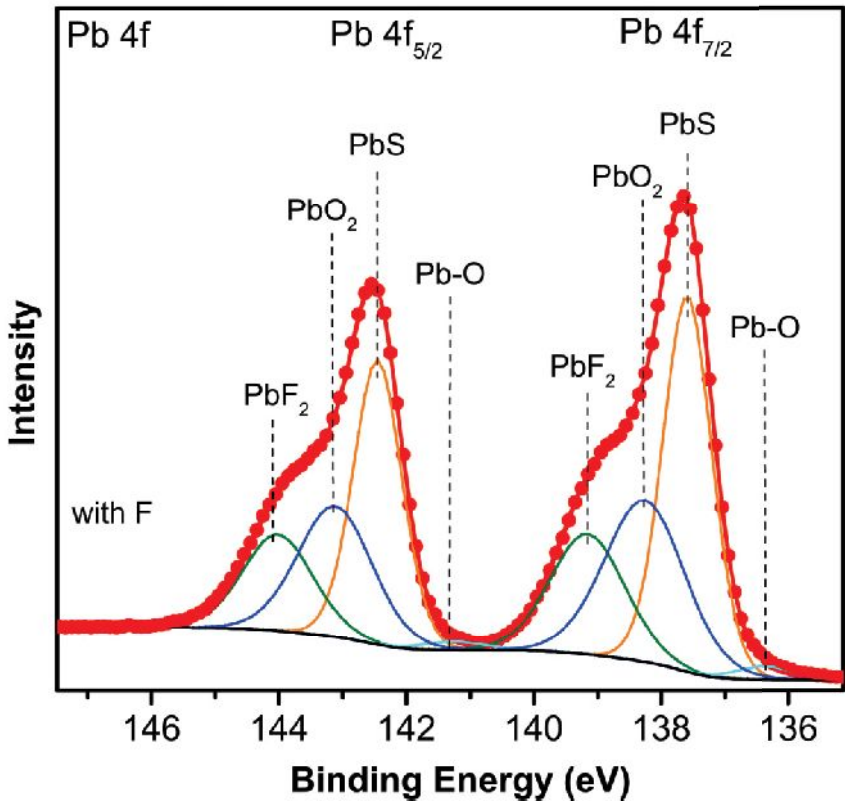

Figure S3. Deconvoluted XPS spectra of the FH-based samples for the Pb 4f region. XPS measurements show small amounts of F^- on the surface of the nanosheets. However, since F can be easily removed from the surface, it is not able to effectively passivate the defects and therefore, poor electrical properties are achieved with these sheets. Here, the Pb 4f peaks centered at 137.6 eV and 142.4 eV are attributed to the binding energy of Pb 4f 7/2 and Pb 4f 5/2 of PbS, respectively. The XPS peaks at 139.2 eV and 144 eV are assigned to Pb 4f 7/2 and Pb 4f 5/2 of Pb^{2+} in PbF_2. Eventually, the peaks at 138.2 eV, 143.1 eV, 136.9, and 141.7 are designated to Pb 4f 7/2 and Pb 4f 5/2 of PbO_2 and PbO respectively

4. SEM image of the device with the stripes

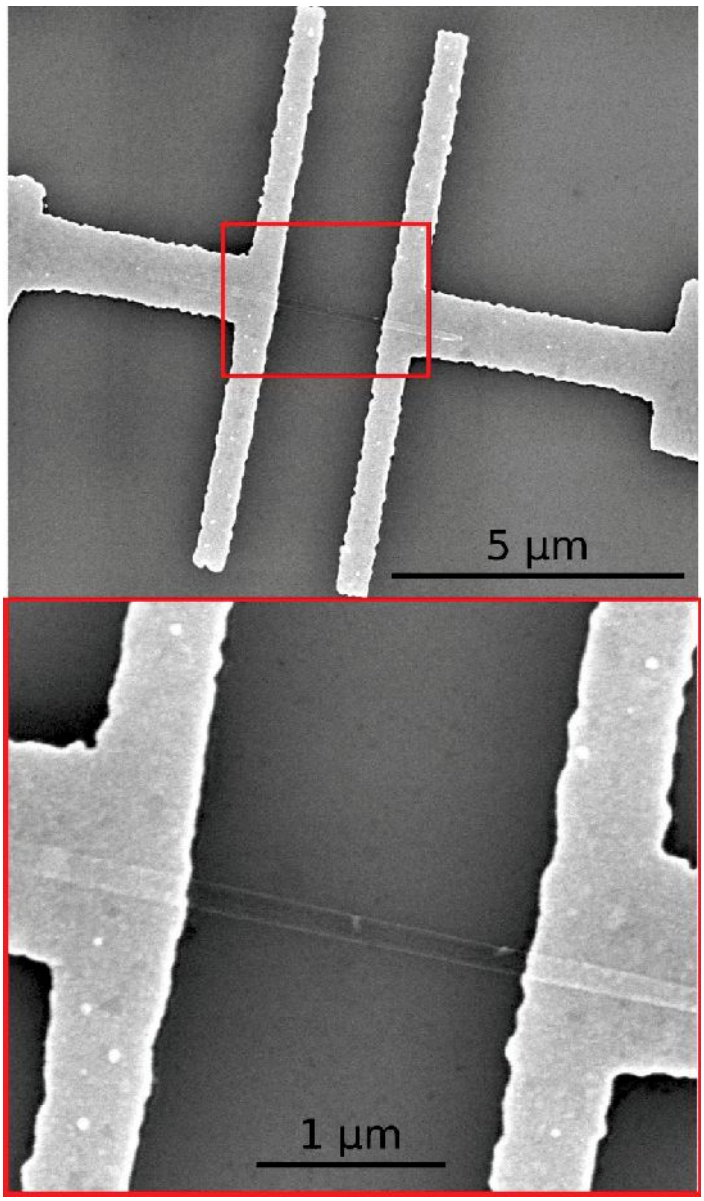

Figure S4. SEM image of the devices made by the narrow stripes. By reducing the channel width to 100 nm, better switching can be achieved.

5. FET measurements of the square nanosheets in air

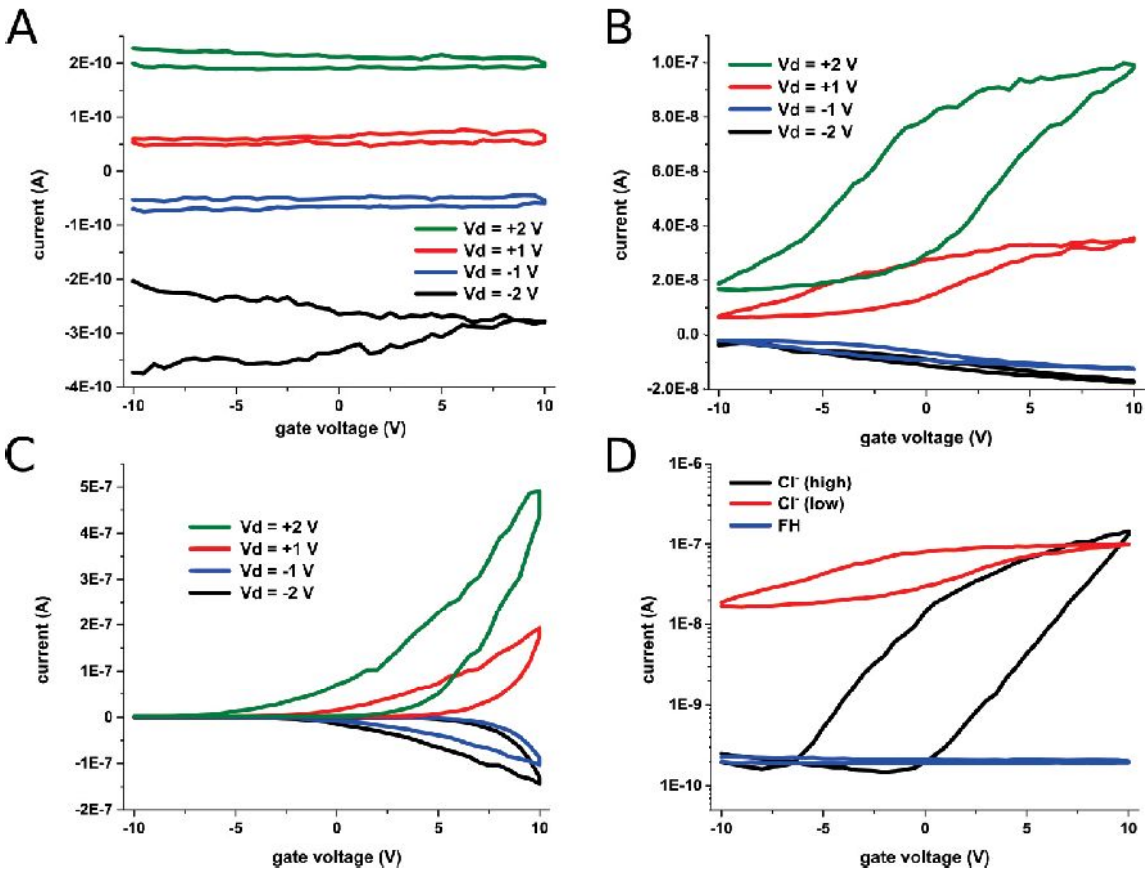

Figure S5. Transfer characteristics of the samples measured in air. (a) The fluoroalkane-based sample (field-effect mobility: 3.3×10^{-4} $cm^2V^{-1}s^{-1}$). (b) The sample passivated with the low amount of Cl^- (field-effect mobility: 0.1 $cm^2V^{-1}s^{-1}$, on/off ratio: 6). (c) The sample with the high amount of Cl^- (field-effect mobility: 2.5 $cm^2V^{-1}s^{-1}$, on/off ratio: 1000). (d) Comparison between the transfer characteristics of all the samples. Although clear improvements can be observed by intensifying the surface passivation (similar to the vacuum measurements), all the samples show weaker n-type behavior when air is introduced to them. This is in agreement with the archived results for the strips.

6. FET measurements of the square nanosheets contacted with Au

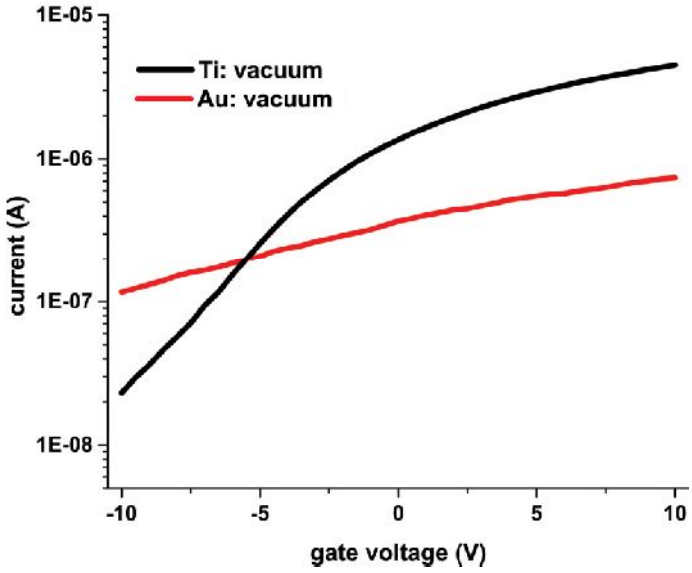

Figure S6. Variation of the transfer characteristics of the square sheets (bias voltage: 1 V), passivated by the high amount of Cl^-, by changing the contact metal (Ti or Au). Comparable to the stripes, the n-type behavior is weakened by using Au as the contact metal (for the Au-contacted device: field-effect mobility: 1.3 $cm^2V^{-1}s^{-1}$, on/off ratio: 6).

Supplementary Figures

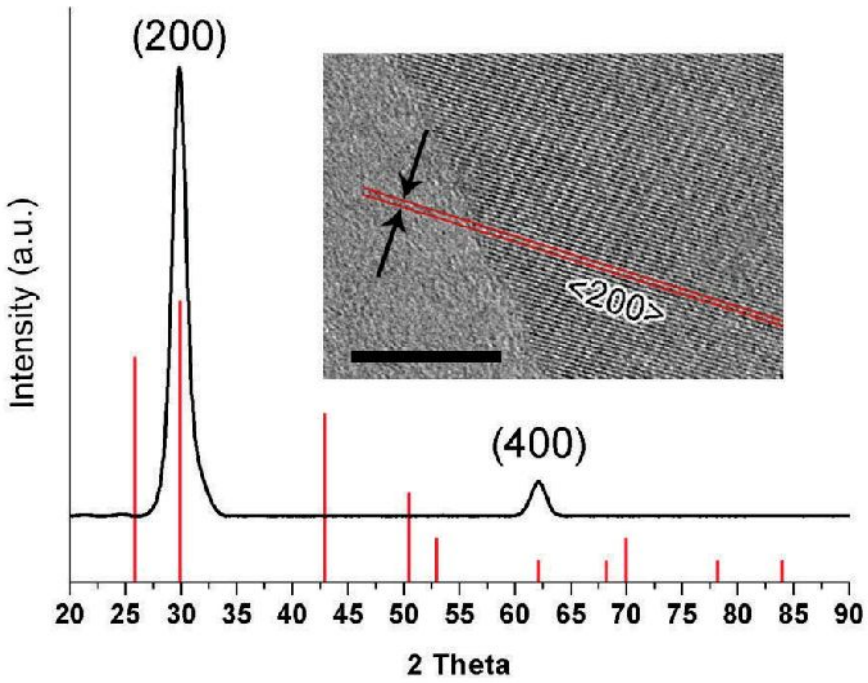

Supplementary Figure 1 | Crystallography of the lead sulfide nanosheets.

X-ray powder diffraction of PbS nanosheets shows only the (200) and (400) planes due to texture effects. The peaks for bulk *galena* are shown in red (JCPDS 5–592: *galena*). The *d*-spacing for the (200) bulk PbS plane is $d = 0.2969$ nm (JCPDS 5–592: *galena*) while the measured *d*-spacing in the high resolution tunnelling-electron microscope (HRTEM) inlet of the (200) nanosheet plane (red lines enclosed by the black arrows) is $d = 0.302 \pm 0.02$. The scale bar is equal to 10 nm.

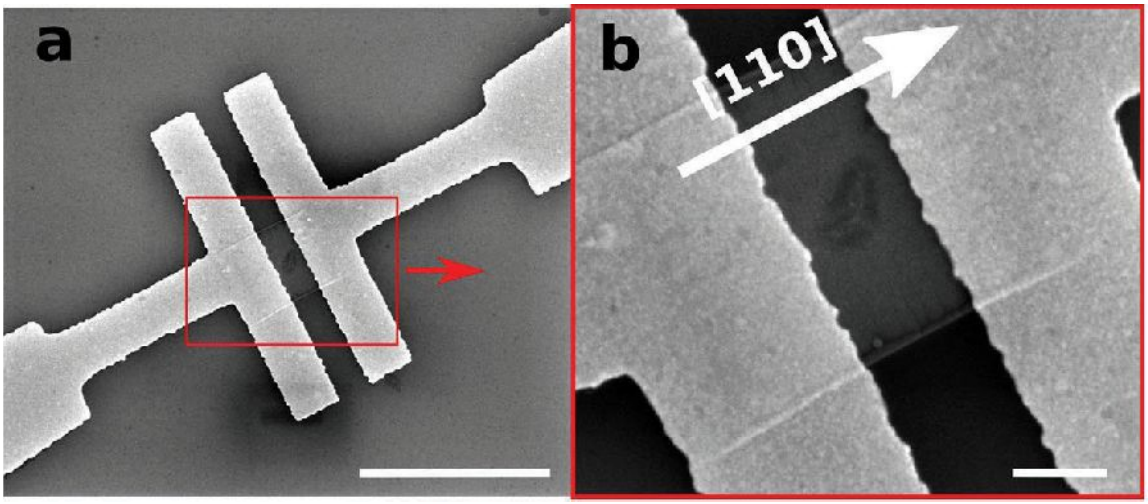

Supplementary Figure 2 | Scanning-electron microscope image of a device based on an individual nanosheet.

a, An SEM image of an individually contacted nanosheet. The scale bar is 4 μm. The nanosheets with thickness of 6, 9 and 18 nm were distributed on the Si/SiO_2 substrate and contacted by Ti/Au by means of electron-beam lithography. **b**, The magnified image of the same device (the scale bar is 500 nm). The current flow for these nanosheets is in [110] direction.

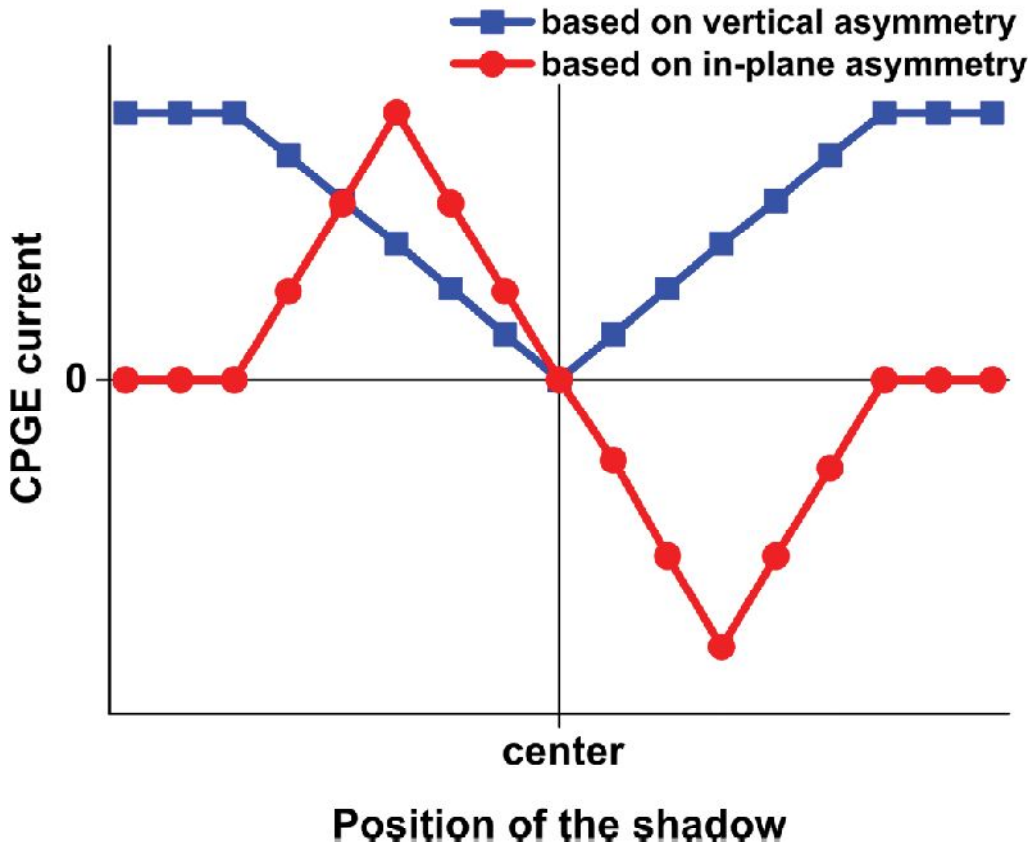

Supplementary Figure 3 | Ideal contribution of vertical and in-plane asymmetry in circular photo-galvanic effect.

If only an in-plane asymmetry is considered, by shadowing the device, the CPGE current experiences a sign change, when the asymmetry is reversed, but the magnitude of the current remains constant. In case of the vertical asymmetry, shadowing leads to a decrease of the CPGE current without changing the sign, since the direction of the asymmetry is constant and the effective part of the crystal for the current generation is reduced. The combination of both effects results in CPGE in PbS nanosheets, while the contribution of each part can be altered by the incidence angle.

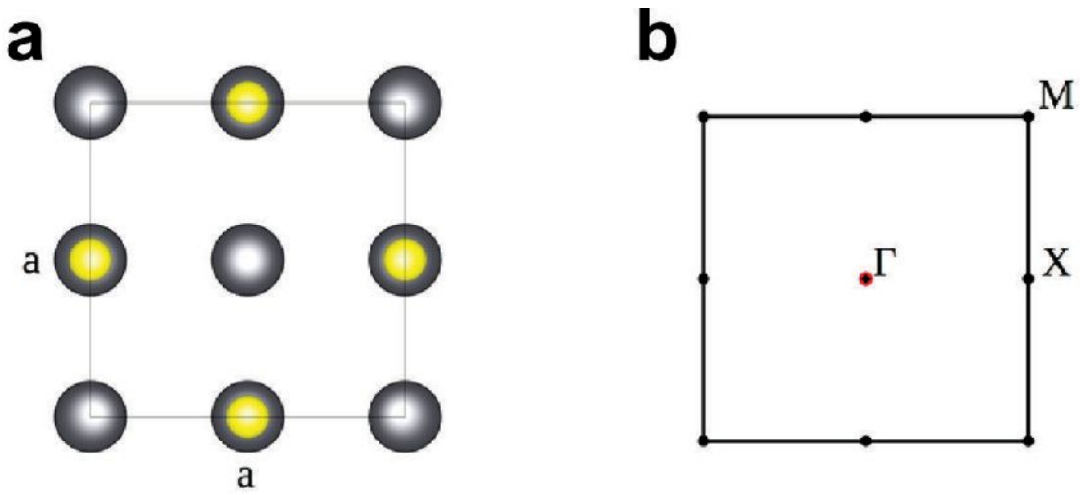

Supplementary Figure 4 | Used unit cell and the corresponding Brillouin zone.

a, The used unit cell during the calculations where *a* denotes the lattice constant and the circles show lead and sulphur atoms. **b**, The corresponding Brillouin zone is shown. The band structure was calculated along the Γ-M-X path and around to the band gap (M Point).

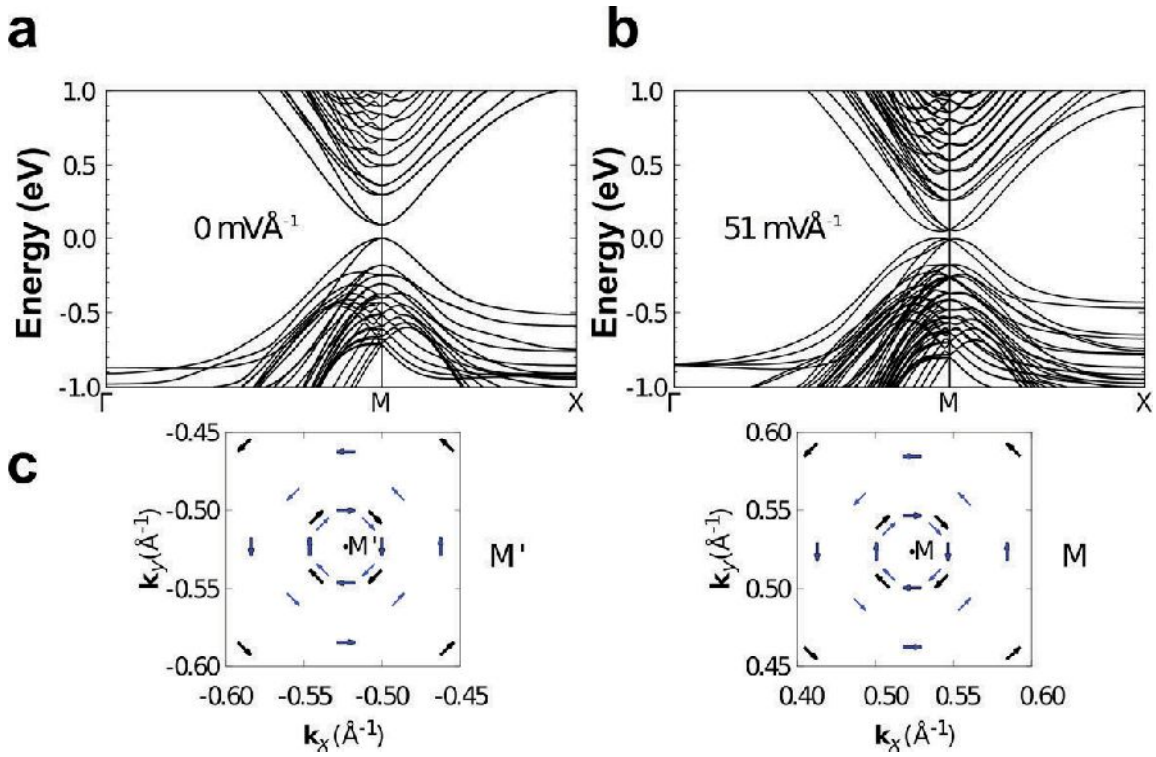

Supplementary Figure 5 | Band structure of lead sulfide nanosheets with Rashba splitting.

a, Without an external electric field, the band structure does not show Rashba-spin splitting along the Γ-M-X path. **b,** With an external electric field, (strength: 51 mVÅ^{-1}) Rashba-spin splitting occurs at the M point in the valence band as well as in the conduction band. The valence-band maximum was set to 0 eV. **c,** Spin texture of the two highest valence bands, 0.044 eV below the valence-band maximum (black: highest filled band, blue: second highest filled band) at the M (right) and the M' point (left). A typical spin texture for Rashba-spin splitting can be observed[1]. The length of the arrows is normalized. Along the Γ-M path, the highest and second highest filled bands split in energy, while along the M-X path, they do not.

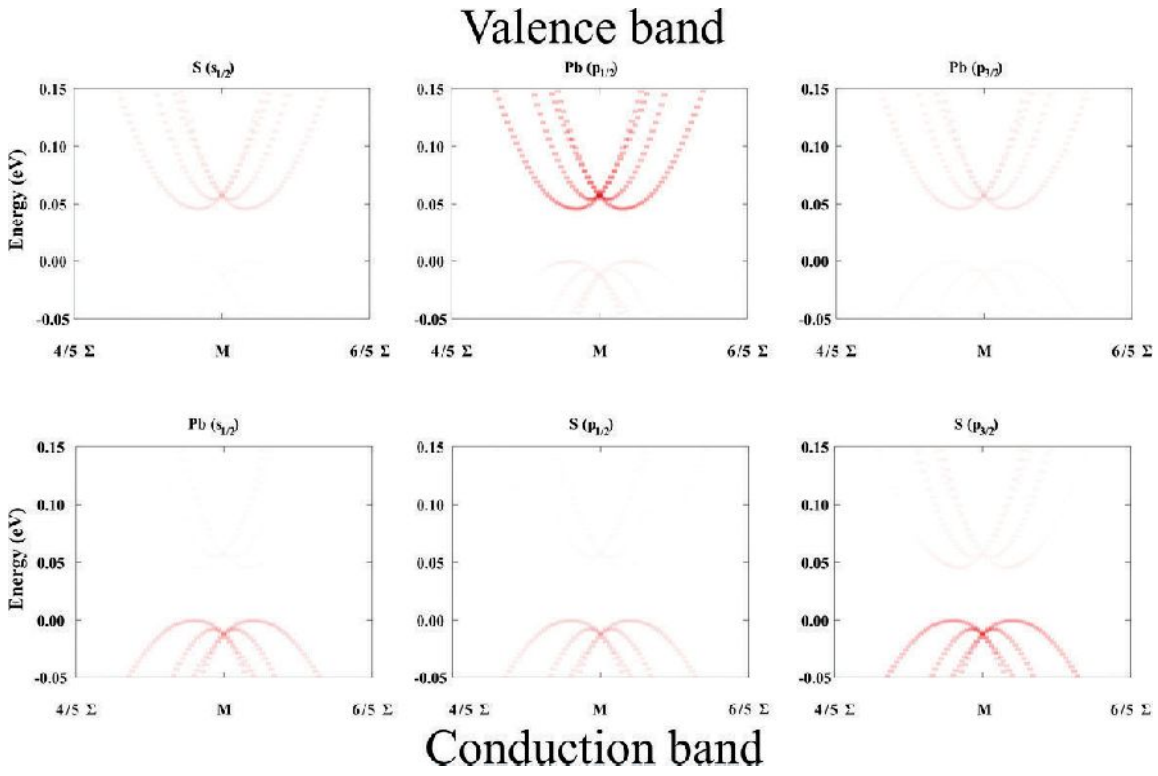

Supplementary Figure 6 | Projected density of states resolved on several k-points in the vicinity of the band gap.

The projected density of states was summed over all atoms for the corresponding orbital (E=51 mVÅ^{-1}). The valence band predominantly consists of the $p_{3/2}$ orbitals of sulphur (S), while the conduction band mainly consists of the $p_{1/2}$ orbitals of lead (Pb). The intensity of the colour implies the strength of the contribution of the corresponding orbital.

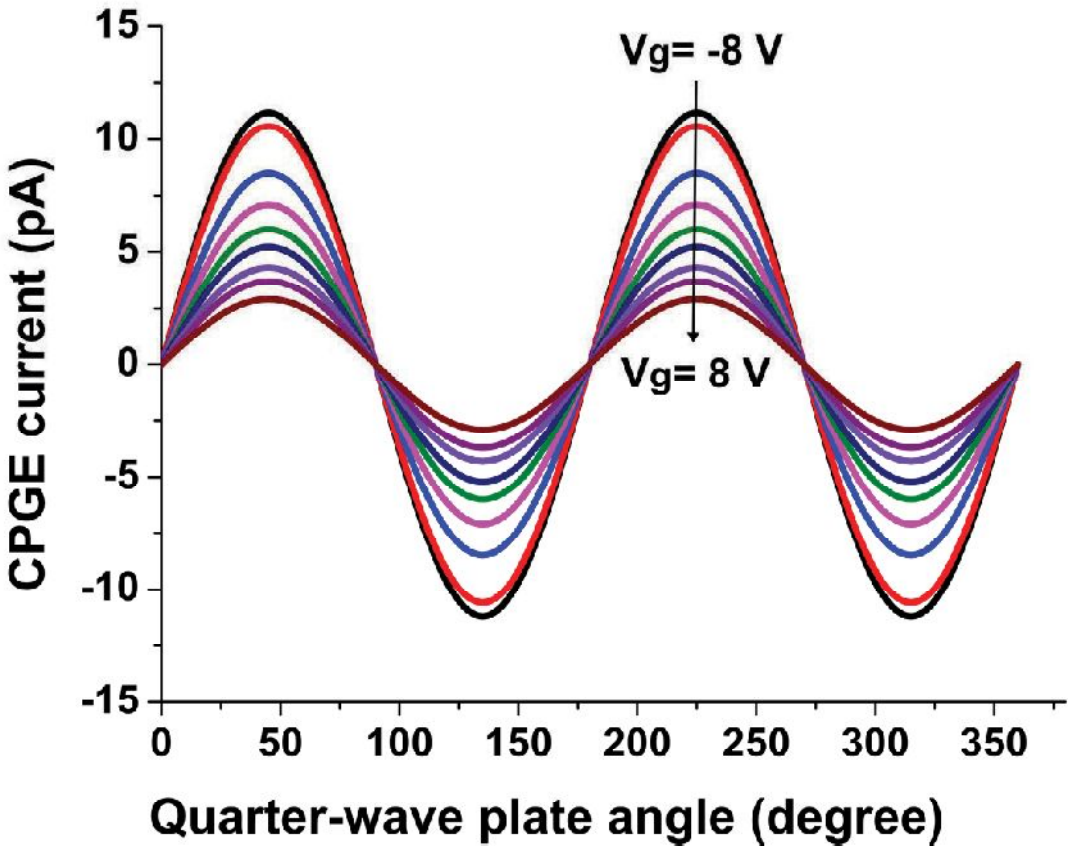

Supplementary Figure 7 | Extracted gate dependency for the magnitude of the circular photo-galvanic current.

By decreasing the back-gate voltage from 8 V to -8 V (in steps of 2 V), the absolute magnitude of the generated CPGE can be increased. Modification of the bands splitting as well as the recombination rate is the reason for such a tendency. By altering the angle of the quarter-wave plate, oscillations with period of 180° are detected.

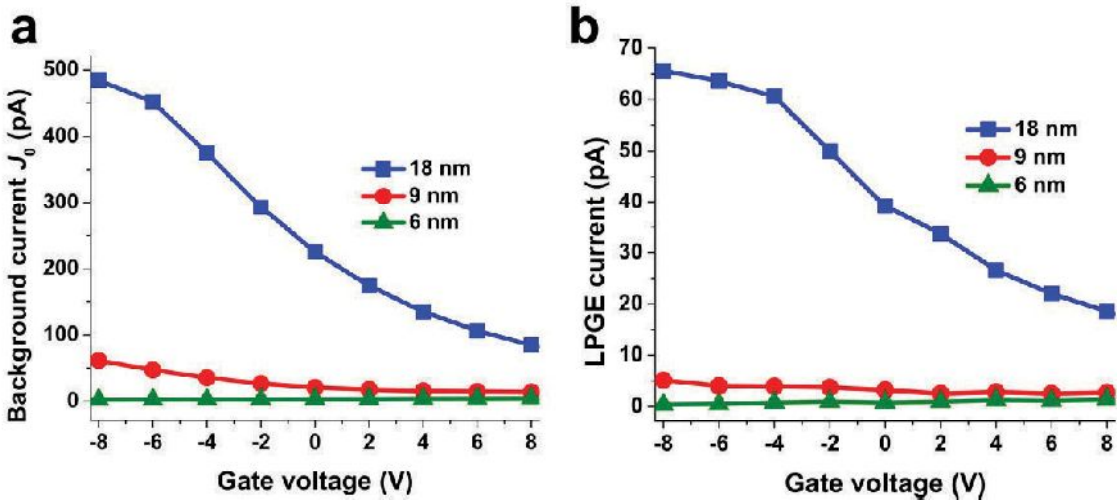

Supplementary Figure 8 | Spin-independent properties of the nanosheets with different thicknesses.

a, Background current J_0 for the investigated devices as a function of the back-gate voltage. Larger channel sizes as well as smaller band gaps for thicker sheets can lead to the generation of higher background currents. Modification of the band alignment by changing the gate voltage also tunes the background current for each thickness. **b,** Variation of the linear photo-galvanic (LPGE) current by changing the nanosheet thickness. By changing the circular polarization of the light, the spin-independent photocurrent can be modulated. Comparable with the background current, this component can be also tuned by the thickness or by the back-gate voltage.

Supplementary References

1. Manchon, A., Koo, H. C., Nitta, J., Frolov, S. M., Duine, R. A., New perspectives for Rashba spin–orbit coupling. *Nature Materials* ***14***, 871–882 (2015).

A2 Supporting information: Tuning electrical properties of lead sulphide by sculpting the crystal

1- Synthesis of PbS Stripes

Different types of lead sulphide nanowires were synthesized as followed. In a three-neck-flask with thermocouple, condenser and septum 860 mg $PbO(Ac_2).3H_{20}$ (2.3 mmol), 3.5 mL oleic acid (11 mmol) and 10 mL Diphenylether are mixed and degassed at 70 °C in vacuum for at least 2.5 h. Under nitrogen atmosphere, 0.10 mL Trioctylphosphine (0.22 mmol) is added and the solution is heated up to 170-200 °C. While heating, 0.2 mL of a 0.3 M LiCl-DMF solution is added. When the reaction solution reaches the desired temperature, 0.2 mL of a 0.09 M TU-DMF solution is added. Then, the solution turns black and shows typical hazes. When the reaction solution reaches room temperature, it is centrifuged with 7 krpm for 5 min. The colorless supernatant is disposed and the black precipitate is washed two more times by dispersion in toluene and centrifugation as described before. The wires, which are stable for at least some weeks, are stored in toluene.

2- Device preparation and measurements

A diluted suspension of the wires was spin-coated on a Si/SiO_2 substrate, and contacted individually by electron-beam lithography, followed by thermal evaporation of 1/50 nm Ti/Au. The achieved devices were transferred to a probe station for room or low temperature electrical measurements in vacuum. All the measurements were carried out with back-gate geometry, using a highly doped silicon substrate with 300 nm thermal oxide as gate dielectric. For the illumination of the wires, a red laser (λ = 630 nm) with 20 mW power was used.

3- XPS measurements

X-ray photoelectron spectroscopy (XPS) measurements were carried out using a high-resolution 2D delay line detector. A monochromatic Al K α X-ray source (photon energy 1486.6 eV; anode operating at 15 kV) was used as incident radiation and, to compensate for charging effects, a flood gun was used. XPS spectra were recorded in fixed transmission mode. A pass energy of 20 eV was chosen, resulting in an overall energy resolution better than 0.4 eV. The binding energies were calibrated based on the graphitic carbon 1 s peak at 284.8 eV[127].

4- Formation of flat and zigzag shaped PbS wires

The first step in the synthesis of colloidal PbS wires is the thermal decomposition of Thiourea to sulphide ions and their precipitation to lead(II) sulphide in presence of lead(II) cations. The first PbS nuclei are probably truncated cuboctahedrons with expressed 110/100/111 facets. Oleic acid combined with a second ligand from the halogenated hydrocarbon family promotes the oriented attachment and the formation of NCs. Alternatively, halide ions can be employed instead of the halogenated hydrocarbons as the competing ligand to oleic acid. Oleic acid, the corresponding oleate and chloride ions bind to lead(II) cations, in order to passivate and stabilize the PbS nuclei. TOP must be also introduced to the synthesis to adjust the reactivity of the lead(II) cations. Without adding TOP, no wires are obtained, while increasing the amount of TOP leads to the formation of longer wires and more nanoparticles as byproduct. The color change (the formation of the product) is delayed from 15 s to 60 s when the amount of TOP is 10 times higher. Beside the reactivity of the lead(II) cations, TOP might also act as a ligand.

The important step in the formation of the wires is the oriented attachment of previously formed nuclei to 1D wires. The amount of chloride ions in the synthesis is crucial to determine the dimensionality of the product. With high amounts of chloride ions, nanoparticles are obtained since the oriented attachment is prevented by strongly passivating chloride ligands. On the other hand, with less chloride, 2D nanosheets are formed. By introducing a proper amount of Cl^- ions, for instance 200 µL LiCl, zigzag and straight nanowires are obtained. Aliquots, taken in the beginning of the synthesis (beginning the color change), show 10 nm thin wires of both types. They grow to thicker and wider wires with a width of approximately 30-50 nm.

By varying the synthesis, it was observed that the zigzag wires are formed at the state with a high concentration of monomers, while the flat ones are formed when the monomer concentration is lower. Dilution of the reaction solution by the factor of 2 or reducing the amount of sulfur precursor by the factor of 4, both result in the formation of mainly flat shaped wires (validated by XRD). On the other hand, increasing the concentration leads to the formation of bigger wires. Increasing the concentration of the sulfur precursor (4 times more) resulted in the formation of NPs with some wires as byproducts. In this condition, bulk XRD reflexes are obtained. So in summary, the concentration of precursors plays an important role and can be used to synthesize mainly flat shaped wires, but not to synthesize only zigzag wires.

The other important parameter is the amount of oleic acid, used in the synthesis (2mL vs. 3.5 mL). With 3.5 mL oleic acid, the ratio between oleate and free oleic acid is 0.72. This ratio increases significantly to 2.70 when the volume of oleic acid is reduced to 2.0 mL (since the amount of lead(II) oleate, formed in the first step of the synthesis remains unchanged). With more oleic acid, a faster growth of formed wires can be obtained. With 2.0 mL oleic acid, the formed wires are passivated against further growth, leading to thinner wires with less expressed 111 facets/zigzag shape. By increasing the amount of oleic acid, the wires grow larger, up to 200 nm in width, while no significant changes could be observed in the ratio between the number of zigzag wires to flat ones. In such a synthesis, oleic acid competes with oleate at the wires surface, leading to a weaker passivation and more growth. This is similar to the strategy which is used to tune the thickness of PbS nanosheets.

XRD data can be employed to investigate the composition of the product, since the wires lie differently on a substrate. Reflexes parallel to the zone axis are more pronounced in the powder XRD when the wires are drop casted from the solution. Therefore, a main reflex at 43° [220] should represent zigzag wires, while 26° [111] indicates flat wires. Nanoparticles should not contribute to the XRD signal as long as they are only side products. When mainly NPs are present, the XRD pattern of the bulk material is obtained.

With a short reaction time (15 or 90 seconds), more zigzag wires are produced, while an increase of the reaction time to 5 or 10 min leads to the growth of the absent facets (like {100} and {110}) and the transformation of their shape from zigzag to a wavy form.

To ensure that these wavy wires are the ripened form of the zigzag wires, a few parameters have been investigated. Their XRD mainly shows the reflex at 30° [200]. Also HRTEM indicates the {100} facet as their top facet. However, their growth direction is similar to the normal zigzag wires (100). Therefore, it can be implied that they are also made of the attached octahedra via their tips (the {100} facet). But the normal zigzag wires lie on their edges (the 110 zone axis) and the ripened zigzag wires lie on their tips (100 zone axis). This is possible since during the ripening process, the tips (the {100} facets) grow larger and the crystal can stably lie on it. The growth of these facets during ripening changes the shape from zigzag to wavy.

The temperature of the reaction influences the wires similar to the reaction time and leads to the growth of the absent facets. Nevertheless, it does not change the ratio between the zigzag and flat wires.

5- Temperature effect

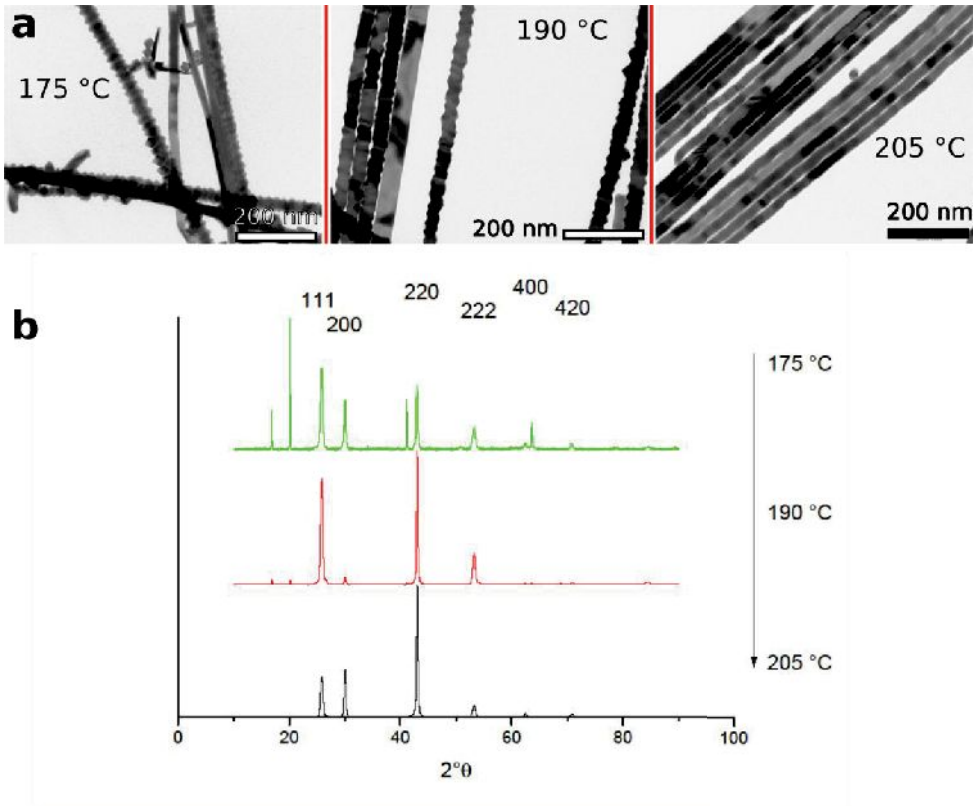

Figure S1. The effect of the synthesis temperature on the products. (a) TEM images of the wires produced with different temperatures. (b) XRD of the products. With increasing the reaction temperature the required time to observe the color change is shorter and the yield of the synthesis is higher. At 190 °C, a mixture of zigzag and flat shaped wires is produced. With 205 °C, mainly the ripened zigzag wires are achieved (their XRD signal is 110, representing zigzag wires).

6- The role of TOP

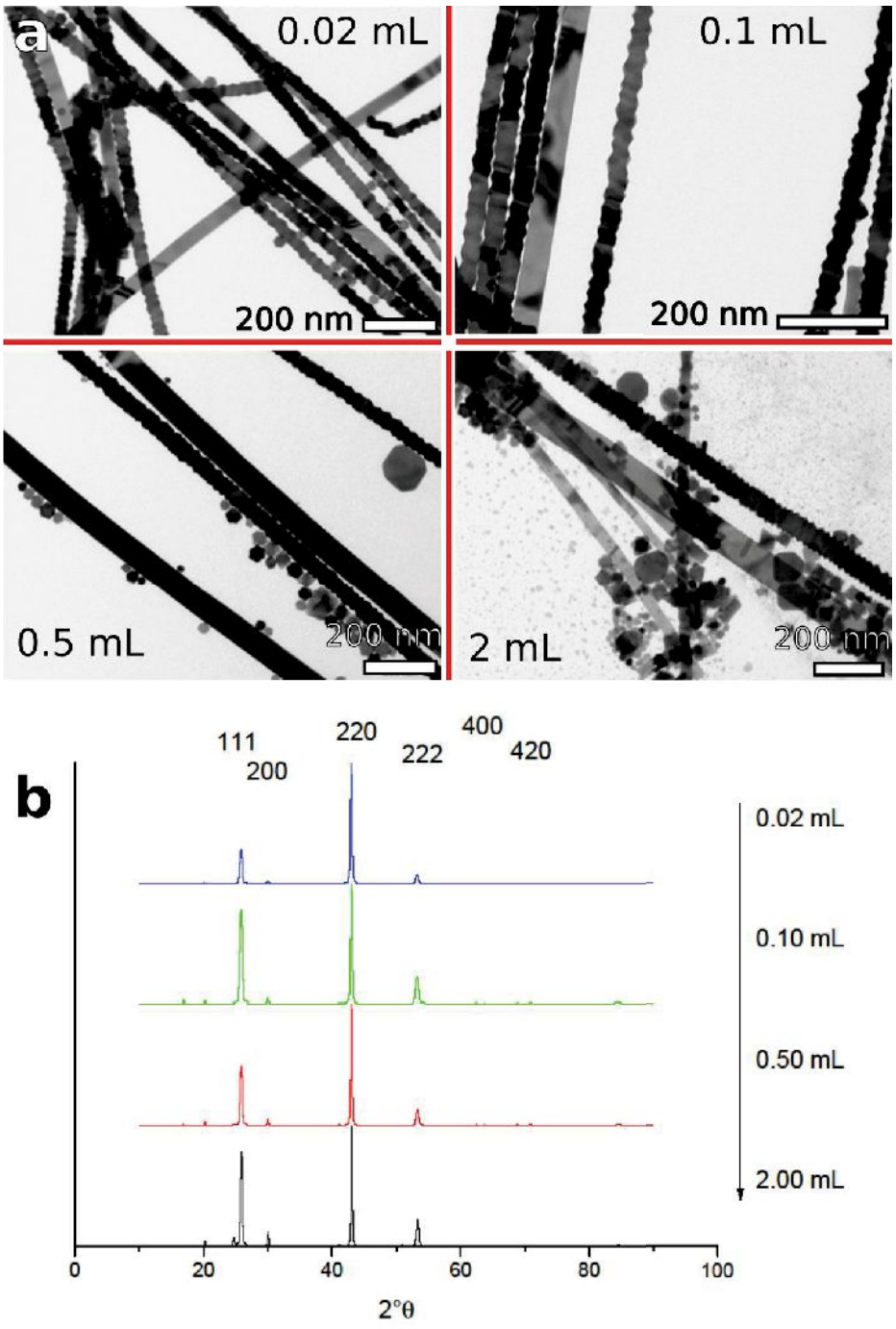

Figure S2. The effect of the TOP amount on the products. (a) TEM images of the wires produced with different amounts of TOP. (b) XRD of the products. With more TOP, more particles and "organic" residues are present in the samples. There seems to be also a slight change in zigzag/flat ratio to more flat ones. The change of the intensity of the 220 (representing zigzags) and 111

(representing flat) reflexes might be due to this change in the zigzag/flat ratio or by the appearance of octahedral particles oriented with the {111} facet on the substrate. Without TOP no wires are formed and only particles or undefined structures (depending on chloride ions) can be observed.

7- Reaction time

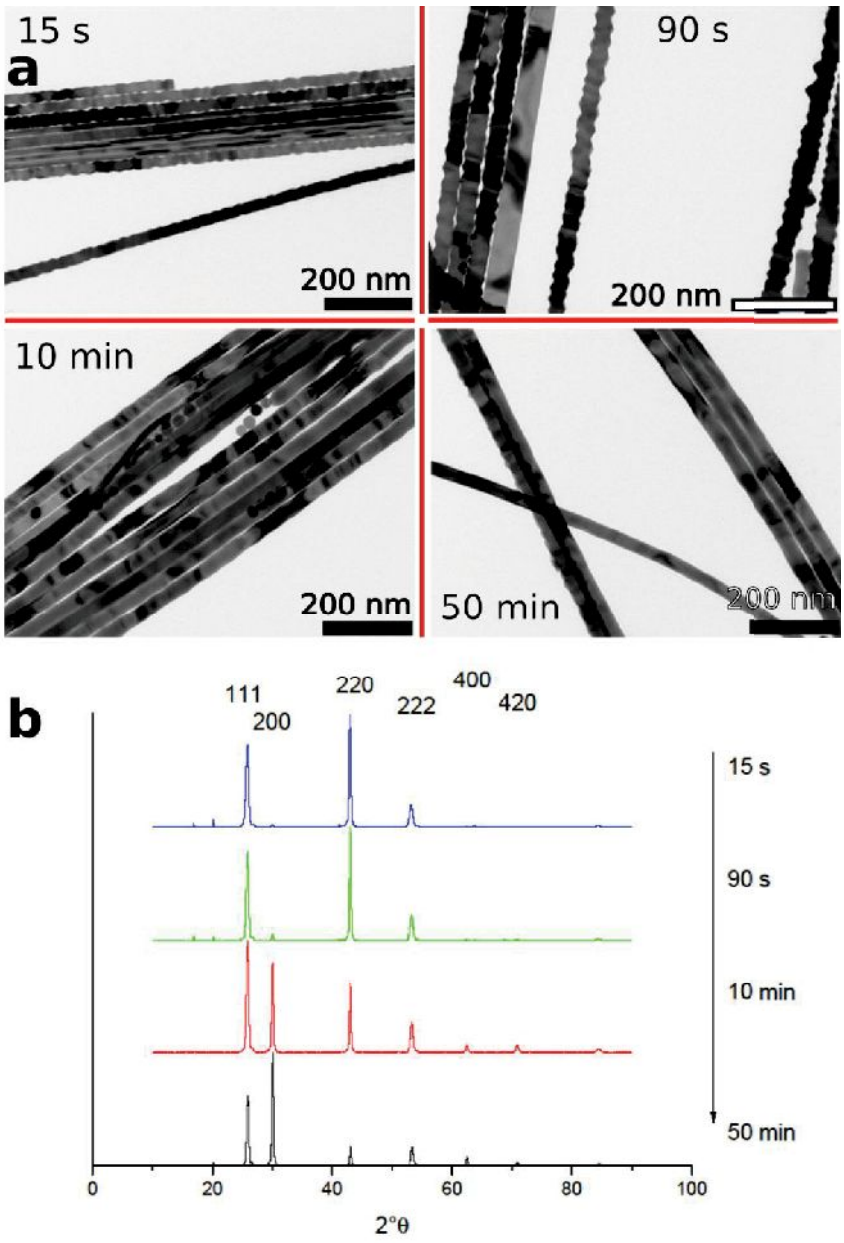

Figure S3. The effect of synthesis time on the products. (a) TEM images of the wires produced with different synthesis durations. (b) XRD of the products. With increasing the reaction time, more ripened zigzag wires (with a wavy surface) are produced, considering the less pronounced 220 reflex compared to 111 and a more pronounced 200 reflex.

8- Effect of oleic acid

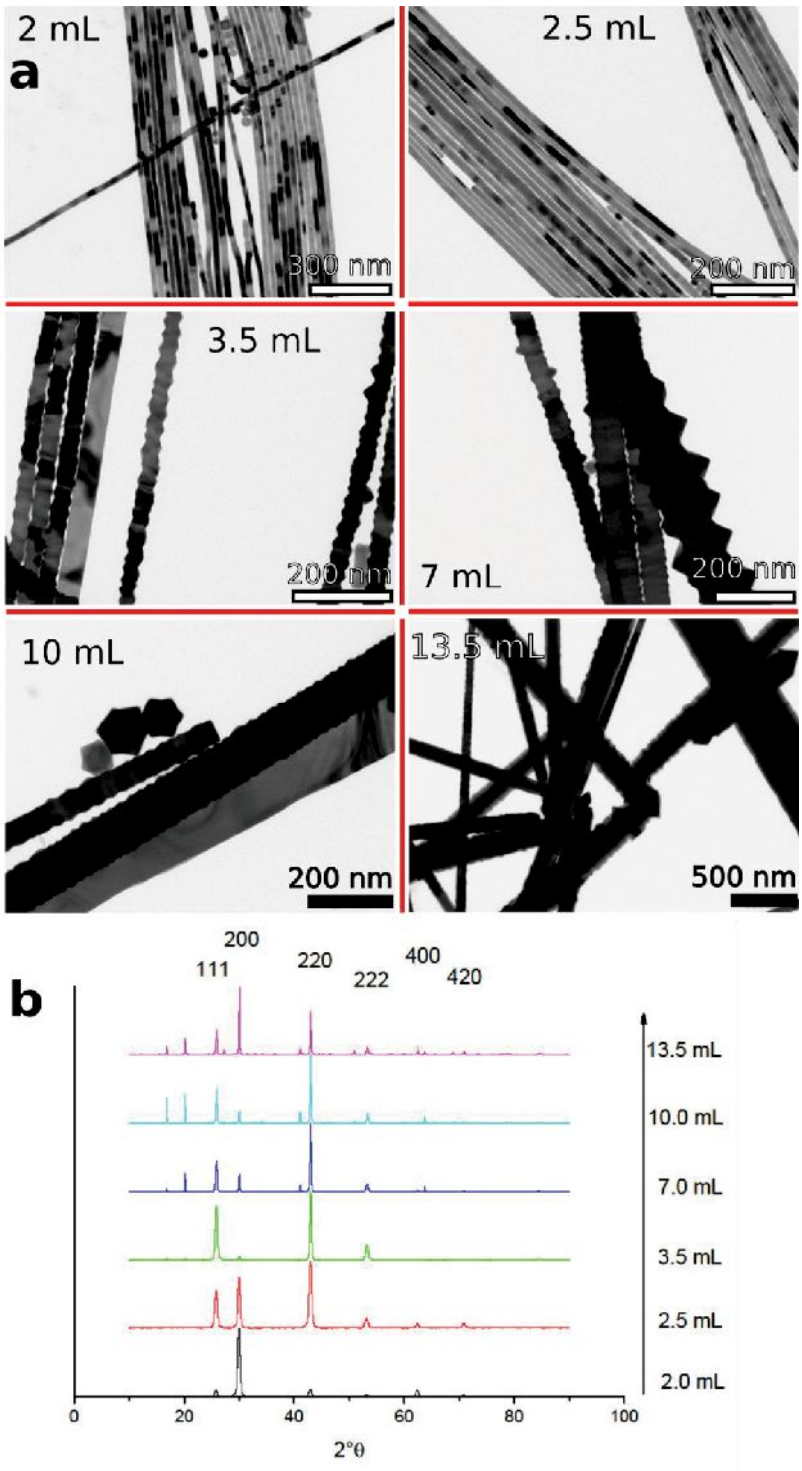

Figure S4. The effect of the oleic acid amount on the products. (a) TEM images of the wires produced with different amounts of oleic acid. (b) XRD of the products. Increasing the amount of oleic acid in the synthesis leads to an increased diameter of wires (higher contrast in TEM). The

particles which are always present in the synthesis are also bigger. This leads to the assumption that oleic acid controls the size of initial particles which attach to the wires via oriented attachment. A moderate amount of oleic acid (3.5 mL) results in a zigzag rich sample. Decreasing the amount of oleic acid to the minimum of 2 mL leads to mainly flat shaped wires. Increasing the amount of oleic acid still results in a mixture of both wires with up to several hundred nanometers in diameter. Oleic acid competes with oleate (which has a better passivating effect) on the surface, leading to an increased growth, when the ratio is changed to excess of free oleic acid.

9- Effect of Cl^- ions

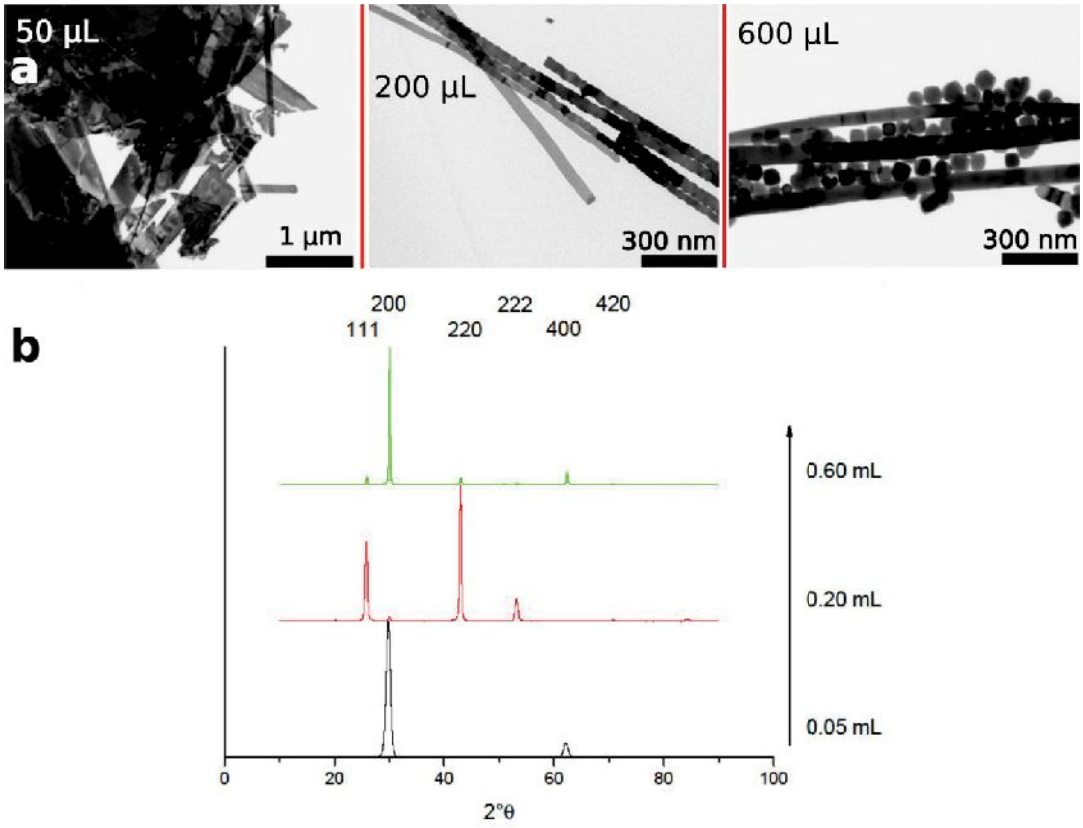

Figure S5. The effect of the Cl amount on the products. (a) TEM images of the wires produced with different amounts of Cl. (b) XRD of the products. With 200 µL LiCl solution (62 mg in 5 mL DMF) the standard product is achieved. By reducing the amount of chloride ions to one fourth, sheets are the main products with some flat stripes as a byproduct. Three times more chloride ions in the synthesis lead to some flat stripes with a lot of cubic shaped particles as a main product. In summary, the product of the synthesis is sheets with a low amount of chloride, stripes with a medium amount, and mainly particles or even precipitation of $PbCl_2$ with too much chloride.

10- Concentration of monomers (TU)

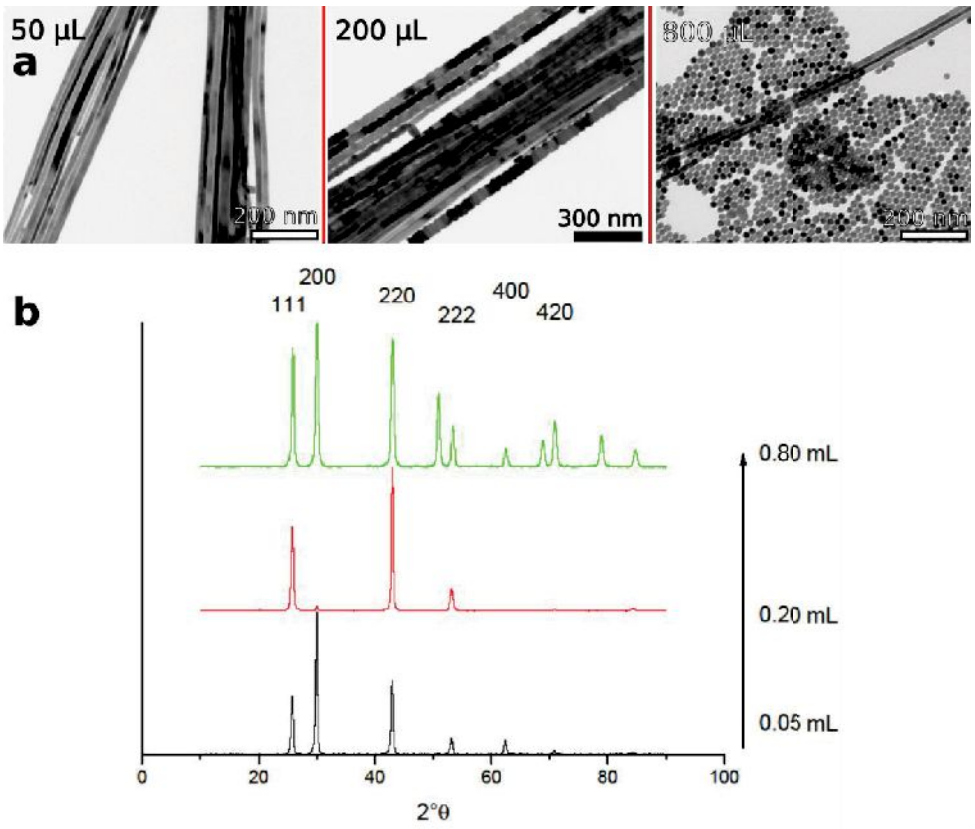

Figure S6. The effect of the monomers concentration on the products. (a) TEM images of the wires produced with different amounts of monomers. (b) XRD of the products. The standard volume of 200 µL of thiourea solution gives a Pb:S ratio of 138:1 resulting in mixture of flat and zigzag shaped PbS wires with a majority of zigzag shaped ones. By decreasing the amount of sulfur by the factor of 4, flat shaped wires are obtained as the main product. With the four times higher amount of sulfur, mainly nanoparticles are formed with some flat shaped wires as the byproduct.

11- Amount of solvent

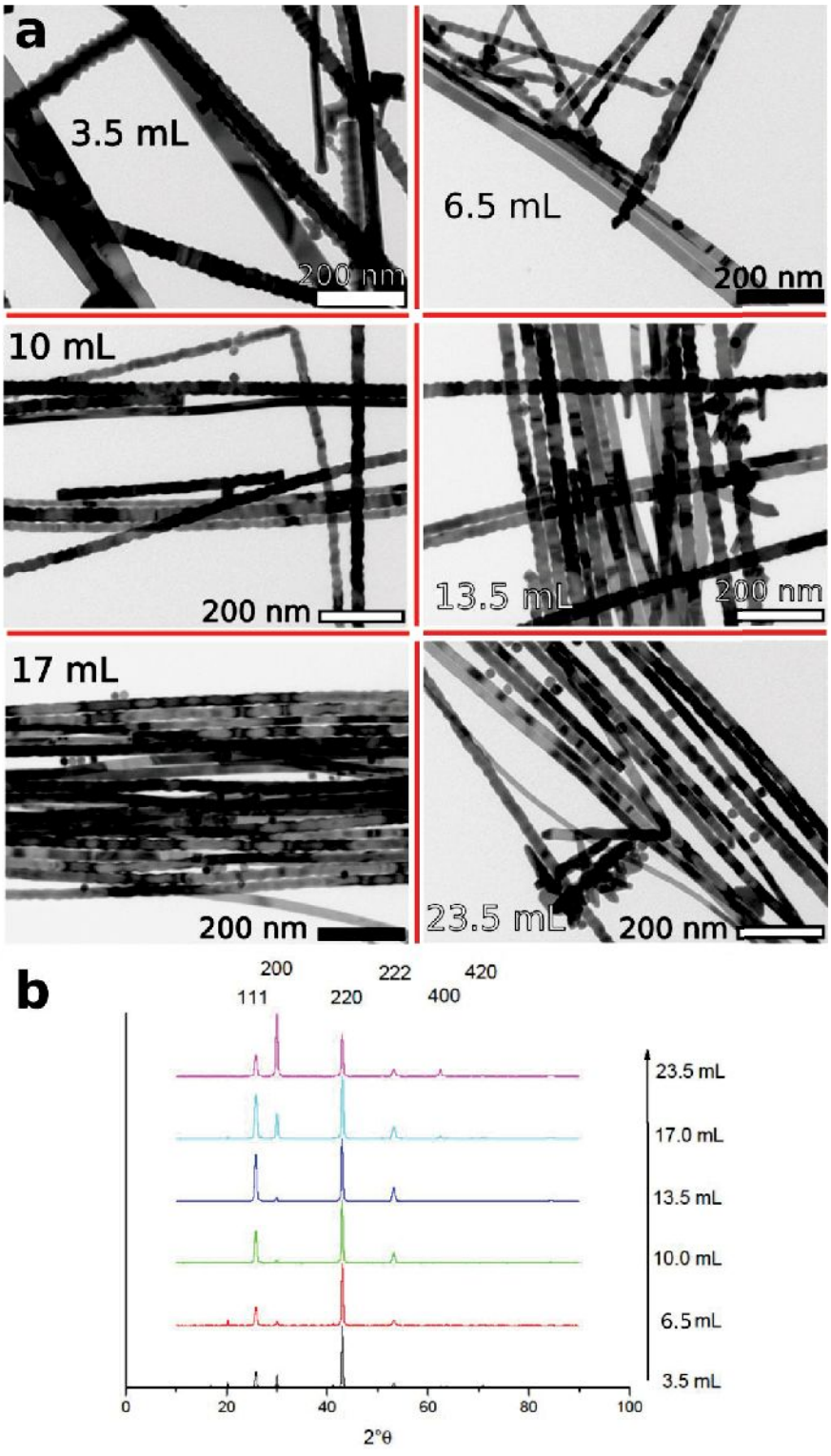

Figure S7. The effect of the solvent concentration on the products. (a) TEM images of the wires produced with different amounts of solvent. (b) XRD of the products. It seems that the wires are

thicker/wider with less solvent used in synthesis. The color change appears after 10 s with 3.5 mL DPE and after 40 s when 23.5 mL DPE was used. The hypothesis of a fast nucleation to zigzag wires with a high monomer concentration followed by a later nucleation to flat ones with a lower monomer concentration can be confirmed with these experiments. With increasing the amount of DPE and further dilution, more flat shaped wires are obtained (reflexes 111 and 200 vs. 220). However, decreasing the amount of the solvent does not lead to only zigzag wires but to thicker/wider wires.

12- XPS peaks

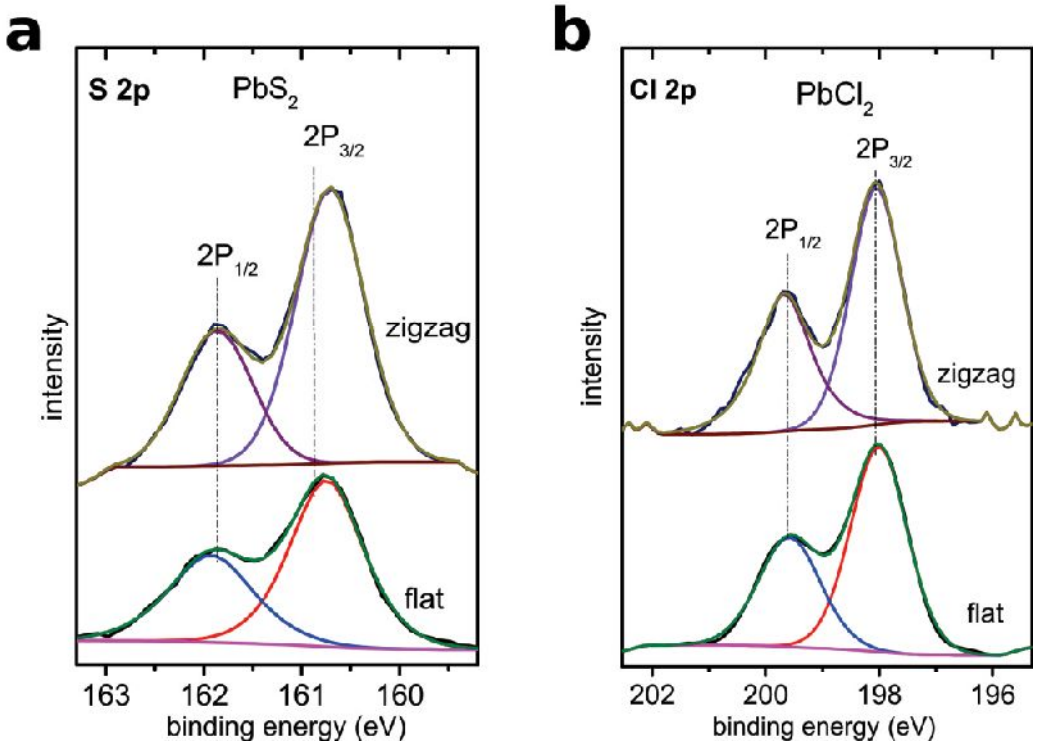

Figure S8. Deconvoluted XPS peaks of the samples for the S 2p and Cl 2p regions. (a) The S 2p core level spectra verifies the formation of PbS with the 2p 3/2 and 2p 1/2 peaks at 160.7eV and 161.9 eV, respectively. (b) The Cl 2p peaks of the samples, with the peaks at 198.0 eV and 199.6 eV attributed to $PbCl_2$. The XPS spectra show that Cl is bound to Pb and does not exist as free Cl^- ions.

A3 Chemicals

Table1: GHS information on hazardous substances used for the sample preparation in this thesis.

Chemical	Symbol	Hazard statement	Precautionary statement
Acetone	GHS02 GHS07	H225 H319 H336	P210 P261 P303+P361+P353 P305+P351+P338 P405 P501
Chlorobenzene	GHS02 GHS07 GHS09	H226 H315 H332 H411	P210 P261 P370 + P378
Lead sulphide	GHS07 GHS08 GHS09	H302 + H332 H360Df H373 H410	P201 P260 P280 P301 + P312 + P330 P308 + P313
Methyl isobutyl ketone	GHS02 GHS07	H225 H319 H332 H335	P210 P261 P305 + P351 + P338
Poly(methyl methacrylate)			
Propanol	GHS02 GHS07	H225 H319 H336	P210 P261 P305 + P351 + P338
Toluene	GHS02 GHS07 GHS08	H225 H304 H315 H336 H361d H373	P210 P261 P281 P301 + P310 P331

Acknowledgements

First and foremost, I offer my sincerest gratitude to my supervisor, Prof. Christian Klinke, who has supported me throughout this project with his patience and knowledge whilst allowing me the room to work in my own way. Working with him was the most amazing part of this project. He has taught me a lot, not only about the science, but also about the politics, the society, and about the life. One simply could not wish for a better and friendlier supervisor.

I would also like to thank my second supervisor, Prof. Horst Weller, for his encouragement and insightful comments.

Many thanks are addressed to all members of the Institute of Physical Chemistry for their technical and organizational supports, specially Mr. Andreas Kornowski, Mr. Robert Schön, and Ms. Daniela Weinert for their great microscopy works. I also thank Ms. Beate Kreutzer, Ms. Sigrid Zeckert, and Ms. Martina Krasa for their kind administrational helps.

I would offer my special thanks to our collaborators, Prof. Carmen Herrmann and Martin Zöllner for their theoretical contributions as well as Dr. Heshmat Noei and Prof. Andreas Stierle for the XPS measurements.

The PIER Helmholtz Graduate School and its super-friendly coordinators are gratefully acknowledged for their appreciable financial and organizational supports during my doctoral project.

Special appreciation goes to my colleagues of the work group, Dr. Rostyslav Lesyuk, Dr. Hauke Lehmann, Dr. Sedat Dogan, Dr. Thomas Bielewicz, Dr. Mirjam Volkmann, Dr. Andrés Black, Dr. Irina Nefedova, Frauke, Leo, Eugen, Fu, Sascha, Michael, Svenja, and Angelique, for cooperating with me in terms of synthesis, characterization, and scientific discussions. I will never forget you and the times we had together. I would also like to thank my students, Alex, Gabrielle, Philip, and Jan for their helps during the project.

I thank all of my friends for helping me to get through the difficult times, and for all the emotional support, camaraderie, entertainment, and caring they provided.

Last but not the least, my deep and sincere gratitude to my family for their continuous and unparalleled love, help and support. I love you and sorry if I could not be with you as much as I had to be.

Declaration

I hereby declare on oath, that I have written the present dissertation by my own and have not used other than the acknowledged resources and aids. The submitted written version corresponds to the version on the electronic storage medium. I hereby declare that I have not previously applied or pursued for a doctorate (Ph.D. studies).

Mohammad Mehdi Ramin Moayed

Date: Signature: